UNIVERSIDAD TECNICA
FEDERICO SANTA MARIA

PONTIFICIA
UNIVERSIDAD
CATÓLICA DE
VALPARAÍSO

UNIVERSIDAD TÉCNICA FEDERICO SANTA MARÍA
PONTIFICIA UNIVERSIDAD CATÓLICA DE
VALPARAÍSO

DOCTORAL THESIS

Toroidal Moments in Micromagnetism and their Connection with Magnonics

---

Author:
Felipe BREVIS GARRIDO

Supervisor:
Dr. Pedro LANDEROS

Co-supervisor:
Dr. Rodolfo GALLARDO

A thesis submitted in fulfillment of the requirements
for the degree of Doctor in Physics

January 21, 2026

CONSTANCIA DE VALIDACIÓN Y CONFIDENCIALIDAD DE MONOGRAFÍA A REPOSITORIO ACADÉMICO

1.- IDENTIFICACIÓN DEL TRABAJO ACADÉMICO

Tipo de monografía (marcar una opción): ☐ Memoria o trabajo de título ☒ Tesis de Postgrado

Título del trabajo: Toroidal Moments in Micromagnetism and their Connection with Magnonics

Nombre del candidato(a): Felipe Eduardo Brevis Garrido

Carrera / Grado: Doctorado en Ciencias Físicas

Campus: Casa Central **Departamento:** Departamento de Física

2.- VALIDACIÓN DEL PROFESOR GUÍA/DIRECTOR DE TESIS

Yo, Pedro Miguel Landeros Silva, en mi calidad de profesor(a) guía/director(a) del trabajo académico mencionado anteriormente **DEJO CONSTANCIA** que:

- He revisado esta versión del documento y corresponde a la versión final aprobada del trabajo.
- El trabajo cumple con los requisitos académicos y de formato establecidos por la institución.

3.- EVALUACIÓN DE CONFIDENCIALIDAD POR PROPIEDAD INDUSTRIAL (marcar una opción)

☒ El trabajo **NO contiene** información que amerite confidencialidad y puede ser publicado de inmediato en repositorio con acceso abierto.

☐ El trabajo **CONTIENE** información con potenciales implicancias de propiedad industrial o intelectual y requiere un periodo de confidencialidad (**embargo**) por **(marcar una opción)**:

☐ 6 meses ☐ 12 meses ☐ 2 años ☐ 3 años ☐ 5 años ☐ 10 años

Fundamentación de la necesidad de confidencialidad (obligatorio si se solicita embargo):

_____

_____

_____

4.- FIRMAS

Profesor(a) guía o director(a) de memoria o tesis:

Fecha: 15-01-2026 **Firma:** _____

Estudiante o Candidato(a):

Fecha: 15-01-2026 **Firma:** _____

Este formulario debe ser insertado como página 2 de la memoria o tesis, completado y firmado por estudiante y profesor(a) antes de la entrega en portal PRISMA de Biblioteca USM.

"Dejo a Sísifo al pie de la montaña. Se vuelve a encontrar siempre su carga. Pero Sísifo enseña la fidelidad superior que niega a los dioses y levanta las rocas [...] El esfuerzo mismo para llegar a las cimas basta para llenar un corazón de hombre. Hay que imaginarse a Sísifo dichoso."

El mito de Sísifo
Albert Camus

UNIVERSIDAD TÉCNICA FEDERICO SANTA MARÍA
PONTIFICIA UNIVERSIDAD CATÓLICA DE VALPARAÍSO

Abstract

Toroidal Moments in Micromagnetism and their Connection with Magnonics

by Felipe BREVIS GARRIDO

Nonreciprocal propagation of spin waves in magnetic media is one of the central ingredients for information transport and signal processing in magnonics. In this context, the magnetic toroidal moment ($\boldsymbol{\tau}$), originally introduced in the context of multiferroic systems and the magnetoelectric effect, can indicate configurations that break both spatial inversion and time-reversal symmetries, and is therefore a quantity to describe and design nonreciprocal responses. However, its formulation within micromagnetism, such as the different definitions, the choice of origin, and its connection to magnon spectra remain only partially understood. This thesis develops a micromagnetic framework for toroidal moments in confined magnetic structures and establishes their impact on spin-wave nonreciprocity. Different definitions of the toroidal moment are revisited and related in terms of continuous magnetization distributions, where a volume and surface contributions to the toroidal moment are found. The role of the choice of origin, and a possible connection between toroidal moments and the antisymmetric part of the spin-wave tensor are studied. The toroidal moment is evaluated for a broad class of magnetic systems and geometries, including ferromagnets with electric currents, conical–helical states in thin films and tubes, skyrmions, merons and bimerons in confined structures, and ferromagnetic systems with graded magnetization, revealing the conditions for the presence of a toroidal moment according to the magnetic ground state, some parameters and geometry. Moreover, the thesis corroborates that a finite projection $\boldsymbol{\tau} \cdot \mathbf{k} \neq 0$ between the toroidal moment and the spin-wave wave vector provides a useful condition for nonreciprocal magnon propagation. This criterion is shown to agree with well-known mechanisms of nonreciprocity, such as current-driven Doppler shifts, graded magnetic profiles, Dzyaloshinskii–Moriya interaction, and curvature-induced symmetry breaking in curved geometries. Interestingly, from an optical perspective, the propagation of electromagnetic waves in a medium with a finite toroidal moment yields a dispersion relation containing the scalar product $\boldsymbol{\tau} \cdot \mathbf{k}$. Moreover, the dynamics of the toroidization are captured by a pair of equations of motion analogous to the Landau–Lifshitz–Gilbert equation, which couple the toroidization to the magnetization and to the monopolar magnetoelectric contribution. Altogether, these results consolidate the toroidal moment as a key parameter for designing nonreciprocal magnonic systems in novel magnetic media. Finally, the evolution from flat stripes to closed nanotubes is analyzed, revealing curvature-induced parity breaking, mode hybridization, and dispersion asymmetries in agreement with the associated toroidal moments.

Acknowledgements

Si hay una palabra que puede resumir este proceso de doctorado, es gratitud. Gratitud hacia las personas que han estado cerca, que me han apoyado, que me han considerado para trabajar y que me han tenido paciencia también. Soy un convencido de que son las personas que nos rodean las que hacen de un proceso algo placentero o no.

Agradezco a mi tutor, Prof. Pedro Landeros, por su constante apoyo y entendimiento, y por transmitirme su pasión por la ciencia, por indagar hasta la última línea en los artículos y por buscar siempre algo original, novedoso y excelente. También me siento afortunado de trabajar con mi cotutor, Dr. Rodolfo Gallardo, de quien he aprendido mucho y quien me consideró para aportar un granito de arena. En la misma línea, estos años no habrían sido los mismos sin el Dr. Jorge Flores, compañero de trabajo y de almuerzos. Muchas gracias por todo y por los tiempos de esparcimiento. Agradezco al Dr. David Cortés, con quien he aprendido muchísimo de simulaciones micromagnéticas, y aprovecho de dejar constancia de mi admiración por su conexión con el arte. Bunkers: muchas gracias.

Quiero agradecer a mi mamá, que ha sido siempre mi modelo y mi pilar, quien puso en mí de pequeño la semilla de la ciencia y la de luchar por los sueños. El orgullo es mutuo. Agradezco a mi familia, tías, tíos, primos y primas, siempre pendientes y preocupados por mí; en especial a mi prima Bárbara, quien es como una hermana: gracias por tu apoyo. El doctorado también me permitió conocer personas hermosas, entre ellas Elías Santacruz, Aarón Cofré, Pablo Silva y Francisca Rojas. Formamos un grupo muy familiar que ha sido de gran amistad y apoyo; eternamente agradecido y afortunado de tenerlos en mi vida.

Tuve la suerte de realizar una pasantía en el HZDR, en Dresden, Alemania, y de llegar a un grupo humano fantástico (con el que almorzábamos juntos todos los días). En particular, agradezco al Dr. Attila Kákay, de quien pude aprender mucho, tanto en lo humano como en lo científico. Allí pude trabajar con el Dr. Lukas Körber, de quien también aprendí muchísimo y con quien pudimos compartir algunas *helles*. Agradecimiento especial a Amelie Fehrmann: Danke für die Spaziergänge. Agradezco, además, la hospitalidad del Dr. Helmut Schultheiss y de la Dra. Katrin Schultheiss.

Quisiera mencionar, con mucho cariño, a quienes me motivaron a iniciar este proceso de doctorado: Prof. Pablo Díaz, Prof. Eduardo Cisternas, Prof. Eugenio Vogel y Prof. David Laroze. Menciono también a algunos miembros de la comunidad USM que han hecho de este paso por el Depto. de Física uno muy agradable: Prof. Patricio Vargas, Dr. Francisco Peña, Prof. Vladimir Juričić, Prof. Pedro Orellana, Dr. Christian Orellana, Marcela Aguirre y Angélica Neira, y a toda la gente bacán que conocí en USM/PUCV: Pata, Malu, Rocío, Gabriel (HZDR), Benja M., Matías C., José J., Pedro C., Alexis L., João, Iván, Leo V., Hishan, Yeslaine, Michel, Jeremy. Por último, me siento agradecido también por todos mis amigos y amigas de Temuco: Nacho, Gerardo, Simón, Chelo, Héctor, Checho, Pancho, Víctor, Caro, Dani, Schubi y Lito.

Finalmente, por supuesto, a las fuentes de financiamiento: Beca de Doctorado Nacional ANID, proyectos Fondecyt y el apoyo de la USM.

Gracias

Contents

List of Figures

List of Tables

List of Symbols

$\mathbf{M}$	Magnetization	$\mathrm{A\,m^{-1}}$
$\mathbf{m}$	Unitary magnetization	–
M_s	Saturation magnetization	$\mathrm{A\,m^{-1}}$
$\mathbf{H}$	Magnetic field	$\mathrm{A\,m^{-1}}$
$\mathbf{H}_\mathrm{eff}$	Effective magnetic field	$\mathrm{A\,m^{-1}}$
A_ex	Exchange stiffness	$\mathrm{J\,m^{-1}}$
λ_ex	Exchange length	m
$\boldsymbol{\mu}$	(Local) Magnetic moment	$\mathrm{A\,m^2}$
$\boldsymbol{m}_{tot}$	Magnetic moment	$\mathrm{A\,m^2}$
a	Magnetoelectric monopolar moment	$\mathrm{A\,m^3}$
Q_{ij}	Magnetoelectric quadrupole moment	$\mathrm{A\,m^3}$
D	Dzyaloshinskii-Moriya strength	$\mathrm{J\,m^{-2}}$
$\mathbf{D}$	Dzyaloshinskii-Moriya vector	$\mathrm{J\,m^{-2}}$
$\mathbf{k}$	Spin-wave wave vector	$\mathrm{m^{-1}}$
$\mathbf{q}$	Pitch vector of the helical/conical state	$\mathrm{m^{-1}}$
ω	Angular frequency of the spin-wave mode	$\mathrm{rad\,s^{-1}}$
f	Spin-wave frequency	Hz
α	Gilbert damping parameter	–
γ	Gyromagnetic ratio	$\mathrm{rad\,s^{-1}\,T^{-1}}$
$\boldsymbol{\tau}$	Toroidal moment	$\mathrm{Am^3}$
$\boldsymbol{\tau}^\mathrm{v}$	Volume toroidal moment	$\mathrm{Am^3}$
$\boldsymbol{\tau}^\mathrm{s}$	Surface toroidal moment	$\mathrm{Am^3}$
$\hat{\mathbf{N}}$	Effective magnetic tensor	–
$\mathcal{N}(\mathbf{k})$	Effective spin-wave tensor	–

Dedicado a mi mamá

Chapter 1

Introduction

1.1 Motivation

The relentless push for faster, smaller, and more energy efficient technologies has brought modern electronics close to its physical boundaries. For decades, Moore's law, predicting the exponential growth of transistor density, has driven the miniaturization of components and the consequent enhancement of computing performance. However, as transistor dimensions approach the nanometer scale, several critical challenges arise: excessive Joule heating, quantum tunneling effects, and escalating power consumption collectively limit further downscaling. These constraints not only threaten device functionality and reliability but also amplify environmental concerns due to the enormous energy cost of information processing [1].

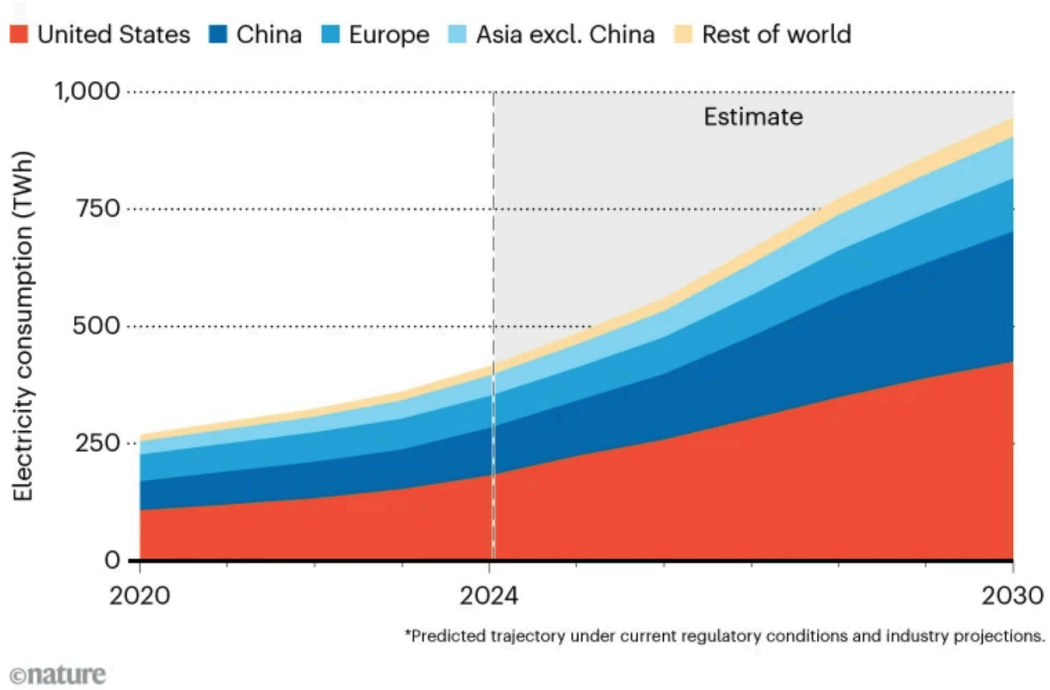

FIGURE 1.1: Global data center energy consumption with trends and projections to 2030. Figure extracted from the news article "Data centers will use twice as much energy by 2030 — driven by AI" [2].

In the so-called "Beyond Moore's Law" era, these limitations underscore the urgent need for alternative paradigms. Conventional technology and computing faces multiple shortcomings. Among these challenges is the exorbitant energy demand of data centers. As illustrated in Fig. 1.1, global data center energy consumption is projected to almost quadruple by 2030, primarily driven by the increasing use

of artificial intelligence (AI) [2]. Another set of limitations arises from the inherent trade off between memory speed and storage capacity in electronic components. Moreover, the well-known von Neumann bottleneck imposes a fundamental constraint on computing performance, since the processor (CPU) and the main memory share a common data pathway (the system bus), the rate of information exchange is severely restricted. This architectural limitation not only hinders computational efficiency but also obstructs further optimization in terms of size, weight, and power consumption. Such trends make evident that sustaining progress requires the adoption of unconventional approaches, leveraging nanotechnologies to enhance energy efficiency, speed, and scalability while enabling radically new architectures for information processing.

To overcome these challenges, alternative paradigms to electronics have been proposed. Among them are spintronics, which exploits the electron's spin degree of freedom [3], and photonics, which relies on the manipulation of light. A relatively recent and promising counterpart is *magnonics*, where information is carried by collective excitations of the magnetization, known as *spin waves* or *magnons* [4, 5]. Magnonic devices offer potential advantages such as operation in the gigahertz/terahertz frequency range [6], low heat generation [7], compatibility with established nanofabrication techniques [8] and the possibility to naturally provide a viable alternative for "Beyond 6G" applications in telecommunications [9]. Among several properties, spin waves offer the possibility of achieving *nonreciprocal propagation* [10, 11]. In such cases, spin waves with opposite wave vectors, $+k$ and $-k$, possess different frequencies, enabling functionalities analogous to isolators and diodes in conventional electronics [8]. Nonreciprocal effects are of practical importance for unidirectional information transport, suppression of backscattering, and the realization of magnonic circuits [12]. They also reflect fundamental chiral and symmetry-breaking mechanisms in the magnetic medium, thus offering a bridge between applied and basic research, as well as between classical and quantum phenomena [13].

Nonreciprocal propagation can be achieved through different physical mechanisms. On the one hand, geometrical factors such as curvature [14–21], magnetization gradients [22], anisotropy gradients [23] or multilayer arrangements [24–28] can induce asymmetries in the spin-wave spectrum. On the other hand, intrinsic magnetic interactions such as dipolar coupling [15, 17, 18], symmetric exchange [16, 21], or the Dzyaloshinskii–Moriya interaction (DMI) also break inversion symmetries and give rise to dispersion asymmetries [29, 30]. Some of these well-established mechanisms can be indicated by quantities which naturally encode symmetry breaking, and therefore provide, in principle, new routes for designing nonreciprocal devices [31, 32]. One relevant quantity for this purpose is the *toroidal moment*, which is arises as a multipole moment associated with circulating magnetization and current distributions. This quantity has been linked not only to nonreciprocal transport phenomena but also to magnetoelectric effects in multiferroic systems, highlighting its fundamental and technological relevance [33].

1.2 State of the Art

1.2.1 Magnonics Today

Magnonics has emerged over the last decades as a central branch of modern spintronics, in order to take advantage of the collective spin excitations called spin waves or magnons, for wave based information transport and processing [34]. The motivation stems from the limitations of nanoscale charge based electronics, where Joule

heating and size limits block further progress, and from the quest for alternative platforms that are energy efficient, fast and compatible with actual integrated circuits [8]. In this context, magnonics offers a distinct paradigm: information is carried not by moving charges but by the coherent precession of localized magnetic moments, enabling signals flowing with almost no dissipation in low damping materials such as yttrium iron garnet (YIG) [35].

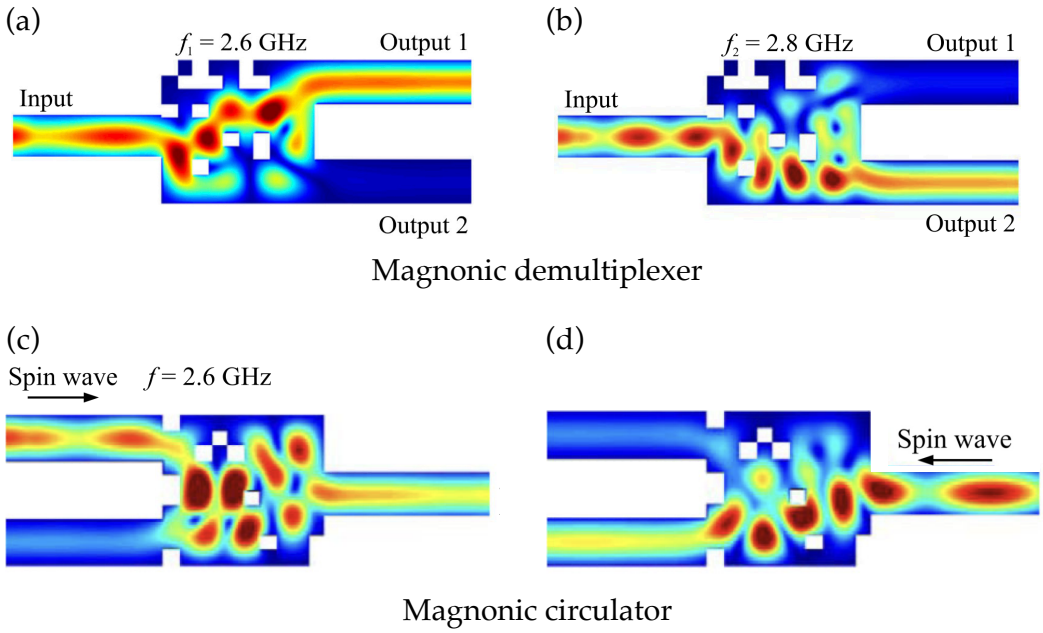

FIGURE 1.2: Simulated magnonic devices. (a-b) shows demultiplexers, whose input is a spin wave composed of two frequencies, f_1 = 2.6 GHz and f_2 = 2.8 GHz, and which, after passing through the designed zone, follow different paths depending on their frequency. (c-d) shows two circulators. In this case, a spin wave is excited either from the left (c) or from the right (d) at the same frequency, and the resulting propagation trajectories are nonreciprocal. Adapted from Ref. [36]

In general, spin waves span a broad spectral range, covering frequencies from sub-gigahertz magnetostatic modes up to hundreds of gigahertz [35–37], and even terahertz regimes for exchange dominated excitations in antiferromagnetic materials [38]. This extensive spectrum enables a wide variety of functionalities and operational regimes for magnonic systems. One of the main focuses of current research in the field is the development of reconfigurable and multifunctional magnonic components that can dynamically control the propagation and interference of spin waves. Typical building blocks in this context include magnonic waveguides, interferometers, directional couplers, multiplexers, circulators, and frequency selective filters [11, 36]. Among these, magnonic waveguides play a central role, serving as fundamental conduits for spin-wave transport and signal processing. By introducing tailored geometries, magnetic inhomogeneities, spatial modulation of magnetic parameters, or by exploiting specific magnetic interactions, it becomes possible to engineer complex functionalities such as wave channeling, band gap formation, frequency demultiplexing, logic operations, and nonreciprocal signal routing. The operation of such devices relies on the precise engineering of internal magnetic textures, Dzyaloshinskii–Moriya interactions, or external magnetic fields, which modify the local dispersion relation and channel spin waves of different frequencies or

wavevectors along distinct paths. An example of this concept is shown in Fig. 1.2, where an engineered coupling region enables frequency dependent spin-wave demultiplexing [39, 40], illustrating the potential of magnonic architectures for wave-based information processing and integrated magnonic circuitry [36].

Another type of reconfigurable system are the so-called magnonic crystals (MC), which are arrays of periodically modulated structures hosting tunable band gaps, engineered dispersion relations, and programmable transmission characteristics [45, 46]. These artificial media are the magnetic analogue of photonic crystals and allow precise control over spin-wave propagation by tailoring the periodicity and symmetry of the underlying structure [35]. Depending on the implementation, MCs can be realized in one [41, 43], two [42, 43], or even three dimensions [47], with periodic modulations introduced either geometrically, for example by patterning grooves, or magnetically, by applying spatially varying bias fields or periodically depositing other materials that induce special interactions such as interfacial DMI [44, 48]. Experimentally, magnonic crystals are fabricated using advanced nanolithography, focused ion beam milling, or thin film deposition techniques that enable nanoscale patterning with high fidelity. Their properties are typically probed through techniques such as Brillouin light scattering (BLS) spectroscopy [49, 50], time-resolved magneto-optical Kerr effect (TR-MOKE) [51].

Figure 1.3 shows examples of magnonic crystals found in the literature. Figure 1.3 (a) illustrates a one-dimensional magnonic crystal (MC) consisting of an array of bilayered nanowires, where the top (bottom) layer is composed of Fe (permalloy) [41]. Fig. 1.3 (b) depicts a two-dimensional magnonic crystal formed by a bicomponent antidot–dot lattice, in which the antidot lattice is patterned in permalloy ($Ni_{80}Fe_{20}$, Py), while the dot lattice is composed of Co [42]. Similar systems were investigated by Yu et al. [43], who fabricated ferromagnetic structures featuring various types of periodic modulations, or gratings, and excited them using microwave antennas. Notably, in a CoFeB-Py bicomponent lattice where Py nanodisks are embedded in a CoFeB thin film, spin waves excited by a coplanar waveguide exhibit omnidirectional propagation as shown in Fig. 1.3(c). Panels (d) and (e) show two possible realizations of 1D chiral magnonic crystals, where the Dzyaloshinskii–Moriya interaction gives rise to chiral effects due to the proximity of a heavy metal such as Pt. In panel (d), a ferromagnetic film is periodically covered by heavy metal stripes (or wires), while in panel (e) a bicomponent magnonic crystal composed of two different ferromagnetic materials is uniformly capped with a heavy metal layer [44]. Such magnonic systems give rise to a variety of nontrivial dynamical effects, including an enhancement of the spin-wave dispersion relations, the emergence of magnonic band gaps, and the formation of flat bands [52–54]. The latter have attracted particular attention in recent years, as they are intimately connected to the phenomenon of spin wave localization, where magnons become confined within specific spatial regions of the crystal due to interference and symmetry effects [55, 56].

A promising approach for designing reconfigurable magnetic devices with tunable and emergent properties relies on the controlled use of magnetic textures [59]. Spin waves propagating in magnetic textures constitute a developing branch of magnonics, where noncollinear spin configurations, such as those shown in Fig. 1.4, act as reconfigurable media for magnon transport and manipulation. Magnons propagating along helical textures are also referred to as *helimagnons*, where the chiral ground state serves as a one-dimensional magnetic crystal defined by the pitch of the magnetic texture [60, 61]. Unlike homogeneous ferromagnets, magnetic textures such as domain walls [62, 63], vortex state in nanotubes [14–21], skyrmions [61, 64], or

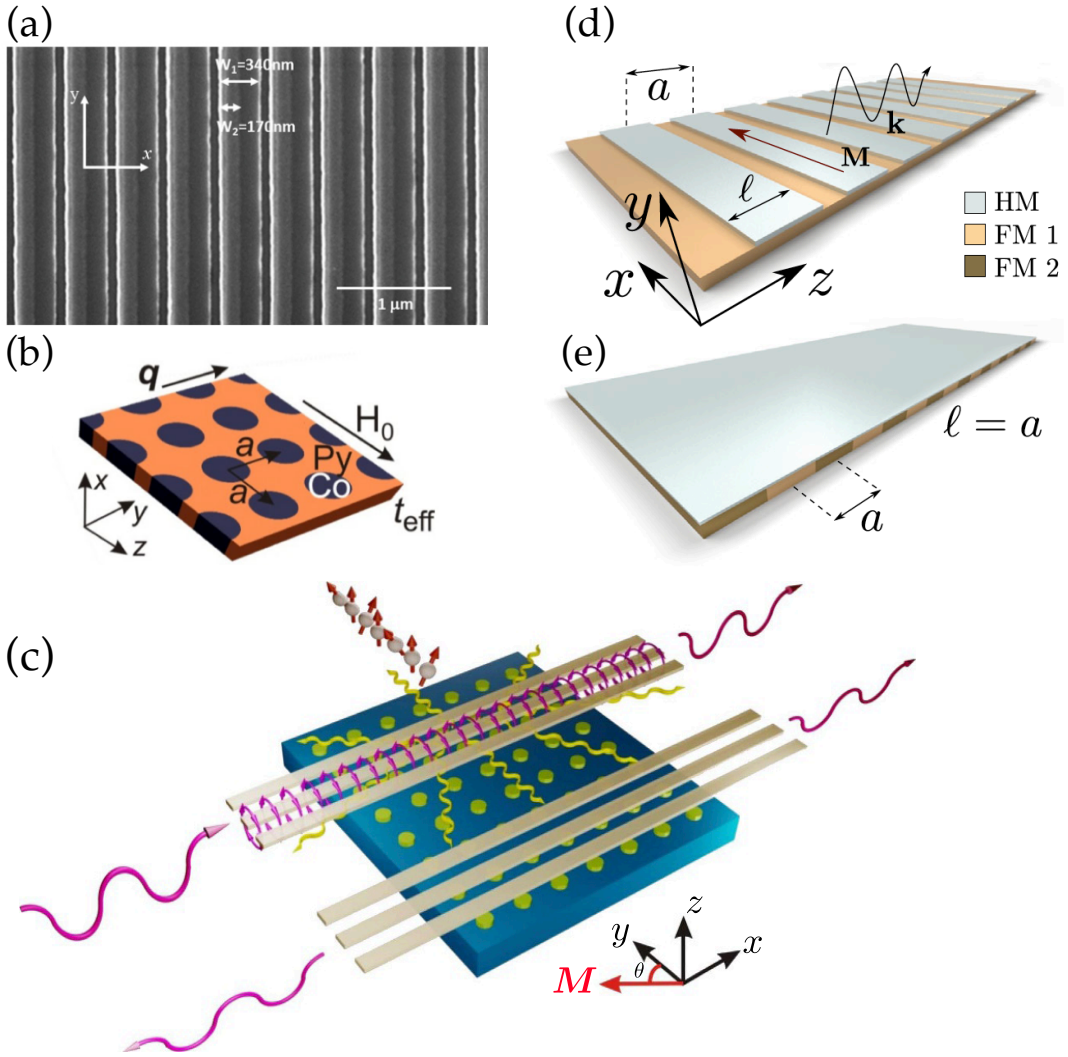

FIGURE 1.3: Examples of magnonic crystals. (a) Magnonic crystals consisting of bilayer Py/Fe nanowires periodically distributed, extracted from Ref. [41]. (b) Binary component dot-antidot lattice with Co nanodisks embedded in a Py film, extracted from Ref. [42]. (c) 2D magnonic grating coupler where omnidirectional spin waves (yellow arrows) are excited by a coplanar waveguide, extracted from Ref. [43]. Chiral magnonic crystals are shown in (d) and (e). (d) Ferromagnetic ultrathin film covered by a periodic array of heavy metals wires such as Pt. (e) Bicomponent magnonic crystal made of two ferromagnets coupled to a heavy metal layer. Adapted from Ref. [44].

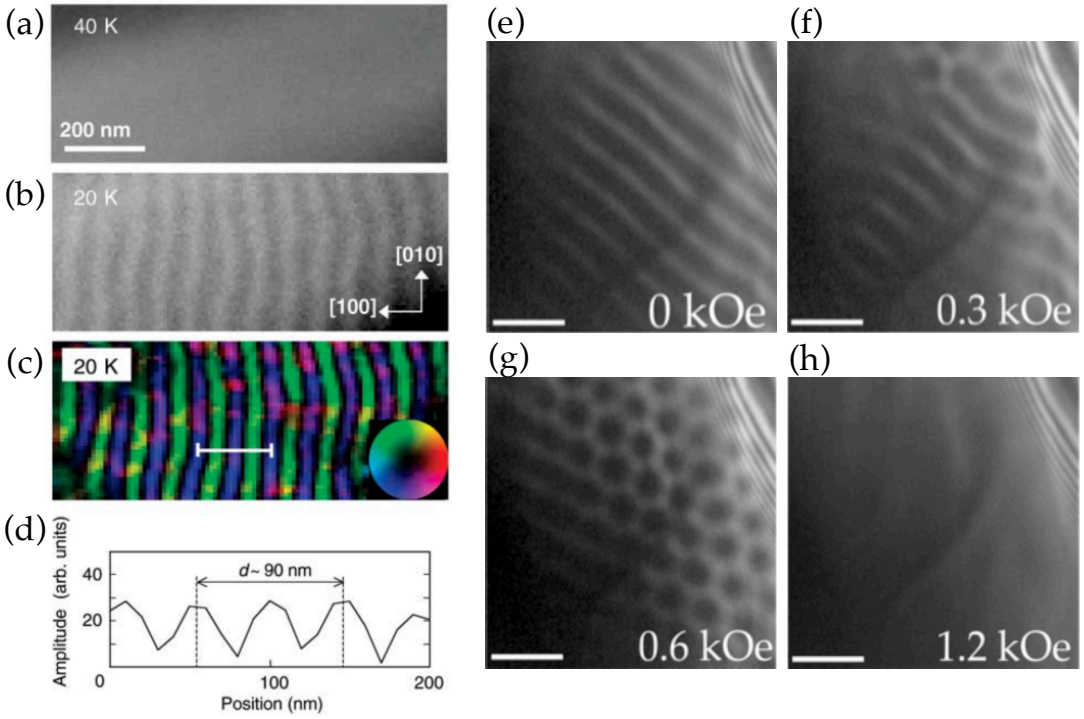

FIGURE 1.4: Real space observation of helical and skyrmionic spin textures in $Fe_{0.5}Co_{0.5}Si$ (a–d) and in an epitaxial FeGe film (e–h). (a,b) Lorentz transmission electron microscopy (LTEM) images reveal the helical spin configuration at 40 K and 20 K, respectively. (c) Magnetization distribution at 20 K, and (d) corresponding amplitude profile along the line indicated in (c). (e–h) Evolution of the spin texture, via LTEM, in FeGe from a helical ground state at zero magnetic field to the coexistence region with a skyrmion lattice and finally to the field polarized state upon increasing the external field. Panels (a-d) extracted from Ref. [57] and (e-h) from Ref. [58].

conical-helices in planar films [57, 65, 66] provide intrinsic, spatially varying effective fields that shape the local dispersion and induce phenomena such as spin-wave channeling, reflection, or mode hybridization [67]. Noncollinear spin structures can be observed as can be seen in Fig. 1.4, showing the transition from helical to skyrmionic spin arrangements in $Fe_{0.5}Co_{0.5}Si$ and FeGe films [57, 58], where bulk DMI in chiral magnets promotes the formation of these textures at certain temperatures and applied external fields. Since the underlying spin textures can be manipulated by external stimuli including magnetic fields, electric currents, or even strain, texture based magnonics offers promising routes toward dynamic reconfigurability.

One of the key properties enabling reconfigurability in magnonic systems is the nonreciprocal propagation of spin waves. In this context, nonreciprocity refers to the asymmetric transmission characteristics of spin waves propagating with opposite wave vectors $\pm\mathbf{k}$, i.e., the dispersion relation or amplitude differs for waves traveling in opposite directions [71]. This effect arises when time reversal symmetry and spatial inversion or mirror symmetry are broken, so that counterpropagating waves are no longer equivalent. It can originate from different sources, including dipolar interactions, Dzyaloshinskii–Moriya interactions, structural and geometrical asymmetries, or the application of external electric currents, among others [8]. In such conditions, spin-wave propagation becomes direction dependent, enabling

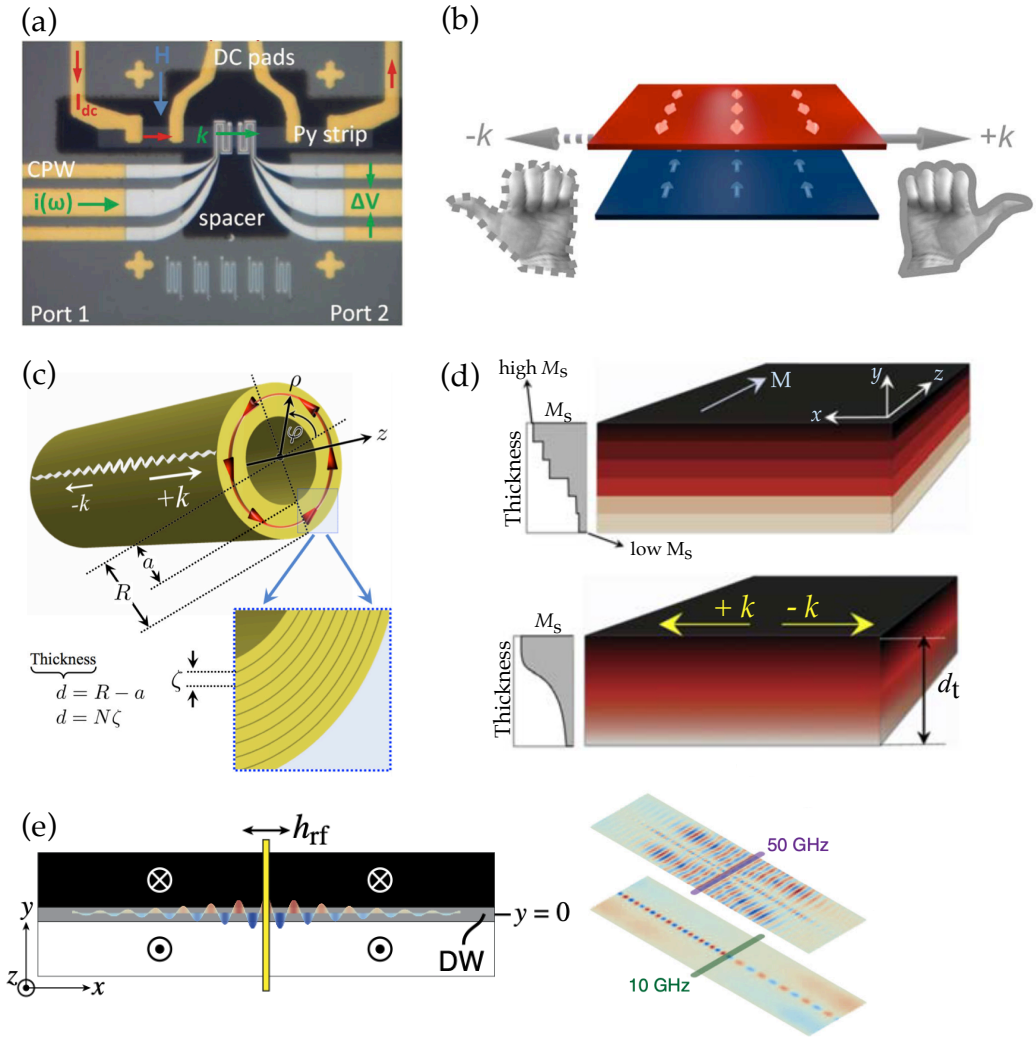

FIGURE 1.5: Illustrations of nonreciprocal magnonic systems. (a) Optical micrograph of a current induced spin-wave Doppler shift device, where a DC current flows through a permalloy strip along the spin-wave propagation direction, extracted from Ref. [68]. (b) Antiparallel magnetic bilayer exhibiting opposite chiralities for magnon phase propagation along $+k$ (right-handed) and $-k$ (left-handed) directions, extracted from Ref. [69]. (c) Thick ferromagnetic nanotube in a vortex state with spin waves propagating along the tube axis, extracted from Ref. [17]. (d) Ferromagnetic systems with a thickness-dependent saturation magnetization M_s. In one case, M_s varies in discrete steps (multilayer), while in the other it changes continuously. In both cases, the equilibrium magnetization is uniform along z and spin waves propagate along x, extracted from Ref. [22]. (e) Domain-wall waveguide with propagation along the x-axis; simulated magnetization profiles for a Néel wall are shown, extracted from Ref. [70].

anisotropic or even unidirectional transport of information and the realization of functionalities analogous to those of microwave isolators, circulators, and diodes [27, 36, 72]. These properties have been extensively exploited in prototype magnonic devices such as transistors and logic gates [73, 74], where amplitude or phase modulation is employed to control signal routing and interference based logic operations [11, 75]. Such advances highlight the potential of magnonics to evolve into integrated, wave-based computing platforms that could complement or even surpass

conventional CMOS architectures [75]. Fig. 1.5 illustrates four different magnetic systems which exhibit nonreciprocal magnonic behavior.

Among the mechanisms responsible for spin-wave nonreciprocity, two stand out as particularly relevant for current research. The first originates from dipolar induced asymmetry in the Damon–Eshbach geometry, where the magnetization **M** lies in the film plane and is perpendicular to the spin-wave wavevector **k** [76]. In this configuration, dynamic dipolar fields confine the spin-wave mode near opposite film surfaces for opposite propagation directions, giving rise to nonreciprocity [77]. Many studies have shown dipolar induced nonreciprocity in a variety of different systems. To name a few, in arrays of magnetic nanopillars with different magnetic states and geometrical asymmetries [78], ferromagnetic multilayers and bilayers [24–28] aligned antiparallel, known as synthetic antiferromagnets (SAF)[as can be seen in Fig. 1.5(b)], as well as in ferromagnetic nanotubes in vortex/curling states [14–21] [see Fig. 1.5(c)] or with specific geometrical shapes [79–81]. Magnetostatic interactions also induce spin-wave nonreciprocity in systems with gradient in the saturation magnetization M_s as it breaks the space-inversion symmetry [22, 23], as shown in Fig. 1.5(d) in thick films where M_s changes along the thickness and spin waves propagate in Damon-Eshbach configuration.

The second mechanism, which is currently the subject of intensive research, originates from the Dzyaloshinskii–Moriya interaction (DMI). This interaction can be categorized by its origin. The interfacial DMI (i–DMI) arises at the interfaces between a ferromagnet and a heavy–metal with strong spin–orbit coupling, such as Platinum (Pt), Tungsten (W) or Iridium (Ir) [82–84]. On the other hand, the bulk DMI (b–DMI) is intrinsic to chiral magnets like MnSi or FeGe which crystallize in the B20 cubic crystal structure [85, 86]. The DMI introduces a chiral exchange term that lifts the degeneracy between counterpropagating spin waves, producing a frequency splitting Δf and enforcing a fixed sense of precession. Consequently, spin waves acquire a chiral character under this interaction [87–89]. Fig. 1.5(e) shows an example of nonreciprocal spin waves propagating along a Néel domain wall with i–DMI. Moreover, spatial modulation of the i–DMI strength enables the design of chiral magnonic crystals with engineered indirect gaps and flat bands [52–56].

1.2.2 The toroidal realm

Toroidal order is ubiquitous in nature. Structures from completely different scales, from the tangible to the abstract, can exhibit toroidal topology. Everyday examples include donuts, smoke rings, vortex rings in fluids, and lifebuoys, all representing simple macroscopic realizations of the torus. At the opposite extreme, astrophysical and cosmological systems display toroidal features as well, with magnetic flux loops and galactic magnetic fields often adopting toroidal components [91]. This geometry is distinguished by its continuous circular symmetry and central void. Even in biology, toroidal-like forms emerge: the biconcave shape of red blood cells optimizes surface area and mechanical flexibility, while supercoiled DNA loops contribute to the spatial organization of chromatin. Figure 1.6 shows some of these toroidal structures existing in nature.

In the context of plasma physics and magnetic confinement, toroidal geometries constitute a fundamental configuration for maintaining the stability of high temperature plasmas. Magnetic confinement devices such as *tokamaks* and *stellarators* employ toroidal magnetic fields to stabilize charged particles and sustain the conditions necessary for thermonuclear fusion [92]. The term tokamak originates from a Russian acronym meaning “toroidal chamber with magnetic coils". Developed over the

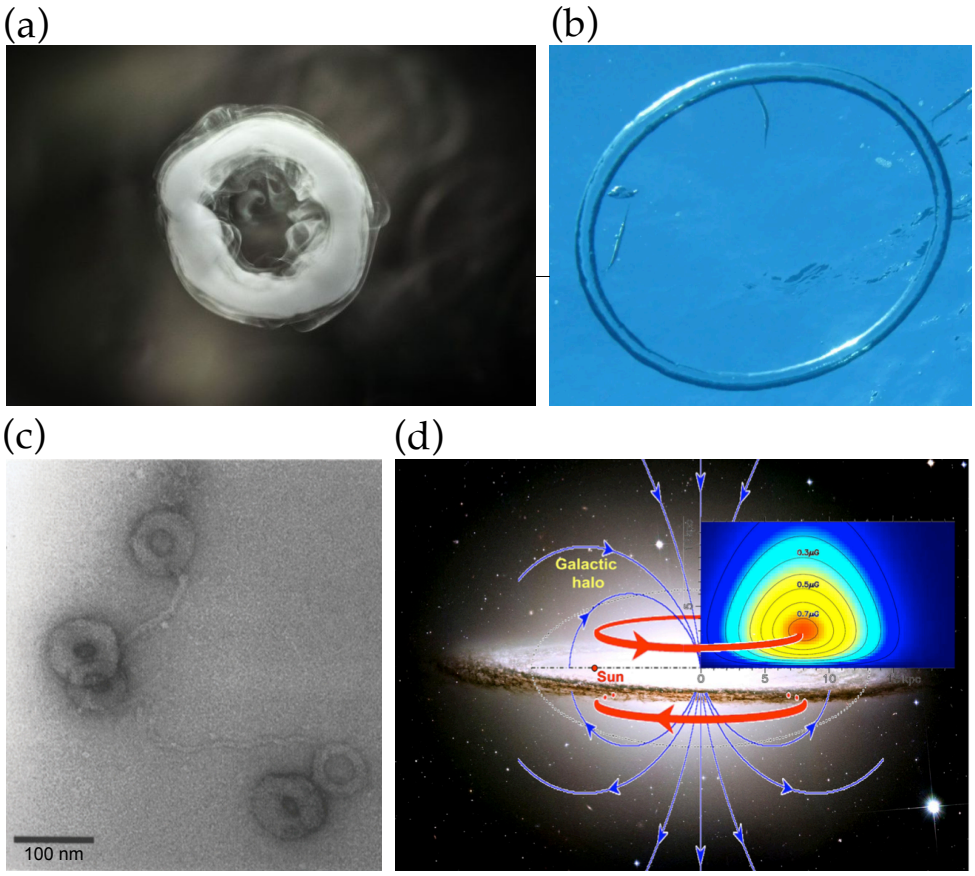

FIGURE 1.6: Toroidal structures in nature. (a) Smoke and (b) water vortex ring. (c) Experimental observation of condensed DNA imaged using transmission electron microscopy (TEM). Extracted from Ref. [90]. (d) Illustration of the magnetic field structure in the Galactic halo. Red (blue) lines indicate the toroidal (dipolar) fields. Extracted from Ref. [91].

past five decades, these systems represent one of the most sophisticated technological realizations of toroidal order in macroscopic physics. In such devices, the plasma is confined within a closed toroidal chamber and follows helical magnetic field lines that prevent particle loss, maintaining the high densities and temperatures required for fusion. Although tokamaks have successfully achieved controlled thermonuclear reactions and extended confinement times, no device to date has reached net energy gain, as the energy input still exceeds the fusion output. Nevertheless, the continuous progress in experimental design particularly with next generation facilities such as ITER toroidal magnetic confinement as the most promising route toward sustainable fusion energy [93]. Beyond the physical realm, toroidal structures also emerge in abstract mathematical and theoretical frameworks. In topology, the torus represents the canonical compact manifold generated by identifying opposite edges of a periodic domain, as commonly implemented in numerical simulations and condensed matter models, the so-called "periodic boundary conditions" [94], while in string theory, toroidal compactification provides a means of reconciling extra spatial dimensions with observable reality [95]. Even in computational and neural architectures, toroidal connectivity is employed to eliminate boundary effects and preserve translational symmetry [96]. Thus, the torus extends far beyond geometry, serving as a universal paradigm linking periodicity, symmetry, and continuity across both

physical and abstract systems.

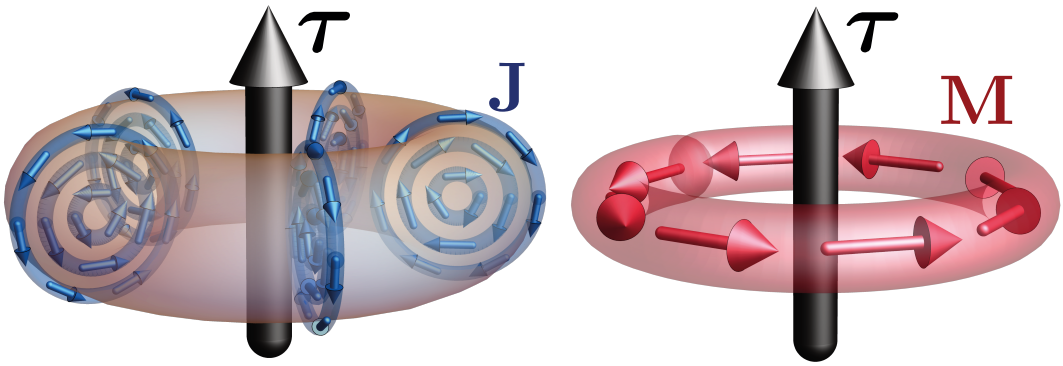

FIGURE 1.7: Illustration of toroidal moments in condensed matter. (Left panel) Toroidal moment (black central arrow) generated by any kind of circulating current distribution **J** (blue arrows). (Right panel) Toroidal moment originated from a circulating magnetization **M** (red arrows). Figure adapted from Ref. [97].

In condensed matter systems, which are our main focus here, the circulation of electric currents or rotating magnetization within a confined region gives rise to a specific toroidal quantity known as the *toroidal moment*. This is an axial vector that breaks both time-reversal and spatial-inversion symmetries [33, 98, 99]. The concept was originally introduced in nuclear physics to describe unusual current configurations that cannot be represented by standard electric or magnetic multipoles [98]. A toroidal moment can be pictured as a poloidal arrangement of magnetic dipoles forming a closed loop, similar to currents circulating around a torus, as can be illustrated in Fig. 1.7. Because this configuration lacks both inversion and time-reversal symmetry, the toroidal moment exhibits transformation properties distinct from conventional electric or magnetic dipole and quadrupole moments [33]. Later, the idea of toroidal multipoles was extended to condensed matter physics, where they act as independent order parameters in multiferroic and magnetoelectric materials [100–102]. In these systems, the toroidal moment often originates from noncollinear arrangements of magnetic dipoles and may give rise to unconventional linear magnetoelectric effects [103, 104], nonreciprocal optical responses [32, 105], and directional dichroism [106, 107], all of which are highly relevant for developing materials with tailored electromagnetic properties.

Focusing on the ferroic aspect of toroidal moment and its relationship with the magnetoelectric effect, it has been mentioned in the literature that an antisymmetric contribution to the magnetoelectric tensor indicates the presence of a toroidal moment [33]. However, a magnetoelectric response is not sufficient to prove ferrotoroidicity. Two verifications are mandatory: (i) there must be regions or domains with different orientations of the order parameter, and (ii) there must be hysteretic behaviour of these domains as a function of a conjugate external field between opposite single domains. The first condition was verified by Van Aken *et al.* [101], who investigated the toroidicity in the magnetoelectric compound $LiCoPO_4$ presenting magnetic vortex patterns, using Second Harmonic Generation (SHG) microscopy [105]. SHG is a powerful optical technique for imaging ferroic domain structures: an incident electromagnetic field $\mathbf{E}(\omega)$ at frequency ω induces a polarization $\mathbf{P}(2\omega)$ at twice the frequency, which acts as a source of frequency doubled radiation [108, 109]. The nonlinear polarization is given by $\mathbf{P}(2\omega) = \epsilon_0 \hat{\chi}\, \mathbf{E}(\omega)\mathbf{E}(\omega)$ [101, 110], where $\hat{\chi}$ is the second-order nonlinear susceptibility tensor. The allowed components of $\hat{\chi}$

are dictated by the crystal symmetry, including the symmetry breaking associated with long range ferroic ordering, making SHG particularly suited to visualizing domains in systems with toroidal order. Whereas Van Aken *et al.* (2007) first imaged ferrotoroidic domains, it was not until 2014 that Zimmermann *et al.* [102] reported hysteretic switching in the same magnetoelectric compound, thereby establishing a key signature of ferroic order, specifically, ferrotoroidicity. Figure 1.8 presents some of the most significant findings reported by Zimmermann *et al.* Panels (a) and (b) illustrate the microscopic origin of the toroidal moment in $LiCoPO_4$, where two inequivalent pairs of Co^{2+} magnetic ions generate opposite toroidal contributions that do not fully cancel, resulting in a net toroidal moment. This leads to a ferrotoroidic crystal with distinct domains, as sketched in (c). Panel (d) shows the hysteretic SHG response under an external magnetic field with a fixed electric field, while (e) reveals the multi-domain structure observed in the material.

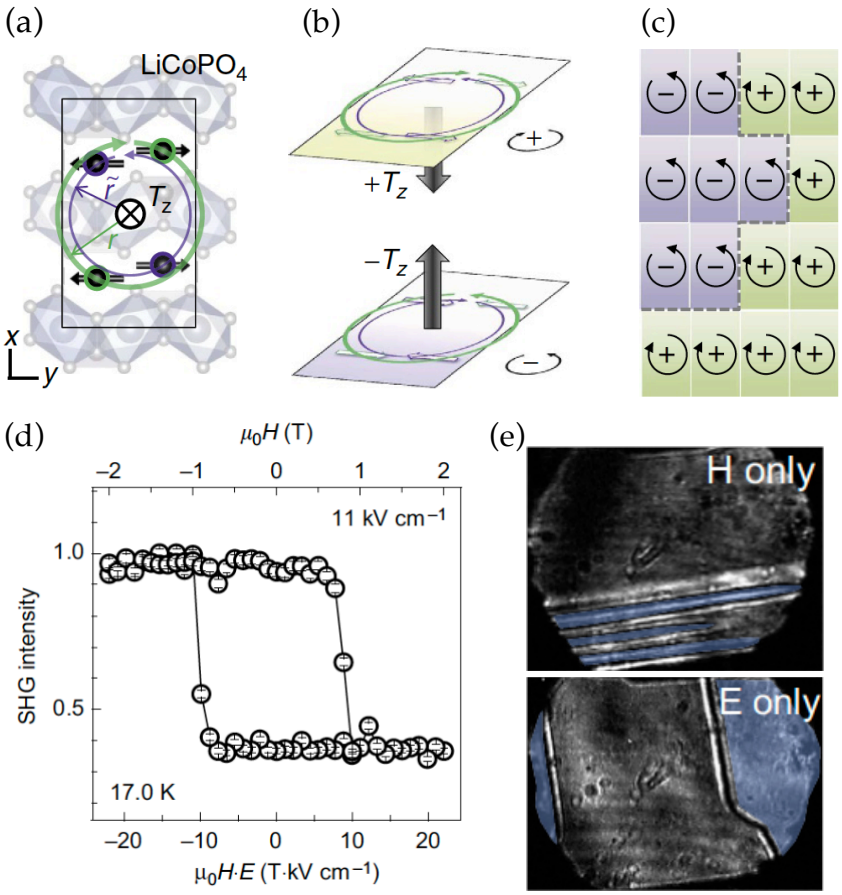

FIGURE 1.8: Toroidal moment (T) and ferrotoroidic order in $LiCoPO_4$. (a) Toroidal moment of the magnetic unit cell, consisting of two pairs of Co^{2+} ions located at different radial positions. (b) The two Co^{2+} spin pairs, highlighted in purple and green, contribute opposite T_z components; however, the difference in their radii $\tilde{r}$ and r prevents full cancellation, resulting in a net toroidal moment T_z parallel to the crystallographic z axis. (c) Schematic representation of a group of unit cells forming a ferrotoroidic crystal with domains in the xy plane. (d) Second harmonic generation intensity in dependence of a static magnetic field ($\mu_0 H_x$) and in the presence of a static electric field (E_y). (e) Multi-domain states after cooling the sample in a magnetic or electric field only where different colours indicate opposite domains. Figure adapted from Ref. [102].

Beyond static or quasi static magnetic structures, the concept of toroidal order has also recently gained attention in the dynamic regime, particularly within metamaterials such as photonics, phononics, and magnonics. In photonic systems, toroidal moments have been engineered using structured arrangements of resonators or split-ring antennas [111]. These so-called "artificial atoms" enable the realization of strong toroidal dipolar resonances, which are not typically dominant in natural materials. As a result, toroidal excitations provide access to highly confined electromagnetic modes, enhanced near-field effects, and novel regimes of light–matter interaction, with potential applications in sensing, lasing, and nonlinear optics. In magnonics, analogous principles emerge when spin waves are excited in the presence of a toroidal moment, leading to nonreciprocal propagation [18, 112, 113]. This nonreciprocal behavior has been observed when the toroidal moment has components parallel to the propagation of spin waves, as shown by Fogetti *et al.* [112]. They studied the multiferroic compound $LuFeO_3$, where the Fe ions form a two dimensional triangular lattice. In this geometry, competing magnetic interactions stabilize distinct spin configurations that generate toroidal and monopolar states, characterized by $\boldsymbol{\tau} \propto \sum \mathbf{r} \times \mathbf{M}$ and $a \propto \sum \mathbf{r} \cdot \mathbf{M}$, respectively. These configurations are shown in Fig. 1.9, where panels (a) and (c) display the corresponding spin textures, and panels (b) and (d) present the simulated inelastic neutron scattering spectra obtained from magnon dispersions. In the toroidal state [Figs. 1.9(a,b)], the toroidal moment is aligned along the crystallographic c axis (equivalent to the z axis), leading to a nonreciprocal magnon spectrum. By contrast, the monopolar configuration [Figs. 1.9(c,d)] exhibits a reciprocal dispersion. This suggests that engineering materials whose properties are based on the toroidal moments or higher order multipoles concepts may enable the realization of nontrivial functionalities, including nonreciprocal signal propagation or magnetoelectric coupling [112].

1.2.3 Gaps in the understanding of toroidal moments and spin-wave nonreciprocity

Despite being introduced more than 40 years ago and extensively studied in electromagnetic radiation, magnetoelectric, and multiferroic systems, the toroidal moment still presents significant open questions in its theoretical formulation and experimental verification. First, there is no consensus on a unique definition of the toroidal moment. As can be seen in the literature, different formalisms are employed, ranging from current density multipoles expansions [98] to discrete lattice sums [33, 114] and response function approaches [115]. These formalisms may not be equivalent and could yield different quantitative values, complicating comparisons across models and experiments. On the other hand, another difficulty is the choice of origin. The toroidal moment is not invariant under translations of the coordinate system. In finite systems, a shift of the origin changes the calculated value unless the net magnetic moment vanishes [99]. In periodic crystals, the situation is further complicated by ambiguities associated with the unit cell choice and surface termination, making the definition of a bulk toroidization multivalued. This lack of a standardized convention constitutes a major obstacle for establishing reproducible and origin independent measures of toroidal order or another interpretation is needed. Finally, the connection between the toroidal moments and spin-wave dynamics has been hardly explored [18, 106, 112, 113]. In principle, a finite toroidal moment breaks both inversion and time-reversal symmetries, which could generate k-odd terms in the magnon dispersion and thus contribute to nonreciprocal propagation. However, quantitative models linking a well-defined toroidal order parameter to measurable

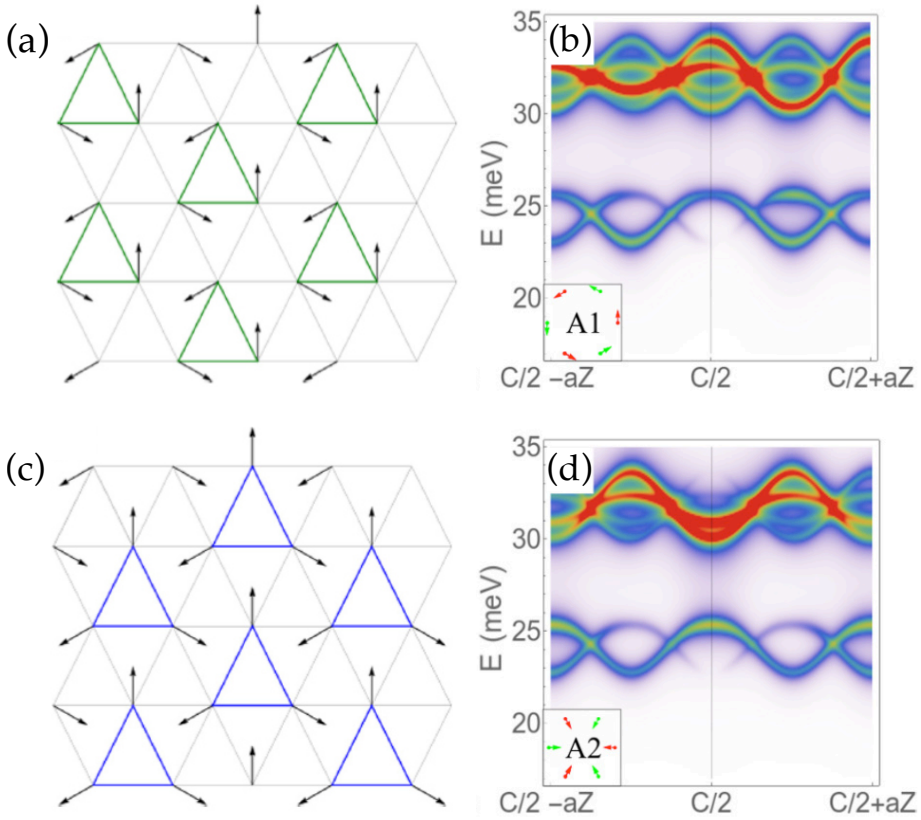

FIGURE 1.9: Toroidal (a) and monopolar (c) magnetic configurations in a 2D triangular lattice, together with their corresponding simulated inelastic neutron scattering (INS) spectra based on magnon dispersions, shown in panels (b) and (d), respectively. Spin waves propagate along the z axis. The toroidal state A1, whose toroidal moment is parallel to the z axis, exhibits a nonreciprocal magnon spectrum, whereas the monopolar state A2 displays a reciprocal one. Figure adapted from Ref. [112].

asymmetries in magnon spectra are scarce, and systematic experimental verification is still missing. Clarifying this link remains an open challenge, yet it is a crucial step to establish toroidal moments as a design principle for nonreciprocal magnonic devices.

1.3 Thesis Outline

The following presents the general outline of this thesis, which investigates the role of the toroidal moment in magnetic systems and its connection to spin-wave nonreciprocity.

The **Introduction** presents the motivation and objectives of the work, outlining the current state of magnonics as an active field in spin dynamics and information transport. The concept of toroidal structures is introduced and progressively focuses on the magnetic toroidal moment as a key quantity linking symmetry and dynamics, setting the basis for the study of nonreciprocal phenomena in magnetic media.

Chapter 2 develops the theoretical framework required for the analysis. It introduces the fundamentals of micromagnetic theory, including the main interactions and the Landau–Lifshitz–Gilbert equation, followed by a description of spin-wave dynamics and mechanisms leading to nonreciprocity. The concept of the toroidal moment is then formally presented, discussing its origins, definitions, and its relation to the dynamic magnetic tensor.

Chapter 3 focuses on the calculation of the toroidal moment in various magnetic systems. Two illustrative examples are first analyzed to introduce the formalism, which is then extended to magnetic textures, different geometries, and systems with graded magnetization, revealing how spatial variations generate effective toroidal moments.

Chapter 4 presents the main results of the publication *"Toroidal moments in confined nanomagnets and their impact on magnonics"* [97]. It establishes a link between the toroidal moment and asymmetric spin-wave propagation, examining different physical cases such as systems with electric currents, magnetic textures, graded magnetization, or Dzyaloshinskii–Moriya interactions.

Chapter 5 summarizes results from the work *"Curvature–induced parity loss and hybridization of magnons: Exploring the connection of flat and tubular magnetic shells"*[80], showing how geometric curvature alters static and dynamic magnetic properties. The transition from planar to curved geometries is analyzed, highlighting curvature as a source of parity breaking and nonreciprocal behavior.

Chapter 6 explores the dynamics of the *toroidization*. An equation analogous to the Landau–Lifshitz–Gilbert form is proposed. Also, the propagation of electromagnetic waves in toroidal media is discussed, illustrating potential nonreciprocal optical effects.

Finally, the thesis concludes with a synthesis of the results, emphasizing their implications for the understanding of the toroidal moment and nonreciprocity in magnetic systems, and suggesting directions for future research.

Chapter 2

Theoretical framework

2.1 Micromagnetism

Micromagnetism is a continuum theory that describes the static and dynamic behavior of magnetization in ferromagnetic materials at submicrometer length scales. It provides a framework bridging the gap between atomistic spin models and macroscopic magnetic behavior. Within this approach, the main order parameter is the *magnetization*, treated as a continuous vector field $\mathbf{M}(\mathbf{r}, t)$, typically expressed as $\mathbf{M}(\mathbf{r}, t) = M_\mathrm{s}\, \mathbf{m}(\mathbf{r}, t)$, where M_s denotes the saturation magnetization and $\mathbf{m}$ the unit vector indicating the direction of the magnetization. This field represents the density of magnetic moment at site $\mathbf{r}$ per unit volume within the material [116, 117].

Fundamentally, magnetization arises from quantum mechanical effects, primarily the intrinsic spin of electrons and their orbital motion around atomic nuclei. Nevertheless, in the present thesis, a classical description of magnetization is adopted, which, despite its simplicity, provides a powerful and sufficiently accurate framework for capturing the collective behavior of magnetic moments at the mesoscopic scale, i.e., from nanometers to a few micrometers. This classical treatment, which constitutes the foundation of micromagnetism, can be extended to describe other types of magnetic ordering, such as antiferromagnetism or ferrimagnetism, which will be discussed in subsequent sections.

The equilibrium configurations of the magnetization $\mathbf{M}(\mathbf{r})$ are obtained by minimizing the total magnetic energy, whereas its dynamics are governed by the Landau–Lifshitz–Gilbert (LLG) equation. The total energy of a micromagnetic system is typically expressed as the sum of several contributions, including the exchange energy, magnetostatic (or dipolar) energy, magnetocrystalline anisotropy energy, and Zeeman energy due to external magnetic fields. Another interaction that is central to the present study is the Dzyaloshinskii–Moriya interaction (DMI), which is an antisymmetric exchange energy term. All of them will be described in Subsection 2.1.2.

The following section delves deeper into the theoretical foundations and applications of micromagnetism that are relevant to the phenomena investigated in this thesis. It focuses on the key physical interactions that give rise to various magnetic orders and the formation of magnetic textures.

2.1.1 Magnetic orders

Magnetic ordering in solids arises from the collective behavior of electron spins, primarily influenced by exchange interactions. Depending on the nature of these interactions and the resulting alignment of magnetic moments, various types of magnetic orders can emerge, as can be seen in Fig. 2.1. In the following, the principal classes of magnetic order observed in magnetic materials are summarized and briefly detailed.

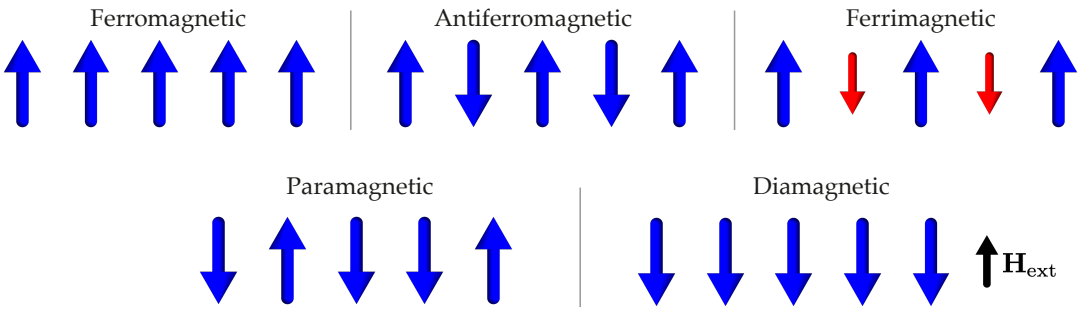

FIGURE 2.1: Schematic representation of different types of magnetic ordering for a chain of magnetic moments.

Ferromagnetism

Ferromagnetism is a fundamental type of magnetic ordering characterized by the parallel alignment of magnetic moments (also referred to as *spins*) within a material, resulting in a spontaneous net magnetization even in the absence of an external magnetic field. The magnetization $\mathbf{M}$ satisfies:

$$\mathbf{M} = (1/V)\sum_i \boldsymbol{\mu}_i \neq 0, \tag{2.1}$$

where $\boldsymbol{\mu}_i$ is the magnetic moment of the i-th ion or atom and V the sample volume. This collective behavior arises from exchange interactions that energetically favor parallel spin configurations among neighboring atoms or ions. Below a critical temperature known as the Curie temperature (T_C), thermal agitation is insufficient to disrupt this alignment, allowing the long-range magnetic order to emerge. Ferromagnetism is the microscopic origin of magnetization in conventional permanent magnets, and it plays a central role in numerous magnetic phenomena and applications, including magnetic storage and spintronic devices. Main examples include iron (Fe), cobalt (Co), as well as its alloys such as permalloy (Py) composed of iron and nickel, typically $Ni_{80}Fe_{20}$, and neodymium magnets (NdFeB) which are the strongest type of permanent magnet available commercially.

Antiferromagnetism

In compensated **antiferromagnetic** (AFM) materials, neighboring magnetic moments align antiparallel, resulting in a vanishing net magnetization

$$\mathbf{M} = (1/V)\sum_i \boldsymbol{\mu}_i = 0. \tag{2.2}$$

This configuration is stabilized by a negative exchange interaction, favoring antialigned spins. The order parameter is typically the Néel vector, defined as $\mathbf{L} = \mathbf{M}_A - \mathbf{M}_B$, where $\mathbf{M}_A$ and $\mathbf{M}_B$ denote the sublattice magnetizations. A prototypical example is manganese oxide (MnO), in which the AFM order is detectable via neutron diffraction due to the breaking of time-reversal and translational symmetry.

Unlike ferromagnets, compensated antiferromagnets possess no macroscopic magnetization, but they still exhibit long-range magnetic order below the Néel temperature (T_N).

Ferrimagnetism

Ferrimagnetism resembles antiferromagnetism in that magnetic moments are aligned antiparallel on distinct sublattices; however, the magnitudes of opposing moments are unequal, yielding a nonzero net magnetization

$$\mathbf{M} = (1/V)\sum_i \boldsymbol{\mu}_i \neq 0. \tag{2.3}$$

This unequal compensation arises due to the presence of chemically or crystallographically inequivalent magnetic ions, often occupying different lattice sites. Ferrimagnetic ordering is commonly observed in magnetic oxides such as magnetite (Fe_3O_4) and yttrium iron garnet ($Y_3Fe_5O_{12}$), where magnetic ions with different spin states are arranged in a specific geometric pattern.

A distinctive feature of some ferrimagnets is the presence of a *compensation temperature*, at which the sublattice magnetizations become equal in magnitude but opposite in direction, leading to a vanishing total magnetization despite the persistence of magnetic order. This phenomenon has significant implications for spin dynamics and magneto-optical effects. Ferrimagnetic materials are of particular interest in spintronic and magnonic devices due to their favorable combination of low damping, tunable magnetic properties, and the possibility of achieving ultrafast spin switching and spin-current generation.

Paramagnetism

Paramagnetism is a form of magnetic behavior characterized by the absence of spontaneous magnetization in the absence of an external magnetic field, while still exhibiting a weak, linear response to such a field. In paramagnetic materials, individual magnetic moments are randomly oriented due to thermal agitation, resulting in a zero net magnetization in equilibrium. When an external magnetic field is applied, these moments tend to align partially along the field direction, leading to a small induced magnetization.

From a thermodynamic perspective, paramagnetism represents a "high temperature disordered phase" of magnetic systems. It typically emerges above a critical temperature, denoted as the Curie temperature T_C for ferromagnets or the Néel temperature T_N for antiferromagnets, at which the system undergoes a second-order phase transition from an ordered magnetic phase to a disordered paramagnetic state. Below these temperatures, exchange interactions dominate thermal fluctuations and give rise to long-range magnetic order: parallel (antiparallel) alignment in ferromagnets (antiferromagnets), or more complex noncollinear configurations and other frustrated systems. Thus, paramagnetism serves as the common disordered phase from which various types of magnetic orders emerge upon cooling.

Diamagnetism

Diamagnetism is a fundamental and universal form of magnetic response observed in *all materials*, arising from the Lenz-law-type opposition of induced magnetic moments to an applied magnetic field. It originates from the modification of the orbital motion of bound electrons in the presence of an external magnetic field, which generates small induced magnetic dipoles oriented opposite to the field direction. It is typically a very weak effect, characterized by a small, negative magnetic susceptibility, and independent of temperature in most cases. Although often masked by

stronger paramagnetic or ferromagnetic responses in materials containing magnetic ions, diamagnetism becomes the dominant behavior in substances such as bismuth, graphite, or superconductors which are a special case of diamagnets [118].

These magnetic orders play foundational roles in the study of collective spin excitations, topological textures, and emergent phenomena such as nonreciprocal magnon transport and toroidal ordering, which are of central interest in modern spintronics and magnonics.

2.1.2 Magnetic interactions and micromagnetic energy terms

The behavior of magnetic textures at the mesoscale is governed by several fundamental interactions, which are incorporated into the micromagnetic energy functional. These interactions usually originate from atomistic or microscopic expressions and are translated into continuum field descriptions. In the micromagnetic framework, each contribution to the total energy density w, with $E = \int_V w \, \mathrm{d}V$, gives rise to an associated effective magnetic field, defined through the functional derivative

$$\mathbf{H}_i(\mathbf{r}) = -\frac{1}{\mu_0 M_\mathrm{s}} \frac{\delta w_i}{\delta \mathbf{m}(\mathbf{r})}, \tag{2.4}$$

where w_i denotes the energy density of the i-th interaction. The total effective field is then obtained as the superposition of all individual contributions,

$$\mathbf{H}_\mathrm{eff} = \sum_i \mathbf{H}_i. \tag{2.5}$$

This effective field is crucial for the Brown's equilibrium condition in the bulk, $\mathbf{M} \times \mathbf{H}_\mathrm{eff} = 0$, as well as in the context of the Landau-Lifshitz-Gilbert equation, which will be shown in the next section.

Symmetric exchange interaction

The symmetric exchange interaction originates from the spin-independent Coulomb repulsion between electrons, combined with the requirement that the total electronic wavefunction be antisymmetric under particle exchange. This antisymmetrization introduces an additional term in the total energy, known as the *exchange integral*, which depends on the relative orientation of the electron spins.

Although the Coulomb potential itself does not involve spin, the exchange energy arises due to quantum statistics and leads to an effective spin-spin interaction. This is the microscopic foundation of the Heisenberg exchange term,

$$E_\mathrm{ex} = -\sum_{\langle i,j \rangle} J_{ij} \, \boldsymbol{S}_i \cdot \boldsymbol{S}_j, \tag{2.6}$$

where the sign and magnitude of J_{ij} reflect the spatial overlap of electronic orbitals and the underlying Coulomb interaction. In the context of micromagnetism, J_{ij} is the exchange integral between spins at sites i and j, and $\mathbf{S}_i$ is a unit vector along the local spin direction. For ferromagnetic materials, $J_{ij} > 0$, favoring parallel alignment, as can be seen in Fig. 2.2, meanwhile for antiferromagnetic materials $J_{ij} < 0$ where antiparallel spins minimize the exchange energy.

In the continuum limit, this gives rise to the exchange energy,

$$\begin{aligned} E_{\text{ex}} &= A_{\text{ex}} \int \left[(\nabla m_x)^2 + (\nabla m_y)^2 + (\nabla m_z)^2 \right] \mathrm{d}V \\ &= A_{\text{ex}} \int_V (\nabla \mathbf{m})^2 \, \mathrm{d}V, \end{aligned} \tag{2.7}$$

where A_{ex} is the exchange stiffness, measured in J/m, and $\mathbf{m}(\mathbf{r})$ is the normalized magnetization field.

Dipolar interaction

The magnetostatic energy, also known as dipolar energy, originates from the classical interaction between magnetic dipole moments mediated by their associated magnetic fields. Each magnetic moment $\boldsymbol{\mu}_i$ generates a magnetic field that interacts with other moments $\boldsymbol{\mu}_j$, leading to an energy contribution that is long-ranged and strongly anisotropic.

In a discrete system of localized moments, the dipolar interaction energy between two magnetic dipoles $\boldsymbol{\mu}_i$ and $\boldsymbol{\mu}_j$ separated by a vector $\boldsymbol{r}_{ij} = \boldsymbol{r}_i - \boldsymbol{r}_j$ is given by,

$$E_{\text{dip}}^{(ij)} = \frac{\mu_0}{4\pi} \left[\frac{\boldsymbol{\mu}_i \cdot \boldsymbol{\mu}_j}{|\mathbf{r}_{ij}|^3} - \frac{3(\boldsymbol{\mu}_i \cdot \mathbf{r}_{ij})(\boldsymbol{\mu}_j \cdot \mathbf{r}_{ij})}{|\mathbf{r}_{ij}|^5} \right], \tag{2.8}$$

where μ_0 is the permeability of free space.

In the continuum approximation, for a magnetization field $\mathbf{M}(\mathbf{r})$, the total dipolar energy is expressed as [117]

$$E_{\text{dip}} = \frac{\mu_0}{2} \int_V \mathbf{M}(\mathbf{r}) \cdot \mathbf{H}_{\text{d}}(\mathbf{r}) \, \mathrm{d}V, \tag{2.9}$$

where $\mathbf{H}_{\text{d}}$ is the demagnetizing field, also called the stray field, generated by $\mathbf{M}(\mathbf{r})$ itself and is obtained from Maxwell's equations under the magnetostatic approximation,

$$\nabla \cdot \mathbf{B} = 0, \quad \nabla \times \mathbf{H}_{\text{d}} = 0, \quad \mathbf{B} = \mu_0(\mathbf{H}_{\text{d}} + \mathbf{M}). \tag{2.10}$$

This leads to a scalar magnetic potential Φ such that $\mathbf{H}_{\text{d}} = -\nabla\Phi$, and Φ satisfies:

$$\nabla^2 \phi = \nabla \cdot \mathbf{M}. \tag{2.11}$$

The nonlocal character of the dipolar interaction is a direct consequence of the long-range nature of the magnetic field generated by a dipole. As a result, the dipolar energy strongly depends on the sample geometry, boundary conditions, and spatial distribution of the magnetization, and it plays a critical role in determining equilibrium magnetization textures and spin-wave dynamics. Fig. 2.2 shows a configuration that minimizes the dipolar energy by closing the field lines and generating a vortex state.

Zeeman interaction

The Zeeman interaction describes the coupling between a collection of localized magnetic moments and an externally applied magnetic field. For a set of moments

$\boldsymbol{\mu}_i$ in an external field $\mathbf{H}_{\text{ext}}$, the Zeeman energy is given by

$$E_Z = -\mu_0 \sum_i \boldsymbol{\mu}_i \cdot \mathbf{H}_{\text{ext}}, \tag{2.12}$$

which is minimized when all moments are aligned parallel to the applied field. This interaction tends to orient the magnetic moments along $\mathbf{H}_{\text{ext}}$, as schematically indicated in Fig. 2.2. In the continuum limit of micromagnetism, the discrete moments are replaced by the magnetization field $\mathbf{M}(\mathbf{r})$, and the Zeeman energy takes the form

$$E_Z = -\mu_0 \int_V \mathbf{M}(\mathbf{r}) \cdot \mathbf{H}_{\text{ext}}(\mathbf{r})\, \mathrm{d}V. \tag{2.13}$$

This term favors configurations where $\mathbf{M}$ is parallel to $\mathbf{H}_{\text{ext}}$, competing with exchange, anisotropy and dipolar interactions in determining the equilibrium magnetic state.

Magnetocrystalline Anisotropy

Magnetocrystalline anisotropy describes the dependence of the magnetic energy on the orientation of the magnetization vector $\mathbf{m}$ relative to the crystallographic axes. It originates from the competition between electrostatic crystal-field interaction and spin-orbit coupling [119]. This effect defines energetically preferred directions (easy axes) for the magnetization, as illustrated in Fig. 2.2 for a vertical easy axis, where the magnetization may adopt two opposite orientations along this direction.

The most common forms of magnetocrystalline anisotropy are:

(i) Uniaxial anisotropy: Typical of hexagonal close-packed (hcp) crystals or thin films with out-of-plane symmetry, uniaxial anisotropy favors alignment along a single axis (commonly the c-axis). The corresponding energy is given by,

$$E_{\text{ani}}^{\text{uniaxial}} = -K_u \int_V (\mathbf{m} \cdot \hat{z})^2\, \mathrm{d}V, \tag{2.14}$$

where K_u, measured in $\mathrm{J/m^3}$, is the uniaxial anisotropy constant and $\hat{z}$ is the easy-axis direction.

(ii) Cubic anisotropy: Observed in cubic crystals such as body-centered cubic (bcc) Fe or face-centered cubic (fcc) Ni and Co, cubic anisotropy reflects the fourfold rotational symmetries of the lattice. The lowest-order cubic anisotropy energy density is:

$$E_{\text{ani}}^{\text{cubic}} = K_1 \int_V \left(m_x^2 m_y^2 + m_y^2 m_z^2 + m_z^2 m_x^2 \right) \mathrm{d}V, \tag{2.15}$$

where K_1, measured in $\mathrm{J/m^3}$, is the first-order cubic anisotropy constant. Higher-order terms may be included depending on the crystal symmetry and strength of spin–orbit coupling.

Sometimes the competition between dipolar coupling and uniaxial anisotropy is quantified using a quality factor Q by comparing the anisotropy energy and the magnetostatic energy, through the shape anisotropy. The simplest form can be written as $Q = 2K/(\mu_0 M_s^2)$, which was defined by Thiele in 1969 [120] in the context of cylindrical domains in infinite planar surfaces, however this term undergoes modifications for particular cases, especially in the case of extended nontrivial textures

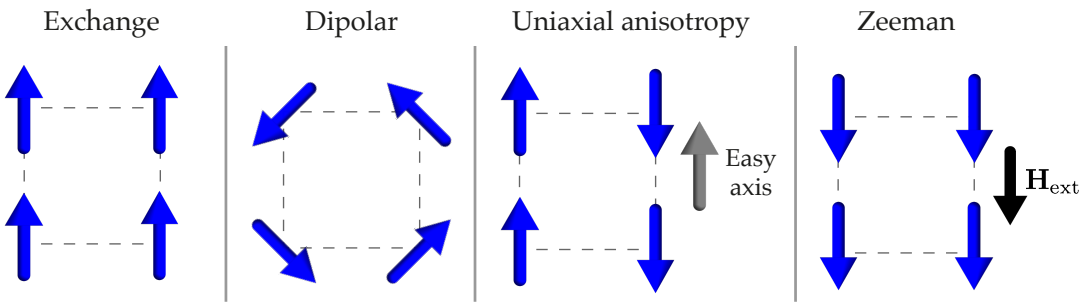

FIGURE 2.2: Schematic illustration of magnetic interactions and their effects on the alignments of magnetic moments.

[121]. The Q value allows to determine which interaction is predominant. For example, for $Q > 1$ the anisotropy dominates and the magnetization prefer to orientate along the anisotropy axis, usually the out-of-plane component or with uniform magnetization. In contrast, for $Q < 1$ the dipolar interaction dominates and magnetization may prefer in-plane orientations. Finally, for $Q \approx 1$ both interactions nearly compensate, enabling nontrivial magnetic textures and, in some cases, simplifying analytical calculations.

Dzyaloshinskii–Moriya Interaction (DMI)

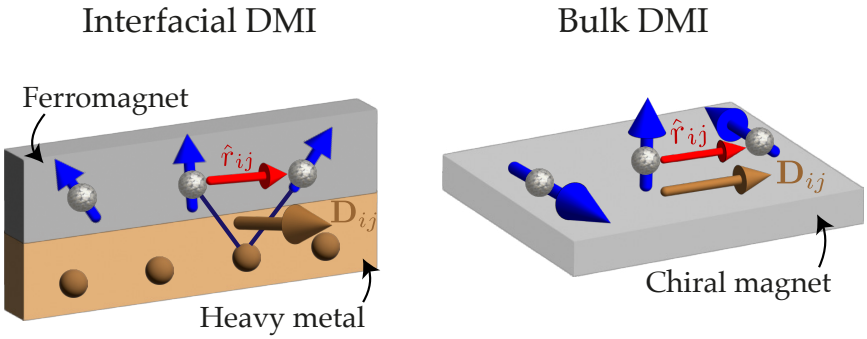

FIGURE 2.3: Schematization for the interfacial and bulk Dzyaloshinskii–Moriya interactions. The magnetic moments associated to each site in the ferromagnet/chiral magnet are shown in blue. In red the unitary vector connecting two consecutive sites and the DM vectors for each kind of interaction.

The Dzyaloshinskii–Moriya interaction (DMI) is an antisymmetric exchange interaction that arises due to the combined effect of strong spin–orbit coupling and broken inversion symmetry [30, 84, 89]. It favors noncollinear and chiral spin configurations and plays a crucial role in the stabilization of topological spin textures and in the propagation of the spin waves.

In its general discrete form, the DMI energy between two neighboring spins $\mathbf{S}_i$ and $\mathbf{S}_j$ is given by

$$E_{\text{DMI}} = \sum_{\langle i,j \rangle} \mathbf{D}_{ij} \cdot (\mathbf{S}_i \times \mathbf{S}_j), \tag{2.16}$$

where $\mathbf{D}_{ij}$ is the Dzyaloshinskii–Moriya vector, whose direction and magnitude are determined by the symmetry of the crystal lattice and the local environment [122]. From this equation it is evident that the minimum energy state does not occur for

parallel states, which is the case of symmetric exchange, but for spins that are oriented perpendicularly. However, due to competition with the other interactions the effect results in a tilting of the magnetization tending to form noncollinear magnetic textures [21, 61, 121, 123–125].

When moving to a continuous description, a Taylor expansion of the magnetization is needed and the DMI energy is expressed in terms of spatial derivatives. A convenient way to express this is through Lifshitz invariants [89, 121, 126]. The main advantage of this formalism is that by means of crystal symmetries it can be reduced to much simpler expressions. The two expressions most commonly used in the continuum to describe systems with Dzyaloshinskii–Moriya interaction are detailed below.

(i) Interfacial DMI (with C_{nv} symmetry): Interfacial DMI (i-DMI) arises in ultrathin magnetic films grown on heavy-metal substrates, where inversion symmetry is broken along the direction perpendicular to the interface, typically leading to C_{nv} point-group symmetry. It originates from the spin–orbit coupling at the interface and is particularly relevant in systems such as Pt/Co, W/CoFeB, and Ir/Fe bilayers [29, 30]. As illustrated in Fig. 2.3(a), the Dzyaloshinskii–Moriya vector $\mathbf{D}_{ij}$ is perpendicular to the plane defined by three atoms: two belonging to the ferromagnetic layer and one to the heavy-metal layer, and the resulting cycloidal spin texture is also shown.

In the continuum approximation, the interfacial DMI energy density can be written as,

$$E_{\text{i-DMI}} = D \int_V \left[m_z (\nabla \cdot \mathbf{m}) - (\mathbf{m} \cdot \nabla) m_z \right] \mathrm{d}V, \tag{2.17}$$

where $\mathbf{m}(\mathbf{r})$ is the normalized magnetization field, D is the interfacial DMI constant, measured in $\mathrm{J/m^2}$ and z the symmetry-breaking direction. This form favors Néel-type domain walls with fixed chirality, enabling the stabilization of skyrmions of the same kind and cycloidal spin spirals.

(ii) Bulk DMI (with chiral crystal symmetry, T or D_{2d} symmetries): Bulk DMI appears in noncentrosymmetric crystals where the entire crystal structure lacks inversion symmetry. This type of DMI is governed by the bulk crystal symmetry and is well described in materials with space groups such as T (tetrahedral) or D_{2d} [85, 126]. A prominent example is the B20 family of compounds (e.g., MnSi, FeGe, and FeCoSi), where the DMI gives rise to Bloch-type skyrmions and helical spin spirals. Fig. 2.3(b) shows the helical spin texture stabilized by b-DMI, together with the DM vector $\mathbf{D}_{ij}$ connecting two neighboring sites in a chiral magnet.

In the continuum limit, the bulk DMI energy density is typically written as

$$E_{\text{b-DMI}} = D \int_V \left[\mathbf{m} \cdot (\nabla \times \mathbf{m}) \right] \mathrm{d}V. \tag{2.18}$$

The magnitude of the Dzyaloshinskii–Moriya constant (D) differs significantly between interfacial and bulk systems. Interfacial DMI typically exhibits values in the range of 0.1–3 $\mathrm{mJ/m^2}$, depending on the choice of heavy-metal substrate and interface quality [29, 30]. In contrast, the values for DMI bulk are weaker. Usually on the order of 10^{-5} $\mathrm{J/m^2}$, i.e., two orders of magnitude smaller than for i-DMI. Apart from the interfacial and bulk forms, other symmetry classes can also host DMI, though these are less commonly studied [121, 122, 126]. Examples include systems with C_n symmetry, or materials with locally broken inversion symmetry due

to defects, strain gradients, or interface reconstructions. These may lead to complex forms of the $\mathbf{D}_{ij}$ vector fiel d and result in mixed or unconventional spin textures. Finally, it should be noted that the typical length of the period of textures originating from DMI is approximately $L = 4\pi A_{\text{ex}}/D$ [61, 124].

2.1.3 Magnetic Textures

The so-called *magnetic textures* are spatially inhomogeneous magnetization configurations that arise from the competition between magnetic interactions such as exchange, anisotropy, magnetostatic, and Dzyaloshinskii–Moriya. As shown in the previous section, all these interactions favor different magnetic orderings. If several are present, depending on the material of the magnetic sample, its geometry, external effects, etc., there will be a competition between these energy terms that can produce noncollinear magnetic textures. Unlike uniform ferromagnetic or antiferromagnetic states, magnetic textures exhibit nontrivial spatial profiles of the local magnetization field $\mathbf{M}(\mathbf{r})$. These textures are can be characterized by their symmetry, topology, dimensionality, among other proper parameters. Below, the most relevant magnetic textures in micromagnetism are summarized.

Domain Walls

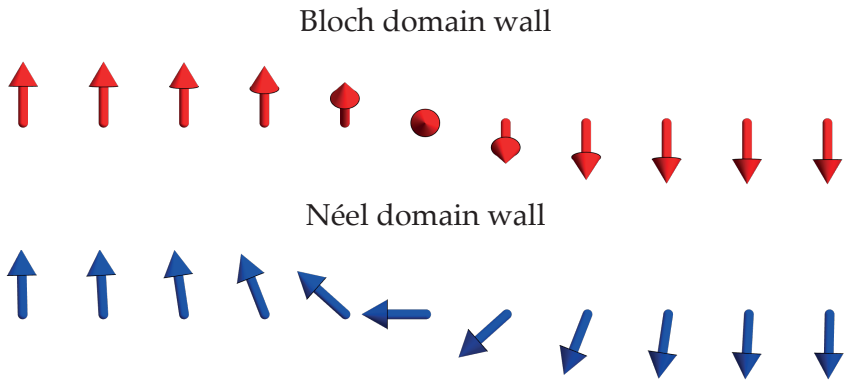

FIGURE 2.4: Bloch and Néel domain walls for a chain of magnetic moments.

Domain walls are transition regions separating uniformly magnetized domains [**domain wall**, 127, 128]. Their structure usually depends on the balance between exchange and anisotropy. In ferromagnets, two main types arise:

- **Bloch wall**: the magnetization rotates within the plane perpendicular to the wall normal. It is also referred typically as an helical rotation.
- **Néel wall**: the magnetization rotates in the plane of the wall, describing a cycloid along the rotation.

Fig. 2.4 schematizes both type of domain walls. Néel walls are favored in thin films due to surface dipolar fields, while Bloch walls typically appear in bulk materials also due to magnetostatic interaction [129–131]. However, in the absence of DMI, anisotropy allows one type to be switched to the other depending on the competition between interactions [132]. This changes in the presence of DMI, as it favors one type over the other: i-DMI facilitates the formation of Néel-type walls, while b-DMI favors Bloch [70, 133].

Magnetic Vortices and Merons

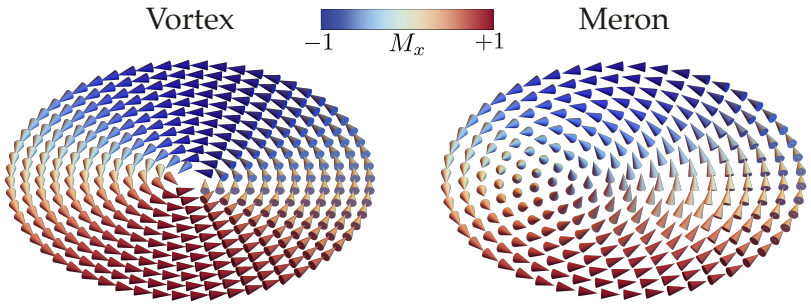

FIGURE 2.5: Vortex and meron magnetic states for a thin ferromagnetic disk. Meron is modeled according to the linear model. Magnetization is colored according to the $x-$component (in-plane).

Vortices are two-dimensional textures typically found in magnetic disks with a few nanometers thick. The magnetization curls homogeneously around a center and it is characterized by their chirality, whether it exhibits a clockwise or counterclockwise curling. At the center of these structures, exchange interactions produce magnetization that points outward from the plane [134, 135], and several models have been developed to describe the texture [see Ref. [135]]. A coreless vortex-type magnetization can be easily modeled using $\mathbf{M} = M_s\hat{\phi}$, being $\hat{\phi}$ the azimuthal unitary vector. When considering magnetization at the center, it is usually referred to as vortex-with-core or *meron*, which is a quasi-particle with half of the skyrmion topological number. The vortex and meron are illustrated in the Fig. 2.5. Furthermore, considering the core adds a new degree of freedom, whether it points up or down, called polarity. There are several ways to model a meron, and one of the simplest is through the linear model [136] given by

$$\mathbf{M} = M_s \begin{pmatrix} -\sin\theta\sin\phi \\ -\sin\theta\cos\phi \\ \cos\theta \end{pmatrix}, \tag{2.19}$$

where $\theta = \frac{\pi r}{2R}$ for $r \leq R$, being r the radial-coordinate and R the disk radius.

These structures minimize magnetostatic energy and are stable due to topological protection. Under certain excitations, such as spin waves or surface acoustic waves, the core can be displaced from the center, thus producing a gyroscopic motion, a nonlinear phenomenon that can be used in unconventional computing using the concept of reservoir computing [137, 138].

Skyrmionic textures

Skyrmions, in the context of magnetism, are two-dimensional topologically nontrivial solitons stabilized by the competition between exchange interaction, dipolar interaction, and the Dzyaloshinskii–Moriya interaction (DMI) [123, 139, 140]. They exhibit a swirling magnetization texture that resembles a circular domain wall, where the magnetization gradually rotates from up (or down) at the periphery to down (or up) at the core. This configuration is characterized by a quantized topological invariant, the skyrmion number. Magnetic skyrmions have been experimentally observed in chiral magnets [58, 139], tubes [64, 141], as well as in thin films and multilayers

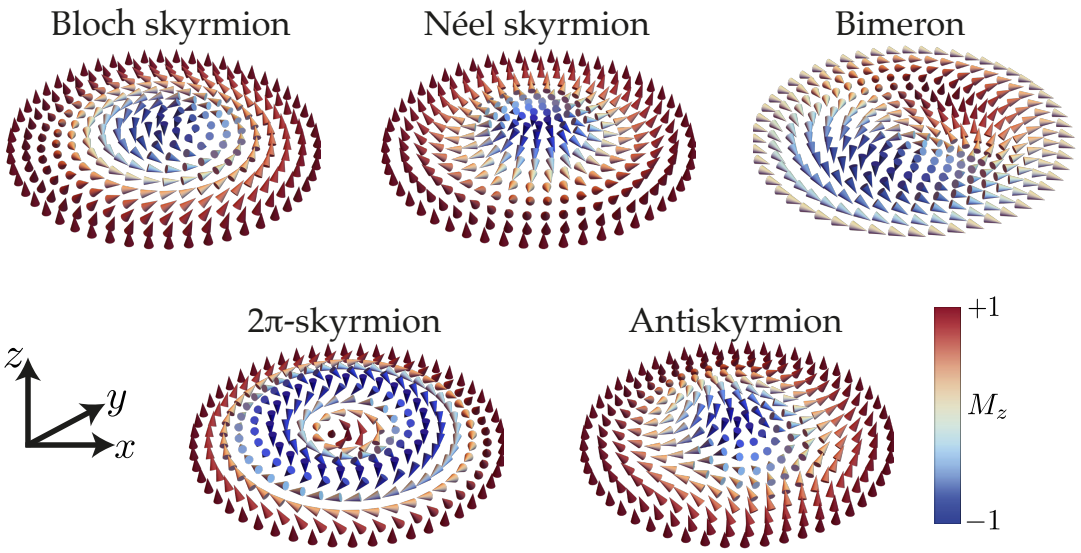

FIGURE 2.6: Skyrmionic textures confined in a nanodisk, based on analytical and approximated models. Magnetization is coloured according to the $z-$component.

with out-of-plane magnetization, typically under the influence of an external magnetic field and/or perpendicular uniaxial anisotropy [142, 143]. Depending on the magnetization rotation, skyrmions can be of Bloch- or Néel-type depending on the DMI symmetry, Bloch for bulk DMI or Néel for interfacial DMI [133, 143]. They are promising candidates for information storage and logic due to their nanoscale size, topological protection, and efficient current driven dynamics [61, 141, 144]. Recently, so-called $\ell\pi$-skyrmions or skyrmioniums have also been studied [145, 146], which correspond to skyrmions with a greater number of rotations between the core and the edge. Thus, the π-skyrmion refers to the traditional skyrmion, while the 2π-skyrmion refers to a skyrmionic texture whose center and edge point in the same direction. Another exciting textures that have been investigated recently are the *bimerons*. They are in-plane analogs of skyrmions, composed of a pair of merons (half-skyrmions) with opposite vorticity [147]. They can exist in centrosymmetric materials with frustrated exchange, as well they can emerge in materials with intrincated geometries. Antiskyrmions, in contrast, are topological structures with anisotropic winding which can be stabilized by DMI in materials with D_{2d} symmetry [148], or they can also be stabilized by dipolar interaction in heterostructured multilayers [149]. Fig. 2.6 schematizes these skyrmionic textures in nanodisks.

An more accurate analytical model for skyrmionic textures is still pending when the dipolar interaction is considered, despite the fact that they have been observed experimentally and can be easily simulated in computational environments such as MuMax3 or OOMMF. However, a general model with suitable approximations can be proposed as

$$\mathbf{M} = M_s \begin{pmatrix} \sin\theta(\mathbf{r})\cos(\phi+\gamma) \\ \sin\theta(\mathbf{r})\sin(\phi+\gamma) \\ \cos\theta(\mathbf{r}) \end{pmatrix}, \tag{2.20}$$

along the Cartesian x, y, and z axes, respectively, where ϕ is the azimuthal angle, $0 \leq \phi \leq 2\pi$, and γ is the helicity. The latter determines the skyrmion type, yielding

a Bloch skyrmion ($\gamma = \pi/2$) or a Néel skyrmion ($\gamma = 0$). What has been difficult for the scientific community to obtain is an exact function for $\theta(\mathbf{r})$ when the dipole-dipole term is present, nevertheless it can be approximated by some models. The simplest of all is the linear model, which is sufficient for the purposes of this thesis, given by $\theta(\mathbf{r}) = \pi(1 - r/\lambda)$ [150], with r the radial coordinate and λ is the characteristic texture period. Then, for any skyrmion we have $\mathbf{M}(r = \lambda) = -\mathbf{M}(0)$. The same expression can describe the antiskyrmion, by making $\phi \to -\phi$, while the bimeron texture is obtained by considering a $y-$axis rotation in 90°, which implies $M_x \to M_z$, $M_y \to M_y$ and $M_z \to -M_x$. From this, it is also possible to model Skyrmioniums or $\ell\pi-$Skyrmions ($\ell = 1, 2, 3...$) and $R = \ell\lambda$, if we consider that these textures stabilized in a disk with radius R.

Conical-Helical Textures

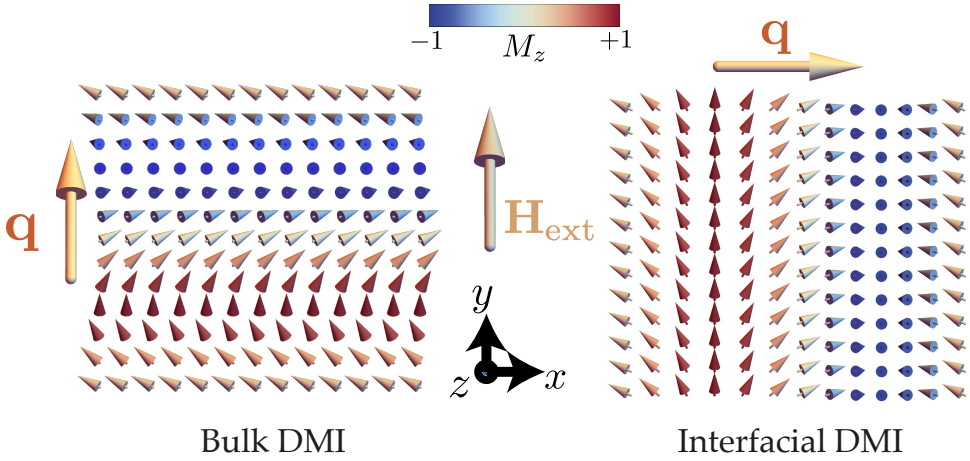

FIGURE 2.7: Conical–helical magnetic textures in a square thin film arising from bulk (left) and interfacial (right) Dzyaloshinskii–Moriya interactions. The external magnetic field $\mathbf{H}_{\text{ext}}$ fixes the pitch vector $\mathbf{q}$, which aligns parallel or perpendicular to the field depending on the interaction type. The magnetization is coloured according to the out-of-plane component m_z.

In chiral magnets such as materials with noncentrosymmetric crystalline symmetry, like FeGe or MnSi, or in ultrathin ferromagnetic films in contact with heavy metals like Pd, Pt or W, the DMI can stabilize modulated magnetic states such as the conical-helical states, which exhibit a periodic rotation of the magnetization vector along a pitch vector $\mathbf{q}$, as the ones shown in Fig. 1.4. These textures originate from the competition of several interactions where the DMI plays a key role. A conical-helical texture can be nucleated through the gradual lowering of a magnetic field along one direction in the plane. The competing values of DMI, uniaxial out-of-plane anisotropy, symmetric exchange and dipole-dipole interactions define the critical field and period of the texture. As the texture approaches zero field, a helix stabilizes, i.e., there is no component along the field. A usual way to describe these textures is through the following magnetization model [61, 124],

$$\mathbf{M} = \begin{pmatrix} \sin(\mathbf{q}\cdot\mathbf{r} + \psi)\sin\theta \\ \cos\theta \\ \cos(\mathbf{q}\cdot\mathbf{r} + \psi)\sin\theta \end{pmatrix}, \tag{2.21}$$

where the three components of **M** are taken along the Cartesian x, y, and z axes, respectively. Here $\mathbf{q}$ is the pitch vector, given by $\mathbf{q} = q(\sin\varphi_{\mathbf{q}}\hat{x} + \cos\varphi_{\mathbf{q}}\hat{y})$, with $\varphi = 0$ for i-DMI, standing for cycloidal texture meanwhile $\varphi = \pi/2$ for b-DMI, exhibiting helical textures. These configurations are illustrated in Fig. 2.7 for an applied field along $y-$direction. Nevertheless, in chiral magnets with C_n symmetry $0 \leq \varphi \leq \pi/2$ where two D strengths are present and the texture is a mix between the helical and cycloidal textures. The pitch vector magnitude is $q = 2\pi/\lambda$ with λ the texture period. This q, or equivalently λ, depends on the system's parameters and the interactions but it can be approximated by $q = D/2A_{\text{ex}}$, where D is the DMI strength and A_{ex} the exchange stiffness, however dipolar interaction modifies slightly this term [121, 124]. The phase ψ accounts for the competition between uniaxial anisotropy and dipolar interaction and can take 0 or $\pi/2$ values. Also, θ is the angle of the cone that the texture forms with the magnetic field, where $\theta = 0$ represents a uniform magnetization along the field, θ between 0 and $\pi/2$ is a conical state, and $\theta = \pi/2$ is a helix.

Hopfions

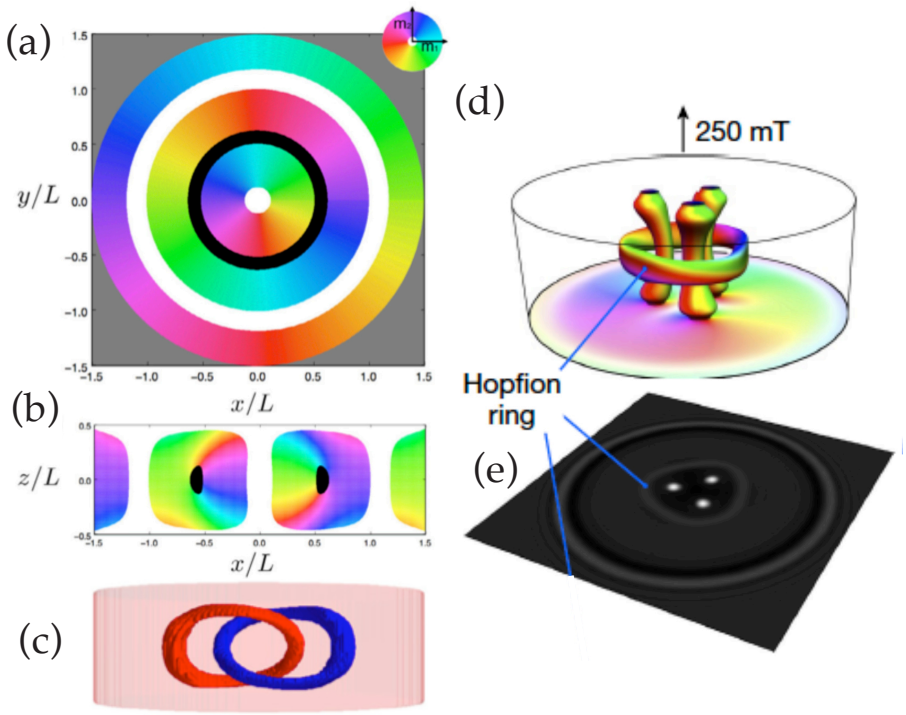

FIGURE 2.8: Hopfions numerically calculated and experimentally observed. (a) Numerically computed Hopfion in a cylinder of height L and diameter $3L$, at $z = 0$ and (b) at $y = 0$. (c) Shows two isosurfaces m_x = 0.9 (blue) and m_x = -0.9 (red). Adapted from Ref. [151]. (d) Simulated hopfion ring on three skyrmion strings formed in a disk with increasing field, showing the isosurfaces at $m_z = 0$. (e) Experimental over-focus Lorentz images of corresponding magnetic states in (d). Adapted from Ref. [152].

Hopfions are three-dimensional topological solitons in magnetic materials that can be regarded as closed, twisted skyrmion strings whose magnetization forms a toroidal, ring-like configuration. In contrast to skyrmions, which are essentially two-dimensional textures extended along one direction, hopfions are fully localized

in all three spatial dimensions. The existence of such structures in field theories was first proposed by Ludwig Faddeev in 1975, and they are now referred to as *hopfions* in recognition of Heinz Hopf, whose work established the homotopy classification underlying these configurations. Magnetic hopfions have been directly observed in chiral magnets, reproduced in numerical simulations, and described by suitable analytical models. They are currently regarded as promising candidates for three-dimensional spintronic applications [151, 152]. Figure 2.8 shows numerically calculated and experimentally observed Hopfions. Panels (a) and (b) present a numerically computed Hopfion confined to a cylinder of height L and diameter $3L$, visualized in the planes $z = 0$ and $y = 0$, respectively [151]. This state is further illustrated in panel (c) by the isosurfaces $m_x = 0.9$ (blue) and $m_x = -0.9$ (red). Panels (d) and (e) show a Hopfion ring formed on three skyrmion strings in a disk under increasing magnetic field [152] and with a particular protocol. The simulations in (d) display the isosurfaces at $m_z = 0$, while the over-focus Lorentz transmission electron microscopy (TEM) images in (e) reveal the corresponding magnetic configurations in experiment, following the same protocol as in simulations.

Magnetic states in thin tubes

Magnetic nanotubes support a variety of equilibrium magnetization states resulting from the competition between exchange, dipolar, and geometrical confinement effects [153]. The most fundamental is the vortex state, in which the magnetization curls around the tubular circumference, minimizing stray fields by avoiding surface magnetic charges. A related configuration is the *curling* (or *helical*) state, which can be regarded as a vortex state with an additional homogeneous magnetization component along the tube axis [79]. This hybrid character provides a compromise between flux-closure and longitudinal alignment, making it particularly relevant in elongated nanotubes. Vortex, curling and axial states can be described, in cylindrical basis $(\hat{\rho}, \hat{\phi}, \hat{z})$, by the following model

$$\mathbf{M} = M_s \begin{pmatrix} 0 \\ \chi \sin\Theta \\ \cos\Theta \end{pmatrix} \tag{2.22}$$

where χ is the helicity (± 1) around the z-axis, and Θ the constant angle between the equilibrium magnetization and the z-axis: $\Theta = \pi/2$ is the vortex state, $\Theta = 0, \pi$ the axial state, meanwhile any other Θ, represents a curling state, as is shown in Fig. 2.9.

Moreover, finite-length nanotubes often exhibit curling states at the nanotube ends, also known as closure caps, where the magnetization gradually bends at the extremities to close the flux and reduce magnetostatic energy [154–156]. These states not only govern the static properties of magnetic nanotubes but also strongly influence their spin wave spectrum and the emergence of nonreciprocal propagation phenomena. Nanotubes can also exhibit much more intricate states, such as conical-helical states, especially in the presence of Dzyaloshinskii–Moriya interaction, whether bulk or interfacial. The latter case will be discussed in more detail in the next chapter.

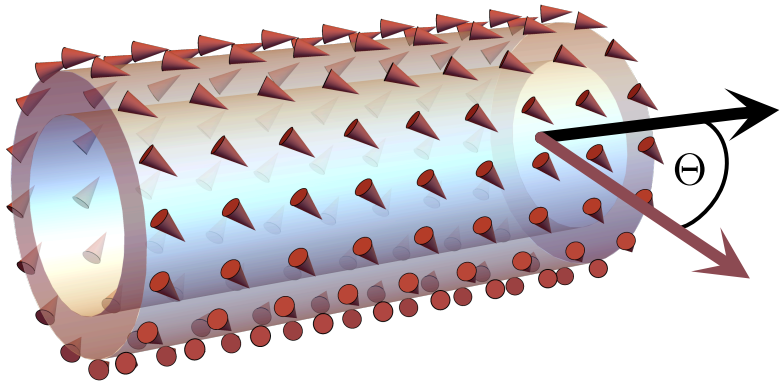

FIGURE 2.9: Ferromagnetic nanotube in a curling state for $\Theta = \pi/4$, where the black arrow indicates the z-axis and the magnetization distribution is shown in red.

2.2 Magnetization Dynamics and Spin Waves

2.2.1 Landau-Lifshitz-Gilbert (LLG) equation

The Landau-Lifshitz-Gilbert (LLG) equation is a fundamental equation in the field of magnetism, describing the dynamics of the magnetization vector $\mathbf{M}(\mathbf{r}, t)$ in response to magnetic fields, whether they are internal, such as the dipole or exchange fields, or external applied fields. Its origin traces back to the work of L. D. Landau and E. M. Lifshitz in 1935, who first proposed a phenomenological equation to model the precessional motion and relaxation of the magnetization (Eq. 21 from [157]). Later, in 1955, T. L. Gilbert introduced a modification in which the damping torque is proportional to the time derivative of the magnetization, leading to the now-standard form of the LLG equation. This damping term is introduced by using a Rayleigh dissipation function [158, 159].

The modern form of the LLG equation is written as

$$\frac{d\mathbf{M}}{dt} = -\gamma \mathbf{M} \times \mathbf{H}_{\text{eff}} + \frac{\alpha}{M_s} \mathbf{M} \times \frac{d\mathbf{M}}{dt}, \tag{2.23}$$

where γ is the gyromagnetic ratio, α is the dimensionless Gilbert damping parameter, M_s is the saturation magnetization, and $\mathbf{H}_{\text{eff}}$ is the effective magnetic field. This field typically includes contributions from external fields, exchange interactions, magnetic anisotropy, dipole-dipole interactions, and possibly Dzyaloshinskii–Moriya interactions (DMI) in systems with broken inversion symmetry.

The LLG equation serves as the foundation for understanding a wide range of dynamical magnetic phenomena. In the context of magnetic textures, such as domain walls, vortices, skyrmions or helices, it governs the collective motion and stability of these structures under various excitations, such as magnetic fields, spin polarized currents, or temperature gradients.

In magnonics, the LLG provides a reliable description of spin-wave dynamics. Spin waves are low-energy collective excitations of the magnetization field, and their quanta are the magnons. By linearizing the LLG equation around an equilibrium configuration $\mathbf{M}_0$, one obtains a set of linear differential equations that determine the spin wave dispersion relations and mode profiles. These results are used to study phenomena such as nonreciprocal spin wave propagation due to DMI or interfacial asymmetry, mode hybridization and magnon band structures in patterned media,

spin wave emission and scattering by dynamic or topological textures, thermally activated spin wave transport (magnon spin Seebeck effect).

2.2.2 Spin-wave modes

Spin waves can propagate in different configurations depending on the orientation of the static magnetization $\mathbf{M}_0$, usually parallel to the applied external field $\mathbf{H}_{\text{ext}}$, and wavector $\mathbf{k}$. Kalinikos and Slavin showed in Ref. [160] an analytical expression for the spin-wave dispersion relation for waves in waveguides with thickness d, much smaller than its width w, by considering uniform magnetization, homogeneous external applied field, exchange and dipolar interactions. The expression is given by [161],

$$\omega_n = \sqrt{(\omega_0 + \omega_M \lambda_{\text{ex}} \kappa^2)(\omega_0 + \omega_M \lambda_{\text{ex}} \kappa^2 + \omega_{\text{M}} F)}, \tag{2.24}$$

where $\omega_0 = \gamma \mu_0 H_0$, $\omega_M = \gamma \mu_0 M_{\text{s}}$ and,

$$F = P + \sin^2 \phi \left(1 - P\left(1 + \cos^2(\theta_k - \theta_M)\right) + \frac{\omega_M P(1-P)\sin^2(\theta_k - \theta_M)}{\omega_0 + \omega_M \lambda_{\text{ex}} \kappa^2}\right), \tag{2.25}$$

$$P = 1 - \frac{1 - e^{\kappa d}}{\kappa d}. \tag{2.26}$$

Additionally, $\kappa^2 = k^2 + k_n^2$, with $k_n = n\pi/w$ the quantized wavenumber along the width, corresponding to standing waves. k is the wavenumber along the propagation direction, $\theta_k = \arctan(k_n/k)$, ϕ the angle between the magnetization and the normal to the waveguide, and θ_M is the angle between the magnetization and the waveguide axis. The most common spin-wave configurations are the Damon–Eshbach (DE), Backward Volume (BV), and Forward Volume (FV) modes. Their corresponding dispersion relations are plotted in Fig. 2.10, using $\gamma = 186.6$ GHz/T, $M_{\text{s}} = 658$ kA/m, $A_{\text{ex}} = 11.1$ pJ/m, which gives $\lambda_{\text{ex}} \approx 6.39$ nm. $H_0 = \mu_0 B_0$, with $B_0 = 100$ mT, $d = 30$ nm and $w = 500$ nm.

Damon-Eshbach ($\theta_M = \pi/2$, $\phi = \pi/2$)

The Damon-Eshbach mode corresponds to surface spin waves propagating with the wavevector $\mathbf{k}$ perpendicular to the equilibrium magnetization $\mathbf{M}_0$, i.e., $\mathbf{k} \perp \mathbf{M}_0$, typically in an in-plane magnetized thin film. These modes are localized at different surfaces of the film, depending on the wavevector orientation, and decay exponentially into the bulk.

Backward-volume ($\theta_M = 0$, $\phi = \pi/2$)

In the Backward Volume (BV) configuration, the wavevector is aligned parallel to the magnetization, $\mathbf{k} \parallel \mathbf{M}_0$, and both lie in the film plane. These spin waves exhibit a negative group velocity in the dipolar-dominated regime, i.e., for small wavevectors k. This implies that the phase and group velocities are antiparallel.

Forward-volume ($\theta_M = \pi/2$, $\phi = 0$)

The Forward Volume (FV) geometry corresponds to the case where the static magnetization $\mathbf{M}_0$ is oriented perpendicularly to the plane of the magnetic film, and the

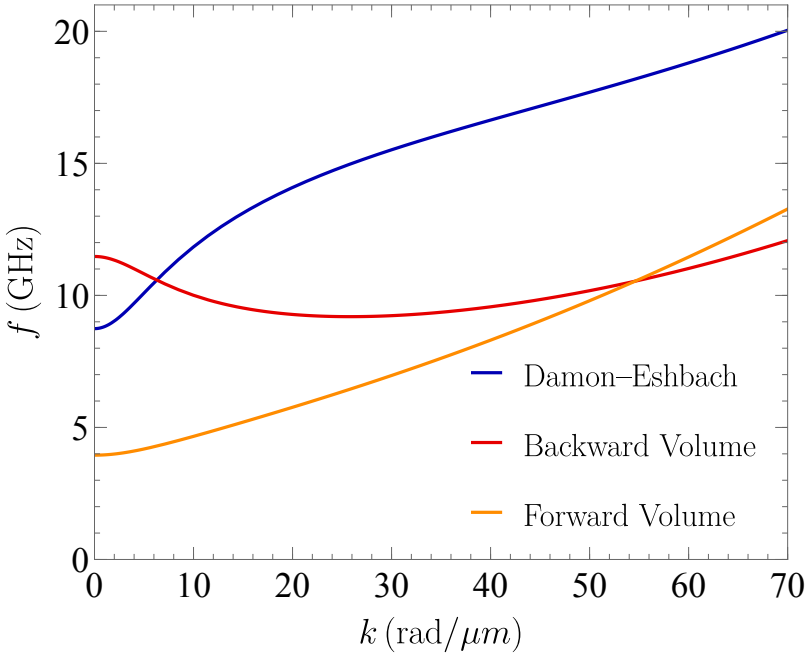

FIGURE 2.10: Spin-wave dispersion relations for the Damon–Eshbach (blue), Backward Volume (red), and Forward Volume (orange) geometries, by considering $n = 1$ in Eq. 2.24.

spin wave wavevector $\mathbf{k}$ lies within the film plane ($\mathbf{k} \perp \mathbf{M}_0$). This configuration can be realized experimentally by applying a strong out-of-plane magnetic field that overcomes the demagnetizing field.

2.2.3 Methods of Solution

Solving the LLG equation can be highly nontrivial due to its nonlinear and vectorial nature. The choice of method depends on the specific problem:

- **Analytical methods:** In simplified geometries or for small-amplitude excitations, it is possible to linearize the LLG equation and solve it analytically. This is commonly done to obtain spin wave spectra in uniform infinite films and cylindrical shells, or in periodic media [162, 163].
- **Plane Wave Method (PWM):** For periodic or quasi-periodic systems, Bloch's theorem can be used to reduce the problem to an eigenvalue formulation in momentum space, which is particularly useful for calculating magnon band structures in magnonic crystals [47, 48].
- **Dynamic Matrix Method (DMM):** The Dynamic Matrix Method is a numerical approach commonly used to compute the spin-wave eigenfrequencies and mode profiles in discretized magnetic media. It is based on the linearization of the LLG equation around the equilibrium magnetization configuration. Assuming small-angle precessions, the magnetization vector is decomposed as $\mathbf{M}(\mathbf{r}, t) = \mathbf{M}_0(\mathbf{r}) + \delta\mathbf{m}(\mathbf{r}, t)$, where $\delta\mathbf{m} \perp \mathbf{M}_0$ is treated as a harmonic perturbation. The resulting linearized equations are discretized in space, employing finite difference or finite element methods, leading to a generalized eigenvalue problem [17, 164].

- **Micromagnetic simulations:** Full numerical integration of the LLG equation can be performed using finite-difference or finite-element discretization schemes. Micromagnetic solvers such as `OOMMF` [165], `MuMax3` [166] or `FinMag` [167] are widely used to simulate the generation of spin waves over complex geometries, patterned materials or nontrivial magnetic textures. In general, by performing a Fast Fourier Transform (FFT) in space and time of the recorded data during a simulation, allows to obtain the spin-wave dispersion relation.

2.2.4 Nonreciprocity and dispersion asymmetries

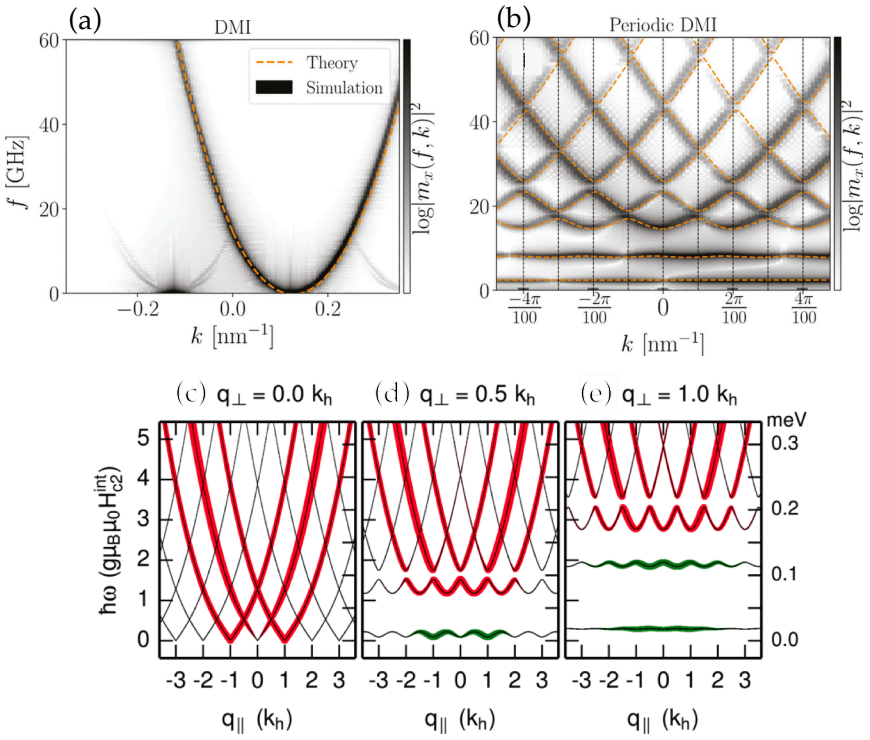

FIGURE 2.11: Spin-wave dispersions for three representative systems. (a) Ferromagnetic thin film with uniform interfacial Dzyaloshinskii–Moriya interaction (i-DMI). (b) Magnonic crystal with spatially periodic i-DMI. (c–e) Helimagnon spectra in the chiral magnet MnSi, where spin waves, with wavevector $\mathbf{q} = (\mathbf{q}_{\parallel}, \mathbf{q}_{\perp})$ are excited on a periodic helix along $\mathbf{k}_h \parallel \mathbf{q}_{\parallel}$ for different values of $\mathbf{q}_{\perp}$. Panels (a–b) are adapted from Ref. [29], and panels (c–e) from Ref. [65].

The nonreciprocity of spin waves refers to the situation where two counter-propagating waves with same wavevector magnitude, i.e, when comparing $+k$ and $-k$, exhibit different frequencies [8, 11]. This effect arises from broken spatial symmetries and is also intimately related to chirality, the lack of equivalence between an object and its mirror image after spatial operations [77, 168]. In magnetic systems, long-range dipolar interactions can induce chirality, as well as relativistic spin-orbit coupling in noncentrosymmetric crystals or interfaces, giving rise to Dzyaloshinskii–Moriya interactions [77]. Furthermore, as discussed in previous sections, these interactions can stabilize magnetic textures under specific conditions, such as upon crossing a critical field. Remarkably, the characteristics of spin waves can be imprinted onto the properties of these textures through magnetic phase transitions, for instance, by reducing the external field from a saturated state [124, 169]. Figure 2.11 shows the

spin-wave dispersion in systems with Dzyaloshinskii–Moriya interaction (DMI): (a) Nonreciprocal dispersion in a thin film with interfacial DMI (i-DMI), where the magnetization is saturated along the external field and oriented perpendicular to the propagation direction (Damon–Eshbach geometry) [89]. (b) Similar film geometry but with a spatially periodic DMI, forming a DMI-based magnonic crystal. In this case, flat bands and band folding arise due to the periodic modulation [29]. (c–e) Spin waves excited in a helical magnetic state (helimagnons) in the chiral magnet MnSi, governed by bulk DMI (b-DMI). The resulting dispersion for helimagnons exhibits features analogous to those of the magnonic crystal due to the periodicity of the magnetic textures [61, 65].

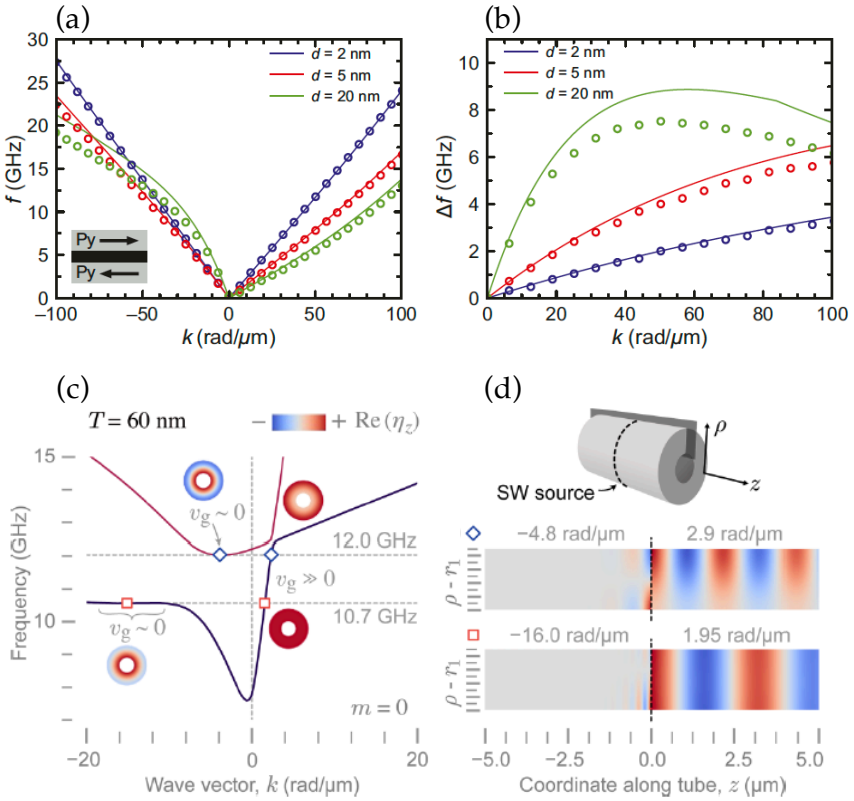

FIGURE 2.12: Two magnetic systems exhibiting dipolar-induced nonreciprocity. (a) Spin-wave dispersion relation for a bilayer magnetized antiparallel in a Damon–Eshbach configuration, (b) and the corresponding frequency shift between counter-propagating modes, adapted from Ref. [25]. (c) Spectrum for a thick ferromagnetic nanotube showing only two modes. (d) Spatial profiles of spin waves excited at selected frequencies, evidencing unidirectional propagation, adapted from Ref. [18].

In extended films, dipolar coupling across the film thickness gives rise to nonuniform internal fields. As a result, surface spin waves (MSSWs) acquire asymmetric profiles along the thickness, leading to characteristic asymmetries in the spin-wave amplitudes, even in centrosymmetric materials [76]. This symmetry breaking can also be achieved through grading the material properties, such as a variation of the saturation magnetization or anisotropy along the thickness, which may result in spin-wave nonreciprocity [22, 23]. These nonreciprocal effects are also noticeable in layered and three-dimensional nanomagnetic systems. For example, in antiferromagnetically coupled bilayers, interlayer dipolar coupling produces pronounced

frequency asymmetries between opposite propagation directions, enabling unidirectional magnon transport without the presence of interfacial DMI [24–28]. Similarly, in curved nanostructures such as nanotubes or spherical shells, geometry itself breaks inversion symmetry, and dipolar interactions induce strong asymmetric dynamics, including nonreciprocal domain-wall motion [128, 170], and asymmetric spin-wave propagation [14–21]. Fig. 2.12 illustrates the spin-wave properties of two of these cases. Fig. 2.12 (a-b) shows the dispersion relation and frequency shift for a ferromagnetic bilayer aligned antiparallel, and (c-d) shows the spectrum and the spin-wave magnetization profile for some modes in a ferromagnetic thick nanotube. In addition to these cases, spectral asymmetry can also emerge from dipolar interactions when material parameters such as the saturation magnetization M_s are spatially modulated [171].

2.3 Toroidal Moment and Symmetry-Breaking Effects

2.3.1 Origins of the toroidal moment

The origins of the toroidal moment lie in the multipole expansions of electromagnetic quantities. One of the earliest approximations to this concept was introduced by Zel'dovich in 1957, who, in the context of parity violation in elementary particles, defined the anapole term. This concept is now featured in several modern electrodynamics texts, such as *Modern Electrodynamics* from Zangwill [118]. Later, Dubovik et al. connected this anapole moment to a family of polar toroidal multipole moments [98], where "polar" refers to the transformation under parity as a polar vector, and "toroidal" highlights the intuitive link with current distributions shaped like a torus. A second family, known as axial toroidal moments, can also be defined. The key difference lies in their symmetry properties: axial toroidal moments are even under both parity and time reversal, while polar toroidal moments are odd under both operations. Axial toroidal moments are typically associated with circulating electric polarization, whereas polar toroidal moments are linked to circulating magnetization. In this thesis, we focus on the latter polar toroidal moments and, for simplicity, we will refer to them simply as toroidal moments throughout the text. The toroidal moment is defined as [98]

$$\boldsymbol{\tau} = \frac{1}{10} \int \left[\mathbf{r}(\mathbf{r} \cdot \mathbf{J}(\mathbf{r})) - 2r^2 \mathbf{J}(\mathbf{r}) \right] \mathrm{d}V, \tag{2.27}$$

which is integrated over a unit cell. Here, $\mathbf{J}$ can be referred to an electrical free current $\mathbf{J}_f$, a polarization current given by $\mathbf{J}_p = \partial \mathbf{P} / \partial t$ or the (magnetic) bound currents $J_M = \nabla \times \mathbf{M}(\mathbf{r})$ in the presence of magnetic matter. Notice that this bound current only emerges for inhomogeneous magnetization, from which one can anticipate that textures with any sort of curling magnetization will have an associated toroidal moments.

2.3.2 Symmetry breaking and associated phenomena

The toroidal moment has been associated with symmetry-breaking phenomena and, consequently, with nonreciprocal effects as well as the magnetoelectric effect. Particularly, spatial symmetry breaking and temporal reversal can simultaneously lead to nonreciprocity, and the literature indicates that the presence of the toroidal moment accuses these symmetry breaks [18, 81]. In magnetic materials with a finite toroidal moment according to their equilibrium magnetization, it has been observed that

both the light interacting with the sample and the magnetic excitations (magnons) can exhibit nonreciprocal behavior under certain conditions. This asymmetry in the dispersion occurs if $\boldsymbol{\tau} \cdot \mathbf{k}$. This is because no combination of symmetry operations such as translations, rotations, reflections or spatial inversions can map and reverse directions in the presence of $\boldsymbol{\tau}$. Then, $\mathbf{k} \to -\mathbf{k}$ are not symmetry-equivalent, enabling directional anisotropy, as referred in some works [107], or simply nonreciprocity.

It has been proposed that the toroidal moment, and the associated ferrotoroidicity, constitutes a new type of ferroic order that violates both spatial and temporal inversion symmetries. As a result, it may give rise to a magnetoelectric response described by the relation $\alpha_{ij} = \varepsilon_{ijk} T_k$, where α_{ij} is the magnetoelectric tensor, ε_{ijk} is the Levi-Civita tensor, and $\mathbf{T}$ is the toroidal moment density (or toroidization). Therefore, despite the presence of a magnetoelectric response can indicate the existence of a toroidal moment, two conditions must be fulfilled to conclusively demonstrate ferrotoroidicity: (a) the existence of domains, and (b) a hysteretic switching of these domains under the action of the conjugate external field.

The existence of ferrotoroidics domains was demonstrated by Van Aken *et al.* in 2007 [101], and the hysteretic behavior was shown by Zimmermann *et al.* in 2014 [102]. In both studies, the ferrotoroidicity of $LiCoPO_4$ in its magnetic vortex state was investigated using optical second-harmonic generation (SHG). In 2021, Mund *et al.* [105] demonstrated a nonreciprocal SHG mechanism in the antiferromagnetic compound CuB_2O_4. SHG is a nonlinear optical process in which a crystal irradiated with light at frequency ω emits light at the doubled frequency 2ω. The nonlinear susceptibility tensor $\chi^{(2)}$ governing SHG is strongly determined by the crystal symmetry. According to Neumann's principle, any long-range ordering that alters the symmetry of a material will influence the nonzero components of the SHG tensor [172]. From a microscopic point of view, the toroidal moment can be written as $\boldsymbol{\tau} = -g\mu_B \sum_i \mathbf{r}_i \times \mathbf{S}_i$, where $\mathbf{r}_i$ is the position vector, $\mathbf{S}_i$ the spin, g the Landé g-factor, and μ_B the Bohr magneton. This toroidal moment can be understood as an effective built-in vector arising from spin-orbit interaction [32], and it can couple to the vector potential of incident light. This coupling enables SHG when the toroidal moment $\boldsymbol{\tau}$ is aligned parallel to the electric field $\mathbf{E}_\omega$ (or vector potential $\mathbf{A}_\omega$) of the incoming light.

2.3.3 Volume and surface toroidal moment

For magnetic matter, the bound current is $\mathbf{J}_\mathrm{b} = \nabla \times \mathbf{M}$. Then, in the absence of free and polarization currents, $\mathbf{J} = \mathbf{J}_\mathrm{b}$ and the magnetic contribution to the emergent toroidal moment is given by $\boldsymbol{\tau} = \frac{1}{10} \int \left[\mathbf{r}(\mathbf{r} \cdot (\nabla \times \mathbf{M})) - 2r^2 \nabla \times \mathbf{M}\right] \mathrm{d}V$. By utilizing standard vector identities (further details in Appendix A), $\boldsymbol{\tau}$ splits into volumetric and surface contributions $\boldsymbol{\tau} = \boldsymbol{\tau}^\mathrm{v} + \boldsymbol{\tau}^\mathrm{s}$, where

$$\boldsymbol{\tau}^\mathrm{v} = \frac{1}{2} \int (\mathbf{r} \times \mathbf{M}) \, \mathrm{d}V, \tag{2.28}$$

which has been also obtained by a multipole expansion of the vector potential [33, 99]. Eq. (2.28) has been widely used for calculating $\boldsymbol{\tau}$ in magnetic structures [102, 114, 168, 173, 174]. Indeed, the microscopic version of the toroidal moment arises from Eq. (2.28) [99]. On the other hand,

$$\boldsymbol{\tau}^\mathrm{s} = -\frac{1}{10} \oint_{\partial V} \left[\mathbf{r} \, (\mathbf{r} \cdot \mathbf{K}_\mathrm{b}) - 2r^2 \mathbf{K}_\mathrm{b}\right] \mathrm{d}S \tag{2.29}$$

is due to surface-bound current $\mathbf{K}_b = \mathbf{M} \times \hat{n}$, with $\hat{n}$ a unit vector normal to the local surface. Notice that $\boldsymbol{\tau}^s$, which has not been reported before, is analogous to Eq. (2.27) but with a closed surface integral and opposite sign. Nonetheless, there is an alternative definition for the toroidal moment [33, 115] given by

$$\boldsymbol{\tau}' = (1/6) \int [\mathbf{r} \times (\mathbf{r} \times \mathbf{J})] \mathrm{d}V, \tag{2.30}$$

which gives $\boldsymbol{\tau}' = (1/3)\boldsymbol{\tau}^v - (5/3)\boldsymbol{\tau}^s$, where $\boldsymbol{\tau}^v$ and $\boldsymbol{\tau}^s$ are the moments found before. The toroidal moment $\boldsymbol{\tau}$ and $\boldsymbol{\tau}'$ are equivalent when averaged over time if only free currents are considered [33]. Still, without this temporal average, there is a significant difference due to the surface term. Fig. 2.13 illustrates the physical origin of the toroidal moment. The left panel shows how any circulating current distribution $\mathbf{J}$ gives rise to a toroidal moment. The right panel highlights that, for bound currents $\mathbf{J} = \mathbf{J}_b$, this toroidal moment naturally splits into a bulk contribution, associated with the magnetization in the volume, and a surface contribution, associated with the surface bound currents.

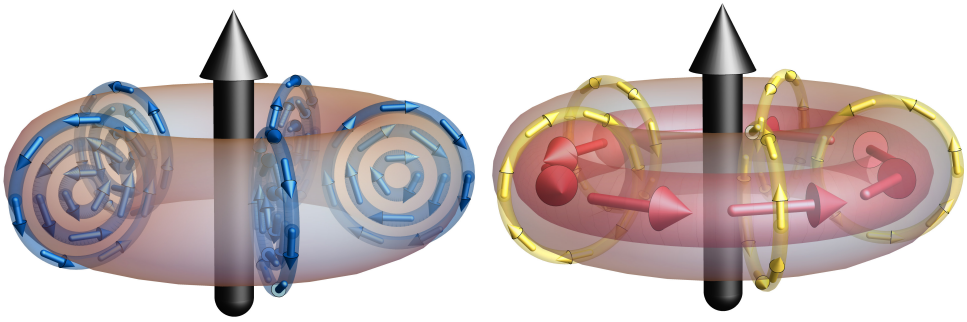

FIGURE 2.13: (Left panel) Toroidal moment (black central arrow) generated by any kind of circulating current distribution $\mathbf{J}$ (blue arrows). (Right panel) For bound currents only ($\mathbf{J} = \mathbf{J}_b$) the toroidal moment has two contributions: a volumetric one, arising from the magnetization in the bulk (red arrows) and a surface contribution, arising from the surface bound currents (yellow arrows).

2.3.4 Choice of origin

The toroidal moment can be used to predict the existence of dipolar symmetry breaking in the magnon spectrum [18]. However, one issue that is not considered in the relation of the toroidal moment with spin dynamics is the proper choice of origin when calculating the volume toroidal moment. One can easily check, e.g., with Eq. (2.28), that shifting the coordinate origin by a vector $\mathbf{R}$ changes the toroidal moment $\boldsymbol{\tau}^v \mapsto \boldsymbol{\tau}^v + (1/2)\, V\, \mathbf{R} \times \langle \mathbf{M} \rangle$, where V is the sample volume. Nonetheless, the choice of origin is not an issue if the sample has a zero magnetic moment, $\langle \mathbf{M} \rangle = 0$, such as the vortex texture [18]. One route to circumvent this origin dependence is found in Ref. [99] for localized spins, where $\mathbf{M}$ is divided into a compensated part with zero magnetic moment $\mathbf{M}^{(0)} = \mathbf{M} - \langle \mathbf{M} \rangle$ and an uncompensated or fully polarized background $\mathbf{M}^{(1)} = \langle \mathbf{M} \rangle$. Following Ref. [99], the part of the toroidal moment due to $\langle \mathbf{M} \rangle$ cannot induce any frequency asymmetry for a homogeneous and centrosymmetric lattice (in the absence of intrinsic DMI). Therefore, the only part of the

toroidal moment that is relevant for dipolar symmetry-breaking is [1]

$$\boldsymbol{\tau}^{\mathrm{v}} = \frac{1}{2}\int \mathbf{r} \times (\mathbf{M} - \langle \mathbf{M} \rangle)\, \mathrm{d}V, \tag{2.31}$$

which is origin-independent, as it involves only the compensated magnetization. This expression proves especially useful, as will be demonstrated in the following sections, for nonsymmetric structures such as partially closed tubes (Subsection 3.2.5), as well as for systems with spatial variation in M_{s}, including graded films (Section 3.3) and multilayers with differing thicknesses and saturation magnetizations. While $\boldsymbol{\tau}$ can be estimated using Eqs. (2.27-2.31), in general, their different definitions are parallel to each other. Then, $\boldsymbol{\tau} \cdot \mathbf{k}$ can be calculated using any of these definitions.

2.4 Magnetic tensor and nonreciprocal magnonics

It was already mentioned in subsection 2.1.2 that the effective magnetic field $\mathbf{H}_{\mathrm{eff}}$ can be obtained through the functional derivative of the total energy of the system. By defining a dimensionless field $\mathbf{h}_i = \mathbf{H}_i / M_{\mathrm{s}}$, it is possible to write this effective field as

$$\mathbf{h}_{\mathrm{eff}} = \mathbf{h}_{\mathrm{ext}} - \tilde{\mathbf{N}} \cdot \mathbf{m}, \tag{2.32}$$

where $\mathbf{h}_{\mathrm{ext}}$ is the unitary external field and $\tilde{\mathbf{N}}$ is the integro-differential operator which includes the sum of all magnetic self-interaction tensors. When $\tilde{\mathbf{N}}$ is projected into the Fourier space and averaged for a particular case, an effective tensor $\mathcal{N}$ is obtained, also referred to as *spin-wave effective tensor*. Formally, the relationship between these quantities can be obtained as follows. Let $\mathbf{r} = (\boldsymbol{\rho}, z)$, where $\boldsymbol{\rho}$ denotes the transverse coordinates on a cylindrical cross section $\Omega_{\perp}$. Cylindrical coordinates are chosen only for simplicity. For a general magnetic system, the internal reduced field is written as,

$$\mathbf{h}_{\mathrm{int}}(\mathbf{r}) = -\big(\tilde{\mathbf{N}} \cdot \mathbf{m}\big)(\mathbf{r}), \tag{2.33}$$

and the effective magnetic tensor is

$$\tilde{\mathbf{N}} = \sum_i \tilde{\mathbf{N}}^{(i)} \quad \text{(exchange, dipolar, anisotropy, ...)}. \tag{2.34}$$

Spin waves are assumed to have spatial mode profiles of the form

$$\mathbf{m}_{\nu}(\mathbf{r}) = \boldsymbol{\eta}_{\nu k}(\boldsymbol{\rho})\, e^{ikz}, \tag{2.35}$$

with a transverse vector profile $\boldsymbol{\eta}_{\nu k}(\boldsymbol{\rho})$ and longitudinal wave number k. Restricting $\tilde{\mathbf{N}}$ to this subspace yield a k-parametrized transverse operator $\mathbf{N}(k)$ defined by

$$\big[\mathbf{N}(k) \cdot \boldsymbol{\eta}\big](\boldsymbol{\rho}) \equiv e^{-ikz}\Big(\tilde{\mathbf{N}} \cdot \big[\boldsymbol{\eta}(\boldsymbol{\rho}) e^{ikz}\big]\Big)(\mathbf{r}). \tag{2.36}$$

[1] From this point forward, $\boldsymbol{\tau}^{\mathrm{v}}$ will refer to Eq. (2.31), a more general formulation compared to Eq. (2.28).

For illustrative purposes, the exchange interaction field is $\mathbf{h}_{\text{ex}} = \ell_{\text{ex}}^2 \nabla^2 \mathbf{m}$ with $\ell_{\text{ex}} = \sqrt{2A/(\mu_0 M_{\text{s}}^2)}$ the exchange length, so that

$$\tilde{\mathbf{N}}^{(\text{ex})} = -\ell_{\text{ex}}^2 \nabla^2. \tag{2.37}$$

For the particular of cylindrical coordinates,

$$\mathbf{N}^{(\text{ex})}(k) = -\ell_{\text{ex}}^2 \left(\nabla_\rho^2 - k^2 \mathbf{I}\right), \tag{2.38}$$

where $\partial_z^2 \to -k^2$ and the transverse Laplacian ∇_ρ^2 acts on $\boldsymbol{\eta}(\boldsymbol{\rho})$. Then, in order to perform the transverse projection onto the mode ν, let's introduce the transverse inner product over the cross section and project the operator equation onto the chosen transverse profile $\boldsymbol{\eta}_{\nu k}$. The resulting *spin-wave effective tensor* for mode ν is

$$\mathcal{N}_\nu(k) = \int_{\Omega_\perp} \boldsymbol{\eta}_{\nu k}^\dagger(\boldsymbol{\rho})\, \mathbf{N}(k)\, \boldsymbol{\eta}_{\nu k}(\boldsymbol{\rho})\, \mathrm{d}S, \tag{2.39}$$

which is a matrix acting on the modal amplitude associated with the spin wave. For a more detailed discussion, please see Refs. [20, 164].

The frequency shift among counterpropagating spin waves $\Delta f = f(\mathbf{k}) - f(-\mathbf{k})$ quantifies the nonreciprocity and analytical formulae for Δf have been obtained only for some magnetic systems such as thin films with Dzyaloshinskii–Moriya interaction [89], ferromagnetic coupled bilayers [24–26], thin films with spin waves propagating under the influence of an electric current [175, 176], and magnetic nanotubes [14–21]. A general expression can be derived from Ref. [89], which reads

$$\Delta f = \frac{\gamma \mu_0 M_{\text{s}}}{\pi} \mathrm{Im}[\mathcal{N}^{(21)}(\mathbf{k})], \tag{2.40}$$

where γ is the absolute value of the gyromagnetic ratio, μ_0 is the vacuum permeability, M_{s} is the saturation magnetization, and $\mathcal{N}^{(21)}(\mathbf{k})$ is the off-diagonal element of the spin-wave tensor in a local basis, which has the property $\mathcal{N}^{(12)} = [\mathcal{N}^{(21)}]^*$ [177]. It must be mentioned that such a formula is not restricted to small k, and may lead to nonlinear wave-vector dependence due to the dipolar coupling [17, 20, 21, 177]. If Δf is expanded up to first order in the wave vector, then it can be shown that $\mathrm{Im}[\mathcal{N}^{(21)}] \propto (\boldsymbol{\tau} \cdot \mathbf{k})$. Namely, the toroidal moment allows for estimating nonreciprocity in the small k-limit [97].

2.5 Multipole expansion

Following Refs. [33, 178], the interaction energy E_{int} of a magnetization distribution $\mathbf{M}(\mathbf{r})$ subjected to an inhomogeneous magnetic field $\mathbf{H}(\mathbf{r})$ that varies slowly on the scale of the system size is given by

$$E_{\text{int}} = -\mu_0 \int \mathbf{M}(\mathbf{r}) \cdot \mathbf{H}(\mathbf{r})\, \mathrm{d}V. \tag{2.41}$$

This can be expanded in powers of field gradients calculated at some arbitrary reference point $\mathbf{r} = \mathbf{r}_0$,

$$\begin{aligned} E_{\text{int}} = &- \mu_0 \int \mathbf{M}(\mathbf{r}) \cdot \mathbf{H}(\mathbf{r}_0)\, \mathrm{d}V - \mu_0 \int r_i M_j(\mathbf{r}) \partial_i H_j(\mathbf{r}_0)\, \mathrm{d}V \\ &- \mu_0 \int M_i(\mathbf{r}) r_j r_k \partial_j \partial_k H_i(\mathbf{r}_0)\, \mathrm{d}V + \ldots, \end{aligned} \tag{2.42}$$

where i, j are cartesian directions (summation over repeated indices is implied). The first term is the interaction of field with the magnetic moment of the system

$$\boldsymbol{m}_{\text{tot}} = \int \mathbf{M}(\mathbf{r})\, \mathrm{d}V. \tag{2.43}$$

In the second term, the tensor $\mathcal{M}_{ij} = \int r_i \mu_j(\mathbf{r})\, \mathrm{d}V$ with nine components can be decomposed into three irreducible tensors:

1. The pseudoscalar from the trace of tensor,

$$a = \frac{1}{3}\mathcal{M}_{ii} = \frac{1}{3}\int \mathbf{r} \cdot \mathbf{M}(\mathbf{r})\, \mathrm{d}V, \tag{2.44}$$

2. The toroidal moment, defined as the axial vector dual to the antisymmetric part of the tensor, $\tau_i = \frac{1}{2}\varepsilon_{ijk}\mathcal{M}_{jk}$.

$$\boldsymbol{\tau} = \frac{1}{2}\int \mathbf{r} \times \mathbf{M}(\mathbf{r})\, \mathrm{d}V, \tag{2.45}$$

   and

3. The traceless symmetric tensor q_{ij} describing the quadrupole magnetic moment of the system,

$$\begin{aligned} q_{ij} &= \frac{1}{2}\left(\mathcal{M}_{ij} + \mathcal{M}_{ji} - \frac{2}{3}\delta_{ij}\mathcal{M}_{kk}\right) \\ &= \frac{1}{2}\int \left(r_i M_j + r_j M_i - \frac{2}{3}\delta_{ij}\, \mathbf{r} \cdot \mathbf{M}(\mathbf{r})\right) \mathrm{d}V. \end{aligned} \tag{2.46}$$

Then, the expansion of the equation (2.42) can be written in the form

$$E_{\text{int}} = -\mu_0 \boldsymbol{m}_{\text{tot}} \cdot \mathbf{H}(\mathbf{r}_0) - \mu_0 a (\nabla \cdot \mathbf{H})_{\mathbf{r}=\mathbf{r}_0} - \mu_0 \boldsymbol{\tau} \cdot [\nabla \times \mathbf{H}]_{\mathbf{r}=\mathbf{r}_0} - \mu_0 q_{ij} (\partial_i H_j + \partial_j H_i)_{\mathbf{r}=\mathbf{r}_0} - \ldots \tag{2.47}$$

The tensor $\mathcal{M}_{ij}$ is also referred as magnetoelectric (ME) multipoles, then a corresponds to the ME monopole and q_{ij} as the ME quadrupole moment. These quantities, together with $\boldsymbol{\tau}$ are key ingredients of the linear ME response, accounting for changes in magnetization (polarization) driven by an applied electric (magnetic) field. The work of S. Bhowal and N. Spaldin [150] relates these quantities to the spin multipolization associated with the electronic band structure in lattices hosting nontrivial spin textures (skyrmions, bimerons, and antiskyrmions), thereby enabling a magnetoelectric classification of such textures.

Chapter 3

Evaluation of the Toroidal Moments in Magnetic Systems

In the previous section, the concepts of toroidal moments, total, volume, and surface contributions, as well as the importance of choosing an appropriate origin, were formally introduced. In this section, these moments will be calculated for different magnetic systems, with specific equilibrium magnetizations and geometries, with the purpose of quantitatively analyzing the toroidal moments.

3.1 Two illustrative examples for continuous magnetization

The following extends the calculation of toroidal moments to nanomagnets with continuous magnetization. To illustrate the approach, two examples are presented in this section: the calculation of both volume and surface toroidal moments for (i) a cuboid with homogeneous magnetization along a single direction, and (ii) a nanodisk exhibiting vortex magnetization.

3.1.1 Rectangular cuboid

Elongated rectangular nanomagnets tend to magnetize along the major axis due to the shape anisotropy induced by the dipolar field, thus exhibiting a practically uniform magnetization as shown in the literature [179], in the absence of external fields or additional anisotropies. Consider a ferromagnetic cuboid with dimensions L_x, L_y, L_z and with uniform magnetization $\mathbf{M} = M_\mathrm{s}\mathbf{m}$, where $\mathbf{m}$. It can be seen that $\nabla \times \mathbf{M} = 0$, so there is no total toroidal moment. On the other hand, and as stated in the subsection 2.3.4, the useful part for calculating the toroidal moment is $\mathbf{M} \mapsto \mathbf{M} - \langle \mathbf{M} \rangle$. The average magnetization field is calculated as $\langle \mathbf{M} \rangle = \frac{1}{V} \int_V M_\mathrm{s}\, \mathbf{m}\, \mathrm{d}V$, and for this case it is $\langle \mathbf{M} \rangle = M_\mathrm{s}\mathbf{m} = \mathbf{M}$. Then, it is easily seen that $\boldsymbol{\tau}^\mathrm{v} = 0$. This would also apply to the surface toroidal moment in the calculation of surface bound currents $\mathbf{K}_\mathrm{b} = (\mathbf{M} - \langle \mathbf{M} \rangle) \times \hat{n}$, in which case it is clear that $\boldsymbol{\tau}^\mathrm{s} = 0$. Despite its simplicity, this result is independent of origin and demonstrates that the toroidal moment for a nanomagnet with uniform magnetization along a single direction and constant M_s is always zero. However, it is possible to arrive at the same result by considering the symmetry of the nanomagnet. In this case, for example, by establishing the reference system at the geometric center of the cuboid. The volume toroidal

moment, calculated with the cuboid's geometric center as the origin, is given by

$$\begin{aligned}\boldsymbol{\tau}^{\mathrm{v}} &= \frac{1}{2}\int_V \mathbf{r}\times\mathbf{M}\,\mathrm{d}V \\ &= \frac{M_{\mathrm{s}}}{2}\int_{-L_z/2}^{L_z/2}\int_{-L_y/2}^{L_y/2}\int_{-L_x/2}^{L_x/2}(x,y,z)\times(m_x,m_y,m_z)\,\mathrm{d}x\,\mathrm{d}y\,\mathrm{d}z \\ &= \frac{M_{\mathrm{s}}}{2}\int_{-L_z/2}^{L_z/2}\int_{-L_y/2}^{L_y/2}\int_{-L_x/2}^{L_x/2}(m_z y - z m_y, m_x z - m_z x, m_y x - m_x y)\,\mathrm{d}x\,\mathrm{d}y\,\mathrm{d}z \\ &= \frac{M_{\mathrm{s}}}{4}(m_z y^2 - m_y z^2, m_x z^2 - m_z x^2, m_y x^2 - m_x y^2)|_{-L_x/2}^{L_x/2}|_{-L_y/2}^{L_y/2}|_{-L_z/2}^{L_z/2} \\ &= 0. \end{aligned} \tag{3.1}$$

Meanwhile for the surface toroidal moment,

$$\boldsymbol{\tau}^{\mathrm{s}} = \frac{1}{10}\oiint_S [\mathbf{r}(\mathbf{r}\cdot\mathbf{K}_{\mathrm{b}}) - 2r^2\mathbf{K}_{\mathrm{b}}]\,\mathrm{d}S. \tag{3.2}$$

For this geometry we have six normal surfaces, namely: $\hat{n}_1 = \hat{x}, \hat{n}_2 = -\hat{x}, \hat{n}_3 = \hat{y}, \hat{n}_4 = -\hat{y}, \hat{n}_5 = \hat{z}$ and $\hat{n}_6 = -\hat{z}$. For simplicity, let's assume $\mathbf{m} = \hat{x}$, however, the following result applies for any direction of uniform and homogeneous magnetization. The associated surface bound currents are

$$\begin{aligned}\mathbf{K}_{\mathrm{b},1} &= \mathbf{M}\times\hat{n}_1 = 0 \\ \mathbf{K}_{\mathrm{b},2} &= \mathbf{M}\times\hat{n}_2 = 0 \\ \mathbf{K}_{\mathrm{b},3} &= \mathbf{M}\times\hat{n}_3 = M_{\mathrm{s}}\hat{z} \\ \mathbf{K}_{\mathrm{b},4} &= \mathbf{M}\times\hat{n}_4 = -M_{\mathrm{s}}\hat{z} \\ \mathbf{K}_{\mathrm{b},5} &= \mathbf{M}\times\hat{n}_5 = -M_{\mathrm{s}}\hat{y} \\ \mathbf{K}_{\mathrm{b},6} &= \mathbf{M}\times\hat{n}_6 = M_{\mathrm{s}}\hat{y} \end{aligned} \tag{3.3}$$

By integrating over the respective surfaces,

$$\boldsymbol{\tau}_1^{\mathrm{s}} = \boldsymbol{\tau}_2^{\mathrm{s}} = 0, \tag{3.4}$$

$$\begin{aligned}\boldsymbol{\tau}_3^{\mathrm{s}} &= \frac{M_{\mathrm{s}}}{10}\int_{-L_x/2}^{L_x/2}\int_{-L_z/2}^{L_z/2}\left[\left(x\hat{x}+\frac{L_y}{2}\hat{y}+z\hat{z}\right)(z) - 2\left(x^2+\frac{L_y^2}{4}+z^2\right)\hat{z}\right]\mathrm{d}x\,\mathrm{d}z \\ &= -M_{\mathrm{s}}\frac{L_x L_z}{120}\left(2L_x^2+6L_y^2+L_z^2\right)\hat{z} \end{aligned} \tag{3.5}$$

$$\begin{aligned}\boldsymbol{\tau}_4^{\mathrm{s}} &= \frac{M_{\mathrm{s}}}{10}\int_{-L_x/2}^{L_x/2}\int_{-L_z/2}^{L_z/2}\left[\left(x\hat{x}-\frac{L_y}{2}\hat{y}+z\hat{z}\right)(-z) + 2\left(x^2+\frac{L_y^2}{4}+z^2\right)\hat{z}\right]\mathrm{d}x\,\mathrm{d}z \\ &= M_{\mathrm{s}}\frac{L_x L_z}{120}\left(2L_x^2+6L_y^2+L_z^2\right)\hat{z} \end{aligned} \tag{3.6}$$

$$\begin{aligned}\boldsymbol{\tau}_5^{\mathrm{s}} &= \frac{M_{\mathrm{s}}}{10}\int_{-L_x/2}^{L_x/2}\int_{-L_y/2}^{L_y/2}\left[\left(x\hat{x}+y\hat{y}+\frac{L_z}{2}\hat{z}\right)(-y) + 2\left(x^2+y^2+\frac{L_z^2}{4}\right)\hat{y}\right]\mathrm{d}x\,\mathrm{d}y \\ &= M_{\mathrm{s}}\frac{L_x L_y}{120}\left(2L_x^2+L_y^2+6L_z^2\right)\hat{y} \end{aligned} \tag{3.7}$$

$$\begin{aligned}\boldsymbol{\tau}_6^{\mathrm{s}} &= \frac{M_{\mathrm{s}}}{10}\int_{-L_x/2}^{L_x/2}\int_{-L_y/2}^{L_y/2}\left[\left(x\hat{x}+y\hat{y}-\frac{L_z}{2}\hat{z}\right)(y)-2\left(x^2+y^2+\frac{L_z^2}{4}\right)\hat{y}\right]\mathrm{d}x\,\mathrm{d}y \\ &= -M_{\mathrm{s}}\frac{L_xL_y}{120}\left(2L_x^2+L_y^2+6L_z^2\right)\hat{y} \end{aligned} \tag{3.8}$$

Adding up all contributions,

$$\boldsymbol{\tau}^{\mathrm{s}} = 0 \tag{3.9}$$

The results for the total, volume, and surface toroidal moments demonstrate that homogeneous magnetization in symmetrically confined systems does not produce any toroidal moment. Furthermore, they confirm that it remains unchanged after subtracting the average magnetization, for a spatially uniform M_{s} and symmetric geometry.

3.1.2 Nanoring in vortex state

As mentioned above in subsection 2.1.3, circular structures such as disks or rings with a radius of a few tens of nanometers prefer a circulating magnetization due to dipolar interactions. The simplest model is the coreless vortex state given by $\mathbf{M}_{\mathrm{vortex}} = M_{\mathrm{s}}\hat{\boldsymbol{\phi}}$, in cylindrical coordinates and considering a ring with inner radius R_{i}, outer radius R, and thickness d. Firstly, it can be noted that this magnetization has a direction of rotation that intuitively generates bound currents, as will be shown later, with interesting consequences. Secondly, its average magnetization is zero, because $\int_0^{2\pi}\hat{\boldsymbol{\phi}}\,\mathrm{d}\phi = 0$. This means that for our purposes, the relevant part of the toroidal moment is independent of the origin, and the simplest way to calculate it is to consider the origin of the reference system at the geometric center of the ring. By using that $\mathbf{r} = \rho\hat{\boldsymbol{\rho}} + z\hat{z}$, the volume toroidal moment is

$$\begin{aligned}\boldsymbol{\tau}^{\mathrm{v}} &= \frac{1}{2}\int_V(\mathbf{r}\times\mathbf{M})\,\mathrm{d}V \\ &= \frac{M_{\mathrm{s}}}{2}\int_V(\rho\hat{\boldsymbol{\rho}}+z\hat{z})\times\hat{\boldsymbol{\phi}}\,\rho\,\mathrm{d}\rho\,\mathrm{d}\phi\,\mathrm{d}z \\ &= \frac{M_{\mathrm{s}}}{2}\int_{-d/2}^{d/2}\int_0^{2\pi}\int_{R_{\mathrm{i}}}^{R}(-z\hat{\boldsymbol{\rho}}+\rho\hat{z})\,\rho\,\mathrm{d}\rho\,\mathrm{d}\phi\,\mathrm{d}z \\ &= \frac{M_{\mathrm{s}}}{2}\left[-\frac{\rho^2}{2}\frac{z^2}{2}\hat{\boldsymbol{\rho}}+\frac{\rho^3}{3}z\hat{z}\right]\Big|_{-d/2}^{d/2}\Big|_{R_{\mathrm{i}}}^{R}\Big|_0^{2\pi} \\ &= M_{\mathrm{s}}\frac{\pi d}{3}(R^3-R_{\mathrm{i}}^3)\hat{z}. \end{aligned} \tag{3.10}$$

Therefore, a nanoring magnetized azimuthally in a counterclockwise direction produces a toroidal moment parallel to the z-axis.

To evaluate the surface toroidal moment, the surfaces must be first defined: Their normal vectors are $\hat{n}_1 = \hat{\boldsymbol{\rho}}$ at $\rho = R$, $\hat{n}_2 = -\hat{\boldsymbol{\rho}}$ at $\rho = R_{\mathrm{i}}$, and the two caps $\hat{n}_{3,4} = \pm\hat{z}$ at $z = \pm d/2$. The associated surface bound-currents are,

$$\begin{aligned}\mathbf{K}_{\mathrm{b},1} &= \mathbf{M}\times\hat{n}_1 = -M_{\mathrm{s}}\,\hat{z}, \\ \mathbf{K}_{\mathrm{b},2} &= \mathbf{M}\times\hat{n}_2 = M_{\mathrm{s}}\,\hat{z}, \\ \mathbf{K}_{\mathrm{b},3} &= \mathbf{M}\times\hat{n}_3 = M_{\mathrm{s}}\,\hat{\boldsymbol{\rho}}, \\ \mathbf{K}_{\mathrm{b},4} &= \mathbf{M}\times\hat{n}_4 = -M_{\mathrm{s}}\hat{\boldsymbol{\rho}}, \end{aligned} \tag{3.11}$$

Integrating on the respective surfaces,

$$\begin{aligned}\boldsymbol{\tau}_1^{\mathrm{s}} &= -\frac{1}{10}\int_{S_1}\left[\mathbf{r}(\mathbf{r}\cdot\mathbf{K}_{\mathrm{b},1}) - 2r^2\mathbf{K}_{\mathrm{b},1}\right]\mathrm{d}S_1 \\ &= -\frac{1}{10}\int_{S_1}\left[(R\hat{\rho}+z\hat{z})(-M_{\mathrm{s}}z) + 2M_{\mathrm{s}}(R^2+z^2)\hat{z}\right]R\mathrm{d}\phi\mathrm{d}z \\ &= -\frac{1}{5}M_{\mathrm{s}}\pi R\left(\frac{d^3}{12}+2dR^2\right)\hat{z}, \end{aligned} \tag{3.12}$$

$$\begin{aligned}\boldsymbol{\tau}_2^{\mathrm{s}} &= \frac{1}{10}\int_{S_2}\left[\mathbf{r}(\mathbf{r}\cdot\mathbf{K}_{\mathrm{b},2}) - 2r^2\mathbf{K}_{\mathrm{b},2}\right]\mathrm{d}S_2 \\ &= \frac{1}{10}\int_{S_2}\left[(R_{\mathrm{i}}\hat{\rho}+z\hat{z})(-M_{\mathrm{s}}z) + 2M_{\mathrm{s}}(R_{\mathrm{i}}^2+z^2)\hat{z}\right]R_{\mathrm{i}}\mathrm{d}\phi\mathrm{d}z \\ &= \frac{1}{5}M_{\mathrm{s}}\pi R_{\mathrm{i}}\left(\frac{d^3}{12}+2dR_{\mathrm{i}}^2\right)\hat{z}, \end{aligned} \tag{3.13}$$

$$\begin{aligned}\boldsymbol{\tau}_3^{\mathrm{s}} &= -\frac{1}{10}\int_{S_3}\left[\mathbf{r}(\mathbf{r}\cdot\mathbf{K}_{\mathrm{b},3}) - 2r^2\mathbf{K}_{\mathrm{b},3}\right]\mathrm{d}S_3 \\ &= -\frac{1}{10}\int_{S_3}\left[(\rho\hat{\rho}+(d/2)\hat{z})(M_{\mathrm{s}}\rho) - 2M_{\mathrm{s}}(\rho^2+(d/2)^2)\hat{\rho}\right]\rho\mathrm{d}\rho\mathrm{d}\phi \\ &= -\frac{M_{\mathrm{s}}}{10}(d/2)\int_{S_3}\rho^2\mathrm{d}\rho\mathrm{d}\phi\hat{z} \\ &= -\frac{M_{\mathrm{s}}}{30}\pi d(R^3-R_{\mathrm{i}}^3)\hat{z}, \end{aligned} \tag{3.14}$$

$$\begin{aligned}\boldsymbol{\tau}_4^{\mathrm{s}} &= -\frac{1}{10}\int_{S_4}\left[\mathbf{r}(\mathbf{r}\cdot\mathbf{K}_{\mathrm{b},4}) - 2r^2\mathbf{K}_{\mathrm{b},4}\right]\mathrm{d}S_4 \\ &= -\frac{1}{10}\int_{S_4}\left[(\rho\hat{\rho}+(-d/2)\hat{z})(-M_{\mathrm{s}}\rho) + 2M_{\mathrm{s}}(\rho^2+(d/2)^2)\hat{\rho}\right]\rho\mathrm{d}\rho\mathrm{d}\phi \\ &= -\frac{M_{\mathrm{s}}}{10}(d/2)\int_{S_4}\rho^2\mathrm{d}\rho\mathrm{d}\phi\hat{z} \\ &= -\frac{M_{\mathrm{s}}}{30}\pi d(R^3-R_{\mathrm{i}}^3)\hat{z}. \end{aligned} \tag{3.15}$$

Then, the surface toroidal moment is,

$$\boldsymbol{\tau}^{\mathrm{s}} = -\frac{M_{\mathrm{s}}\pi d}{60}\left[28(R^3-R_{\mathrm{i}}^3)+d^2(R-R_{\mathrm{i}})\right]\hat{z}. \tag{3.16}$$

Comparing the two toroidal moments, volume Eq. 3.10 and surface Eq. 3.16, it can be seen that both are parallel to the z-axis. However, there is a difference in magnitude, which is explained by the total toroidal moment (Eq. 2.27), by using the

bound currents $\mathbf{J}_\mathrm{b}$. For this configuration, the bound current is given by

$$\begin{aligned}\mathbf{J}_\mathrm{b} &= \nabla \times \mathbf{M} \\ &= M_\mathrm{s} \nabla \times \hat{\phi} \\ &= \frac{M_\mathrm{s}}{\rho} \hat{z}.\end{aligned} \tag{3.17}$$

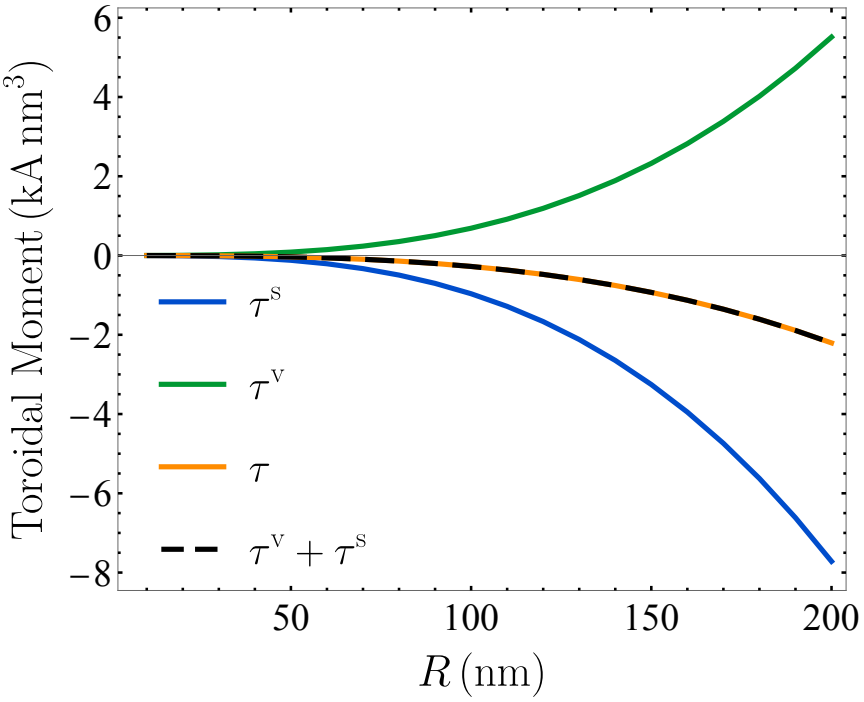

FIGURE 3.1: Toroidal moment (z-component) versus radius for a vortex magnetization in a 1 nm-thick nanoring with $R_\mathrm{i} = 5\,\mathrm{nm}$ and $M_\mathrm{s} = 658\,\mathrm{kA/m}$. The blue (green) line is the volume (surface) toroidal moment of volume. The toroidal moment, calculated directly from bound volume currents, is shown in orange, and the sum of the volume and surface toroidal moments is shown in black dashed.

With this the toroidal moment is,

$$\begin{aligned}\boldsymbol{\tau} &= \frac{1}{10} \int \left[\mathbf{r} \left(\mathbf{r} \cdot \frac{M_\mathrm{s}}{\rho} \hat{z} \right) - 2r^2 \frac{M_\mathrm{s}}{\rho} \hat{z} \right] \mathrm{d}V \\ &= \frac{M_\mathrm{s}}{10} \int \left[\mathbf{r} \left(\frac{z}{\rho} \right) - \frac{2r^2}{\rho} \hat{z} \right] \mathrm{d}V \\ &= \frac{M_\mathrm{s}}{10} \int_{R_\mathrm{i}}^{R} \int_0^{2\pi} \int_{-d/2}^{d/2} \left[(\rho\hat{\rho} + z\hat{z}) \left(\frac{z}{\rho} \right) - \frac{2(\rho^2 + z^2)}{\rho} \hat{z} \right] \rho \mathrm{d}\rho \mathrm{d}\phi \mathrm{d}z \\ &= -M_\mathrm{s} \frac{\pi}{5} \int_{R_\mathrm{i}}^{R} \int_{-d/2}^{d/2} \left(z^2 + 2\rho^2 \right) \hat{z} \, \mathrm{d}\rho \mathrm{d}z \\ &= -M_\mathrm{s} \frac{\pi d}{60} \left[d^2 (R - R_\mathrm{i}) + 8(R^3 - R_\mathrm{i}^3) \right] \hat{z}.\end{aligned} \tag{3.18}$$

It can be seen that if the contributions of volume and surface area are added together, the result is

$$\begin{aligned}\boldsymbol{\tau}^{\mathrm{v}}+\boldsymbol{\tau}^{\mathrm{s}} &= M_{\mathrm{s}}\frac{\pi d}{3}(R^3-R_{\mathrm{i}}^3)\hat{z}-M_{\mathrm{s}}\frac{\pi d}{60}\left[28(R^3-R_{\mathrm{i}}^3)+d^2(R-R_{\mathrm{i}})\right]\hat{z}\\ &= -M_{\mathrm{s}}\frac{\pi d}{60}\left[d^2(R-R_{\mathrm{i}})+8(R^3-R_{\mathrm{i}}^3)\right]\hat{z},\end{aligned} \tag{3.19}$$

which is exactly the result for $\boldsymbol{\tau}$. In order to quantitatively compare these different toroidal moments, Fig. 3.1 illustrates how the $z-$component value changes as a function of the outer radius for M_{s} = 658 kA/m, d =1 nm, and R_{i} = 5 nm, where the three toroidal moments as well as the sum of the volume and surface toroidal moments are illustrated. From this, it can be clearly seen that the surface toroidal moment is comparable in magnitude to the volume toroidal moment, but that they differ in sign. It can even be seen that the surface toroidal moment is greater in magnitude. Finally, it is evident that the sum of both is equal to the total toroidal moment, i.e, $\boldsymbol{\tau}=\boldsymbol{\tau}^{\mathrm{v}}+\boldsymbol{\tau}^{\mathrm{s}}$.

3.2 Magnetic Texture Systems

Below is the calculation of toroidal moments for less trivial magnetic textures, such as conical-helical and skyrmionic textures in flat and tubular systems.

3.2.1 Thin Films with Dzyaloshinskii–Moriya Interaction

In ultra-thin magnetic films, conical-helical (CH) textures may emerge due to the competition between the Dzyaloshinskii–Moriya interaction, symmetric exchange, perpendicular anisotropy, dipolar field, and a bias field [61]. We can consider an ultrathin film of side length L and thickness d, where a bias in-plane field $\mathbf{H}=H\hat{y}$ is applied and a perpendicular anisotropy (out-of-plane) is present. Here x, y are the in-plane directions, and z is the perpendicular. The magnetization can be modeled as already shown in Subsection 2.1.3. Although the model can provide valuable information about the conical helix, it is limited in some aspects. First, it does not account for spatial variations of the magnetization near the boundaries. Second, the helical cone is perfectly circular, which may not appear realistic since, in thin films, anisotropy may change the usual bulk form of the CH texture, inducing an elliptical deformation of the cone when the quality factor Q, which relates the anisotropy with the magnetostatic interaction, deviates from one [124]. Such noncircular CH is expected in thin films when perpendicular anisotropy dominates over the demagnetizing field or vice versa. Third, the magnetization can cease to be characterized by a continuous model, presenting abrupt changes in orientation due to high values of anisotropy for $Q\gg 1$, enabling alternating out-of-plane magnetization patterns.

For this model and geometry, the surface and volume toroidal moments have been calculated with respect to the geometric center of an ultrathin film, which results in

$$\boldsymbol{\tau}^{\mathrm{s}}=\sin\theta\begin{pmatrix}\mathcal{A}_1^{\mathrm{s}}\sin\psi\cos\varphi_{\mathbf{q}}\\ -\mathcal{A}_1^{\mathrm{s}}\sin\psi\sin\varphi_{\mathbf{q}}\\ \mathcal{A}_2^{\mathrm{s}}\cos\psi\cos\varphi_{\mathbf{q}}\end{pmatrix} \tag{3.20}$$

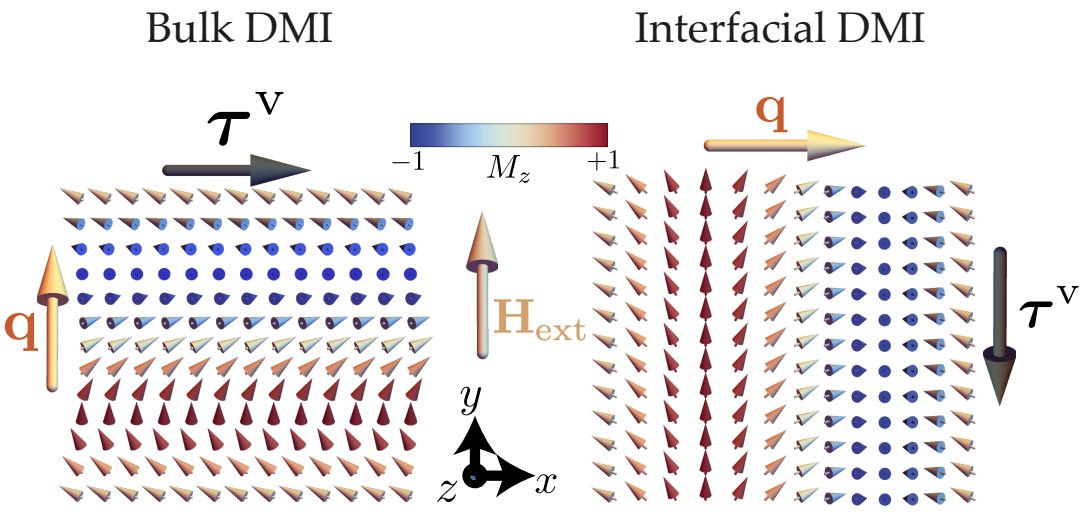

FIGURE 3.2: Conical-helix textures in a thin film with bulk (left) and interfacial (right) DM interaction, where the applied field $\mathbf{H}_{\mathrm{ext}}$ is along y such that the cone-angle is $\theta_0 = \pi/3$ and the phase is $\psi = \pi/2$. The in-plane helical pitch vector $\mathbf{q}$ is parallel (perpendicular) to the field for bulk (interfacial) DMI. The resulting volume toroidal moment (black arrow) is illustrated in both cases and is always in the plane and perpendicular to the pitch vector.

and

$$\boldsymbol{\tau}^{\mathrm{v}} = \mathcal{B}^{\mathrm{v}} \sin\theta \begin{pmatrix} \sin\psi\cos\varphi_{\mathbf{q}} \\ -\sin\psi\sin\varphi_{\mathbf{q}} \\ \cos\psi\cos\varphi_{\mathbf{q}} \end{pmatrix}, \tag{3.21}$$

where $\mathcal{A}_1^{\mathrm{s}}, \mathcal{A}_2^{\mathrm{s}}$ and $\mathcal{B}^{\mathrm{v}}$ depend on M_{s}, L, d and q and are given by,

$$\mathcal{A}_1^{\mathrm{s}} = \frac{M_{\mathrm{s}} dL}{60q^2}\left[(2d^2q^2 + 7L^2q^2 + 12)\sin\left(\frac{Lq}{2}\right) - 6Lq\cos\left(\frac{Lq}{2}\right)\right], \tag{3.22}$$

$$\mathcal{A}_2^{\mathrm{s}} = \frac{M_{\mathrm{s}} dL}{60q^2}\left[(d^2q^2 + 8L^2q^2 + 12)\sin\left(\frac{Lq}{2}\right) - 6Lq\cos\left(\frac{Lq}{2}\right)\right], \tag{3.23}$$

$$\mathcal{B}^{\mathrm{v}} = \frac{M_{\mathrm{s}} dL}{2q^2}\left[Lq\cos\left(\frac{Lq}{2}\right) - 2\sin\left(\frac{Lq}{2}\right)\right]. \tag{3.24}$$

Fig. 3.2 shows the conical textures in a squared film, for (a) b-DMI and (b) i-DMI, with the respective volume toroidal moments for a fixed phase, when the external field is applied along $y-$direction for both systems. From the toroidal moment calculations, an oscillatory behavior around $Lq/2$ is a prominent feature, which may result in positive, zero, or negative toroidal moments. In the ultrathin limit $L \gg d$, all the terms proportional to $(qd)^2$ are negligible. When comparing $\boldsymbol{\tau}^{\mathrm{v}}$ with $\boldsymbol{\tau}^{\mathrm{s}}$ it is interesting to note that despite their differences, the resulting toroidal moments are parallel to each other and always perpendicular to the respective pitch vector ($\mathbf{q}$) despite the choice of origin. Table 3.1 summarizes the toroidal moment directions for this texture and for both interfacial and bulk Dzyaloshinskii–Moriya interactions (b-DMI and i-DMI).

TABLE 3.1: Toroidal moments for different helical states and DMI types.

Conical-helix	**b-DMI**	**i-DMI**
ψ	$(\varphi_{\mathbf{q}} = 0, \mathbf{q} = q\,\hat{y})$	$(\varphi_{\mathbf{q}} = \pi/2, \mathbf{q} = q\,\hat{x})$
$\pi/2$	$(\tau_x^{\mathrm{s}}, 0, 0) \mid \{S_x, S_y\}$	$(0, \tau_y^{\mathrm{s}}, 0) \mid \{S_x, S_y\}$
0	$(0, 0, \tau_z^{\mathrm{s}}) \mid \{S_y, S_z\}$	0

TABLE 3.2: Summary of the surface toroidal moment directions for the conical helix with bulk and interfacial DMI and for the two relevant phase constants appropriate to in-plane ($\psi = \pi/2$) and out-of-plane ($\psi = 0$) magnetic films. The brackets show the pairs of surfaces contributing to $\boldsymbol{\tau}^{\mathrm{s}}$.

Fig. 3.3 shows the behavior of the nonzero components of $\boldsymbol{\tau}$, $\boldsymbol{\tau}^{\mathrm{v}}$, and $\boldsymbol{\tau}^{\mathrm{s}}$ as functions of the lateral size L for bulk and interfacial DMI, at fixed DMI strength and for $\psi = \pi/2$. The calculations were performed using standard parameters for Permalloy ($Ni_{80}Fe_{20}$) [124]. These curves show that the contribution of $\boldsymbol{\tau}^{\mathrm{s}}$ to the total toroidal moment is always larger than the volume contribution $\boldsymbol{\tau}^{\mathrm{v}}$. This difference in magnitude is not related to the length scale of the system, as illustrated in the inset of Fig. 3.3. Moreover, $\boldsymbol{\tau}^{\mathrm{v}}$ and $\boldsymbol{\tau}^{\mathrm{s}}$ oscillate out of phase as functions of L. This phase difference is particularly relevant because of its physical implications for a hypothetical measurement of the toroidal moment, which could shed light on the importance of the surface contribution. For CH textures with a nonzero toroidal moment, the magnitude of $\boldsymbol{\tau}$ exhibits an oscillatory dependence on the DMI strength, since $q \propto D$. A key difference between b-DMI ($\varphi_{\mathbf{q}} = 0$) and i-DMI ($\varphi_{\mathbf{q}} = \pi/2$) is the sign and direction of $\boldsymbol{\tau}$ for $\psi = \pi/2$. In contrast, for $\psi = 0$ a nonzero $\boldsymbol{\tau}$ is obtained only for b-DMI, while for i-DMI it vanishes. By analyzing the surface contribution, it is observed that for b-DMI there is a slight difference in the amplitudes when comparing $\psi = 0$ and $\psi = \pi/2$, which is not the case for $\boldsymbol{\tau}^{\mathrm{v}}$. Although there is only one configuration in which $\boldsymbol{\tau}$ is identically zero (i-DMI and $\psi = 0$), for all other combinations of $\varphi_{\mathbf{q}}$ and ψ, the toroidal moment can vanish at specific values of $Lq/2$ due to commensurability effects. For the configurations studied, $\boldsymbol{\tau}^{\mathrm{v}}$ and $\boldsymbol{\tau}^{\mathrm{s}}$ are always parallel to either x, y, or z, depending on the type of DMI ($\varphi_{\mathbf{q}}$) and the phase ψ.

In order to describe the surface toroidal moment ($\boldsymbol{\tau}^{\mathrm{s}}$), it is necessary to identify which faces contribute to its formation. Given the cuboid geometry of the sample, the surfaces are grouped by the direction of its normal vector, where S_x, S_y, and S_z refer to each pair of surfaces. Table 3.1 indicates the faces contributing to $\boldsymbol{\tau}^{\mathrm{s}}$ in curly brackets. It is found, surprisingly, that for low perpendicular anisotropy ($\psi = \pi/2$), the surfaces contributing to $\boldsymbol{\tau}^{\mathrm{s}}$ are the lateral edges (S_x, S_y) with area Ld. In contrast, for the surviving $\boldsymbol{\tau}$ when $\psi = 0$, the contributing pair of surfaces are S_y and S_z, where S_z have an area L^2 much larger than for $S_{x,y}$. From the point of view of the amplitudes, no significant difference is predicted when comparing $\psi = 0$ and $\psi = \pi/2$ for b-DMI as mentioned above; it is inferred then that the size of the areas is not particularly relevant, but rather the direction of their normal vectors.

We can also consider a more general form of the magnetization, for arbitrary $\varphi_{\mathbf{q}}$. This kind of textures can emerge on the recently studied materials with C_n symmetry [121], which is described by two DMI strength constants. For such a case the volume

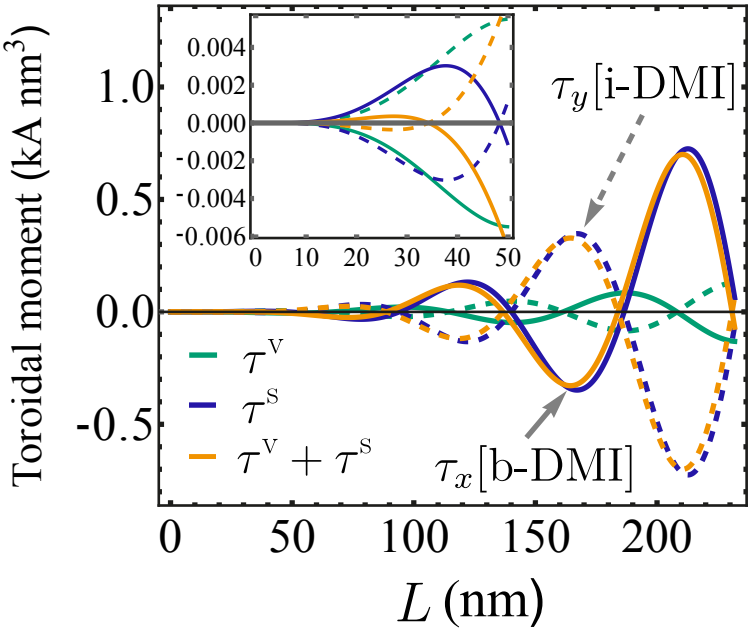

FIGURE 3.3: Nonzero components of the total toroidal moment and its volume and surface contributions as functions of the lateral size L for CH textures with bulk DMI (solid lines) and interfacial DMI (dashed lines), at fixed DMI strength and for $\psi = \pi/2$. Calculations were performed using standard parameters for Permalloy ($Ni_{80}Fe_{20}$) [124]. The inset zooms into the behavior for $L \leq 50$ nm.

toroidal moment is given by,

$$\tau_x^{\mathrm{v}} = \frac{d}{q^3} \csc\varphi \sec\varphi \sin\theta \sin\psi \sin\left(\frac{Lq_x}{2}\right) \left[Lq\cos\left(\frac{Lq_y}{2}\right) - 2\sec\varphi \sin\left(\frac{Lq_y}{2}\right)\right], \tag{3.25}$$

$$\tau_y^{\mathrm{v}} = -\frac{d}{q^3} \csc\varphi \sec\varphi \sin\theta \sin\psi \sin\left(\frac{Lq_y}{2}\right) \left[Lq\cos\left(\frac{Lq_y}{2}\right) - 2\csc\varphi \sin\left(\frac{Lq_x}{2}\right)\right], \tag{3.26}$$

and

$$\tau_z^{\mathrm{v}} = \frac{d}{q^3} \csc\varphi \sec\varphi \sin\theta \cos\psi \sin\left(\frac{Lq_x}{2}\right) \left[Lq\cos\left(\frac{Lq_y}{2}\right) - 2\sec\varphi \sin\left(\frac{Lq_y}{2}\right)\right], \tag{3.27}$$

where $q_x = q\sin\varphi_{\mathbf{q}}$ and $q_y = q\cos\varphi_{\mathbf{q}}$. By carefully taking the limits for $\varphi_{\mathbf{q}} = 0, \pi/2$, the above results can be recovered for i-DMI and b-DMI. Focusing on the intermediate case, $\varphi_{\mathbf{q}} = \pi/4$, i.e., that the pitch vector points in the xy plane, it is observed that the toroidal moment points in a perpendicular direction also in the xy plane for $\psi = \pi/2$. Whereas for $\psi = 0$, the toroidal moment points out of the plane always, even for any value of $\varphi_{\mathbf{q}}$. The surface toroidal moment is presented in Appendix A, where the differences from the volume term are consistent with the explanation above, and the directions of both toroidal moments remain the same.

3.2.2 Arbitrary periodic magnetization in thin films

The previous discussion focuses on a specific periodic magnetic texture. Nevertheless, the analysis of the toroidal moment also applies to an arbitrary periodic texture. In this case, the magnetization can be expanded using a Fourier series in terms of reciprocal vectors **G**, which can have important applications in the study of multi-**G** spin textures, such as skyrmion lattices [139], multiple-q spin textures [180–182], tetrahedral-q hedgehog and cubic-3-q hedgehog lattices.

In order to obtain a general expression for the volume toroidal moment for an arbitrary periodic magnetization in a two-dimensional film, we can consider that the unitary magnetization **m** can be expanded in Fourier terms,

$$\mathbf{m}(\mathbf{r}) = \sum_{\mathbf{G}} \mathbf{m}_{\mathbf{G}} \exp\left(i\,\mathbf{G}\cdot\mathbf{r}\right), \tag{3.28}$$

where $\mathbf{m}_{\mathbf{G}}$ are the Fourier coefficients and **G** are the reciprocal periodicity vectors. The volume toroidal moment, disregarding the correction with $\langle\mathbf{M}\rangle$ due to the symmetry of the film and the fact that there is no variable M_s, is

$$\boldsymbol{\tau}^{\mathrm{v}} = \frac{1}{2}\int \mathbf{r}\times\mathbf{M}\,\mathrm{d}V = \frac{M_s}{2}\int \mathbf{r}\times\mathbf{m}\,\mathrm{d}V. \tag{3.29}$$

Then, the toroidal moment for the periodic magnetization,

$$\boldsymbol{\tau}^{\mathrm{v}} = \frac{M_s}{2}\int \mathbf{r}\times\mathbf{m}\,\mathrm{d}V, \tag{3.30}$$

$$= \frac{M_s}{2}\int \mathbf{r}\times\left[\sum_{\mathbf{G}}\mathbf{m}_{\mathbf{G}}\exp\left(i\,\mathbf{G}\cdot\mathbf{r}\right)\right]\mathrm{d}V. \tag{3.31}$$

The sum and $\mathbf{m}_{\mathbf{G}}$ do not depend on the geometry and we will consider a rectangular coordinated system with $\mathbf{r} = x_j\hat{x}_j$ where $x_j = x, y, z$. On the other hand we will impose the periodicity along the $x-$ and $y-$ directions (in-plane) so $\mathbf{G} = G_x\hat{x} + G_y\hat{y}$. With all of this we can write,

$$\boldsymbol{\tau}^{\mathrm{v}} = \frac{M_s}{2}\sum_{\mathbf{G}}\hat{x}_j\times\mathbf{m}_{\mathbf{G}}\int x_j\exp\left[i(G_x x + G_y y)\right]\mathrm{d}V. \tag{3.32}$$

Expanding explicitly in j

$$\boldsymbol{\tau}^{\mathrm{v}} = \frac{M_s}{2}\sum_{\mathbf{G}}\Bigg[\hat{x}\times\mathbf{m}_{\mathbf{G}}\int x\exp\left[i(G_x x + G_y y)\right]\mathrm{d}x\,\mathrm{d}y\,\mathrm{d}z \tag{3.33}$$

$$+\hat{y}\times\mathbf{m}_{\mathbf{G}}\int y\exp\left[i(G_x x + G_y y)\right]\mathrm{d}x\,\mathrm{d}y\,\mathrm{d}z \tag{3.34}$$

$$+\hat{z}\times\mathbf{m}_{\mathbf{G}}\int z\exp\left[i(G_x x + G_y y)\right]\mathrm{d}x\,\mathrm{d}y\,\mathrm{d}z\Bigg]. \tag{3.35}$$

In order to integrate this we will consider a symmetric rectangular system with dimensions L_x, L_y, L_z. From this it is easy to see that $\int_{-L_z/2}^{L_z/2} z\,\mathrm{d}z = (1/2)z^2\big|_{-L_z/2}^{L_z/2} = 0$

then, we can write that,

$$\boldsymbol{\tau}^{\mathrm{v}} = \frac{M_{\mathrm{s}} L_z}{2} \sum_{\mathbf{G}} \Bigg[\hat{x} \times \mathbf{m}_{\mathbf{G}} \int x \exp\left(iG_x x\right) \mathrm{d}x \int \exp\left(iG_y y\right) \mathrm{d}y \tag{3.36}$$

$$+ \hat{y} \times \mathbf{m}_{\mathbf{G}} \int \exp\left(iG_x x\right) \mathrm{d}x \int y \exp\left(iG_y y\right) \mathrm{d}y \Bigg], \tag{3.37}$$

where the integral over z dropped out the term L_z. The integrals correspond to

$$\begin{aligned} L_j F_1(G_j, L_j) &\equiv \int_{-L_j/2}^{L_j/2} \exp\left(iG_j x_j\right) \mathrm{d}x_j \\ &= \frac{2}{G_j} \sin\left(\frac{G_j L_j}{2}\right), \end{aligned} \tag{3.38}$$

and,

$$\begin{aligned} F_2(G_j, L_j) &\equiv \int_{-L_j/2}^{L_j/2} x_j \exp\left(iG_j x_j\right) \mathrm{d}x_j \\ &= -\frac{i}{G_j^2} \left[G_j L_j \cos\left(\frac{G_j L_j}{2}\right) - 2 \sin\left(\frac{G_j L_j}{2}\right) \right]. \end{aligned} \tag{3.39}$$

Note that,

$$\lim_{G_j \to 0} F_1(G_j, L_j) = 1, \tag{3.40}$$

and

$$\lim_{G_j \to 0} F_2(G_j, L_j) = 0. \tag{3.41}$$

Replacing we get that,

$$\begin{aligned} \boldsymbol{\tau}^{\mathrm{v}} &= \frac{M_{\mathrm{s}} L_z}{2} \sum_{\mathbf{G}} \Big[L_y F_1(G_y, L_y) F_2(G_x, L_x) \hat{x} + L_x F_1(G_x, L_x) F_2(G_y, L_y) \hat{y} \Big] \times \mathbf{m}_{\mathbf{G}} \\ &\equiv \sum_{\mathbf{G}} \boldsymbol{\tau}^{\mathrm{v}}_{\mathbf{G}}. \end{aligned} \tag{3.42}$$

For the particular case $\mathbf{G} = G_x \hat{x}$, that is, there are only periodicities along x, only the first term inside the parentheses survives, and the resulting toroidal moment lies in the y–z plane, perpendicular to the periodicity. Conversely, if $\mathbf{G} = G_y \hat{y}$, the toroidal moment lies in the z–x plane. This confirms that it is the direction of the periodicities that defines the plane in which the toroidal moments will be found. Additional parameters, such as phases, can also define more specific directions. However, in consideration of the above, it can be seen that this result can be summarized in much simpler terms, i.e, the toroidal moment will always be parallel to the vector product between the magnetization pitch vectors $\mathbf{G}$ and the associated magnetization to the periodicity $\mathbf{m}_{\mathbf{G}}$,

$$\boldsymbol{\tau}^{\mathrm{v}}_{\mathbf{G}} \propto \mathbf{G} \times \mathbf{m}_{\mathbf{G}}. \tag{3.43}$$

The following section will show a particular example of this with sinusoidal textures.

3.2.3 Spin textures in confined in disks

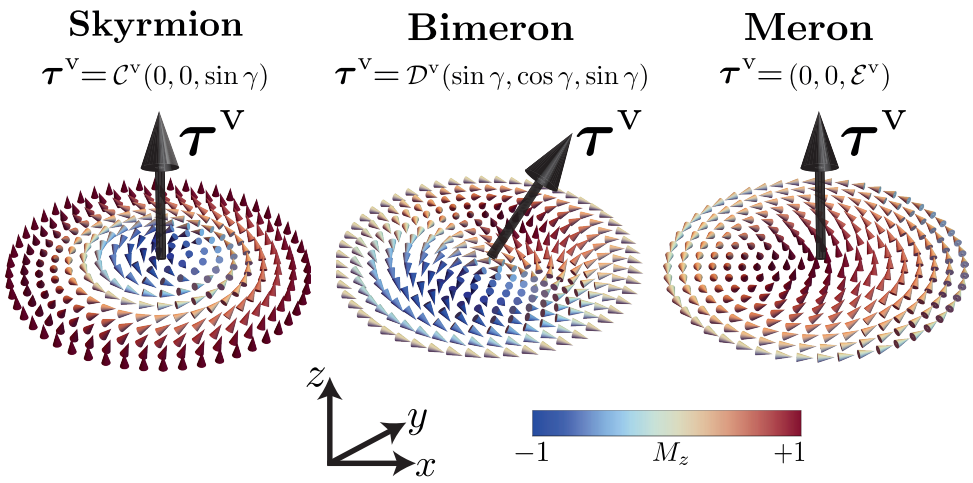

FIGURE 3.4: Skyrmion, bimeron, and meron magnetic textures. Coloring according to the z-component and the helicity is $\gamma = \pi/2$ for skyrmion and bimeron. For each texture, the black arrow illustrates the calculated volume toroidal moment.

According to the description presented in subsection 2.1.3, approximate analytical models can be used to describe the magnetic textures of skyrmions, antiskyrmions, bimerons, merons, and related configurations. These models enable the determination of their associated toroidal moments. Table 3.3 summarizes the calculated toroidal moments for these structures, considering a nanodisk of radius R and thickness d. The contributions from the surfaces, indicated in curly brackets, are included in the evaluation of the total surface toroidal moment. Figure 3.4 schematizes $\boldsymbol{\tau}^{\mathrm{v}}$ for skyrmions and bimerons, with $\gamma = \pi/2$, and for a meron.

	Skyrmion	**Bimeron**	**Meron**
$\boldsymbol{\tau}^{\mathrm{s}}$	$\mathcal{C}^{\mathrm{s}}(0,0,\sin\gamma)\vert\{S_z\}$	$(\mathcal{D}_1^{\mathrm{s}}\sin\gamma, \mathcal{D}_1^{\mathrm{s}}\cos\gamma, \mathcal{D}_2^{\mathrm{s}}\sin\gamma)\vert\{S_z\}$	$(0,0,\mathcal{E}^{\mathrm{s}})\vert\{S_z, S_\rho\}$
$\boldsymbol{\tau}^{\mathrm{v}}$	$\mathcal{C}^{\mathrm{v}}(0,0,\sin\gamma)$	$\mathcal{D}^{\mathrm{v}}(\sin\gamma,\cos\gamma,\sin\gamma)$	$(0,0,\mathcal{E}^{\mathrm{v}})$

TABLE 3.3: Surface and volume toroidal moments for skyrmions, bimerons and merons. In curly brackets are the contributing surfaces for $\boldsymbol{\tau}^{\mathrm{s}}$.

The corresponding expressions that appears in Table 3.3 which summarizes the toroidal moments for the rotating magnetization textures, such as skyrmions, bimerons

and merons are

$$\mathcal{C}^{\mathrm{s}} = -M_{\mathrm{s}} d \frac{\pi R \left[\pi^2 d^2 + 24\left(\lambda^2 + \pi^2 R^2\right)\right] \sin\left(\frac{\pi R}{\lambda}\right) - 24\lambda^3 + 12\lambda\left(2\lambda^2 - \pi^2 R^2\right)\cos\left(\frac{\pi R}{\lambda}\right)}{60\pi^2}, \tag{3.44}$$

$$\mathcal{C}^{\mathrm{v}} = M_{\mathrm{s}} d\lambda \frac{\left(2\lambda^2 - \pi^2 R^2\right)\cos\left(\frac{\pi R}{\lambda}\right) - 2\lambda\left[\lambda - \pi R \sin\left(\frac{\pi R}{\lambda}\right)\right]}{\pi^2}, \tag{3.45}$$

$$\mathcal{D}_1^{\mathrm{s}} = -M_{\mathrm{s}} \pi R d (d^2 + 12R^2) \sin\left(\frac{\pi R}{\lambda}\right), \tag{3.46}$$

$$\mathcal{D}_2^{\mathrm{s}} = -M_{\mathrm{s}} d \frac{\pi R \left[\pi^2 d^2 + 24\left(\lambda^2 + \pi^2 R^2\right)\right] \sin\left(\frac{\pi R}{\lambda}\right) - 24\lambda^3 + 12\lambda\left(2\lambda^2 - \pi^2 R^2\right)\cos\left(\frac{\pi R}{\lambda}\right)}{120\pi^2}, \tag{3.47}$$

$$\mathcal{D}^{\mathrm{v}} = M_{\mathrm{s}} d\lambda \frac{\left(2\lambda^2 - \pi^2 R^2\right)\cos\left(\frac{\pi R}{\lambda}\right) - 2\lambda\left[\lambda - \pi R \sin\left(\frac{\pi R}{\lambda}\right)\right]}{2\pi^2}, \tag{3.48}$$

$$\mathcal{E}^{\mathrm{s}} = -M_{\mathrm{s}} d R \frac{\pi^3 d^2 + 24R^2\left(\pi^3 + 4\pi - 8\right)}{60\pi^2}, \tag{3.49}$$

$$\mathcal{E}^{\mathrm{v}} = M_{\mathrm{s}} d R^3 \frac{8(\pi - 2)}{\pi^2} \tag{3.50}$$

Skyrmionic structures, first column in Table 3.3, indicate that toroidal moments are always parallel to z, i.e., to the axis of the disk. Furthermore, it is proportional to $\sin\gamma$, where γ is the helicity: $\gamma = \pi/2$ indicates a Bloch skyrmion and $\gamma = 0$ a Néel skyrmion. This means that only the Bloch skyrmion is capable of producing toroidal moments, while the Néel skyrmion is not. On the other hand, the factors $\mathcal{C}$ indicate that there is an oscillatory behavior of the toroidal moments magnitudes in relation to the period of the texture with the radius, that is, different types of Skyrmioniums or $\ell\pi$-Skyrmions can change the magnitude of the toroidal moment, even cancel its value. When considering the texture of an antiskyrmion, it is found that both the toroidal volume and surface moment are zero, which is consistent with the findings of [150].

However, bimerons have more components depending on the helicity. Namely, for $\gamma = \pi/2$, the toroidal moments lie in the $x - z$ plane, while for $\gamma = 0$, they point in the y-direction. For the volume toroidal moment of the bimeron with $\gamma = \pi/2$, it can be seen that the x and z components are balanced; however, in the surface toroidal moment, each component has different factors. To illustrate this, Figure 3.5 shows the components of τ as a function of radius R for $M_{\mathrm{s}} = 658\,\mathrm{kA/m}$, $\lambda = 40\,\mathrm{nm}$ and $d = 1\,\mathrm{nm}$. The figure shows that τ^{v} is always the smallest in magnitude, while the surface components are always larger in absolute terms. Furthermore, τ_x^{s}, in red, is significantly larger compared to the other two; note that its units are on the right vertical axis. For $\gamma = 0$, both toroidal moments have the same components with a difference in the magnitudes.

Finally, the toroidal moment was calculated for a meron-type texture using the linear function for the out-of-plane component, and a result similar to that found, for example, for the vortex state was obtained. Both the $\boldsymbol{\tau}^{\mathrm{v}}$ and $\boldsymbol{\tau}^{\mathrm{s}}$ point out of the plane parallel to the disk axis, varying only in magnitude with respect to the simplest vortex model. However, this shows that considering the core does not result in significant changes, at least in direction. Finally, it should be mentioned that these calculations allow us to go beyond disks and apply them to cylinders or strings of skyrmions, bimerons, merons, or antiskyrmions, assuming that the texture is homogeneous along the main axis. With rings or cylinders, additional care would be

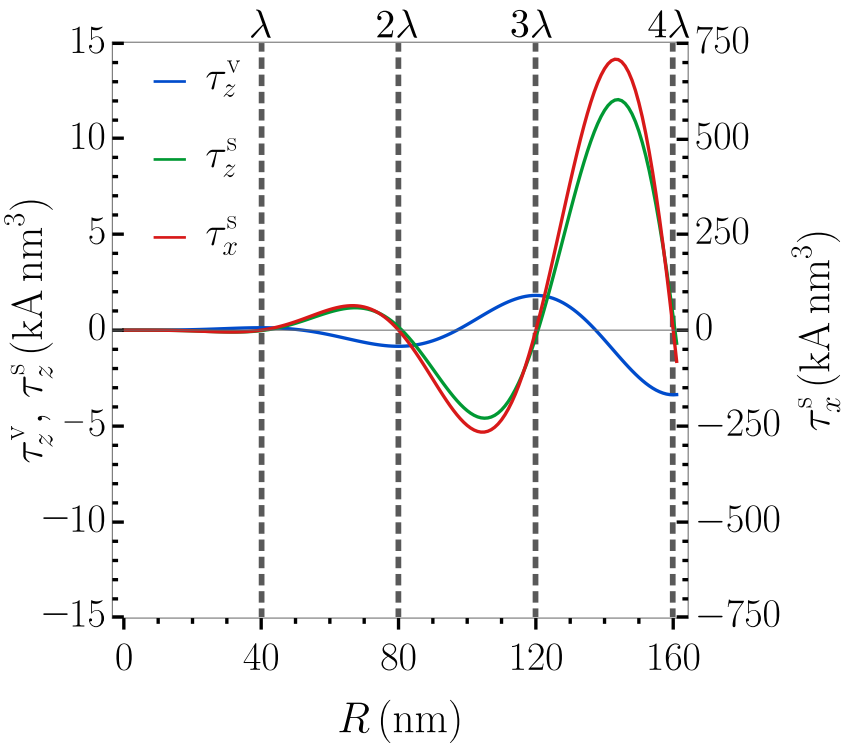

FIGURE 3.5: Volume and surface toroidal moment components for a bimeron with $\gamma = \pi/2$, $\lambda = 40$ nm and $d = 1$ nm, as a function of the radius. Vertical dashed lines indicate radii equal to multiples of λ.

needed when considering the inner and outer radii.

3.2.4 Conical-helix textures in tubes with i-DMI

Conical-helix textures are also expected to emerge in ultrathin nanotubes with interfacial DMI similar to what has been observed in planar films [125, 183]. However, in contrast to flat films, closed tubular systems exhibit quantized magnetic textures along the azimuthal direction, characterized by a quantized azimuthal component of the pitch vector $q_\phi \propto n$, where the integer n is the azimuthal index, alongside an axial pitch vector along the tube axis, q_z. In a cylindrical coordinate system, the magnetization can thus be modeled as

$$\mathbf{M} = M_{\mathrm{s}} \begin{pmatrix} \cos(n\phi + q_z z + \psi)\sin\Theta \\ \sin(n\phi + q_z z + \psi)\sin\Theta \\ \cos\Theta \end{pmatrix}, \tag{3.51}$$

where ψ denotes a phase arising from the competition between dipolar interactions and magnetic radial anisotropy, and Θ is the cone angle with respect to the tube axis. In this model, the curling state corresponds to the particular case $n = 0$, $q_z = 0$, and $\psi = \pi/2$.

The volume toroidal moment, by changing from cylindrical to Cartesian unitary vectors, i.e., $(\hat{\rho}, \hat{\phi}, \hat{z}) \to (\hat{x}, \hat{y}, \hat{z})$, and integrating in cylindrical coordinates for a thin

tube with inner radius βR, outer radius R and length L, $\boldsymbol{\tau}^{\mathrm{v}}$ becomes

$$\begin{aligned}\boldsymbol{\tau}^{\mathrm{v}} = M_{\mathrm{s}} R^2 \sin\theta \sin(n\pi) \Bigg\{ & \frac{\left(1-\beta^2\right)\cos(n\pi+\psi)}{2q_z^2(n+1)} \left[q_z L \cos\left(\frac{q_z L}{2}\right) - 2\sin\left(\frac{q_z L}{2}\right)\right] \hat{x} \\ & + \frac{\left(1-\beta^2\right)\sin(n\pi+\psi)}{2q_z^2(n+1)} \left[q_z L \cos\left(\frac{q_z L}{2}\right) - 2\sin\left(\frac{q_z L}{2}\right)\right] \hat{y} \\ & + \frac{2\left(1-\beta^3\right) R}{3q_z n} \sin\left(\frac{q_z L}{2}\right) \sin(n\pi+\psi)\hat{z} \Bigg\}. \end{aligned} \tag{3.52}$$

By inspecting the q_z and n values it is found that this expression is only nonzero for $n = 0$ and $n = -1$ and the result can be expressed as

$$\begin{aligned}\boldsymbol{\tau}^{\mathrm{v}} = & M_{\mathrm{s}} \frac{2\pi\left(1-\beta^3\right) R^3}{3q_z} \sin\Theta \sin\psi \sin\left(\frac{q_z L}{2}\right) \delta_{n,0}\hat{z} \\ & + M_{\mathrm{s}} \frac{\pi R^2 (1-\beta^2)}{2q_z^2} \sin\Theta \left[q_z L \cos\left(\frac{q_z L}{2}\right) - 2\sin\left(\frac{q_z L}{2}\right)\right] \delta_{n,-1}(\cos\psi\hat{x} + \sin\psi\hat{y}), \end{aligned} \tag{3.53}$$

where the symbol $\delta_{i,j}$ denotes the Kronecker delta function. For the particular case $q_z = 0$ and $n = 0$,

$$\boldsymbol{\tau}^{\mathrm{v}} = M_{\mathrm{s}} \frac{LR^3}{3} \pi \left(1-\beta^3\right) \sin\Theta \sin\psi\, \hat{z}. \tag{3.54}$$

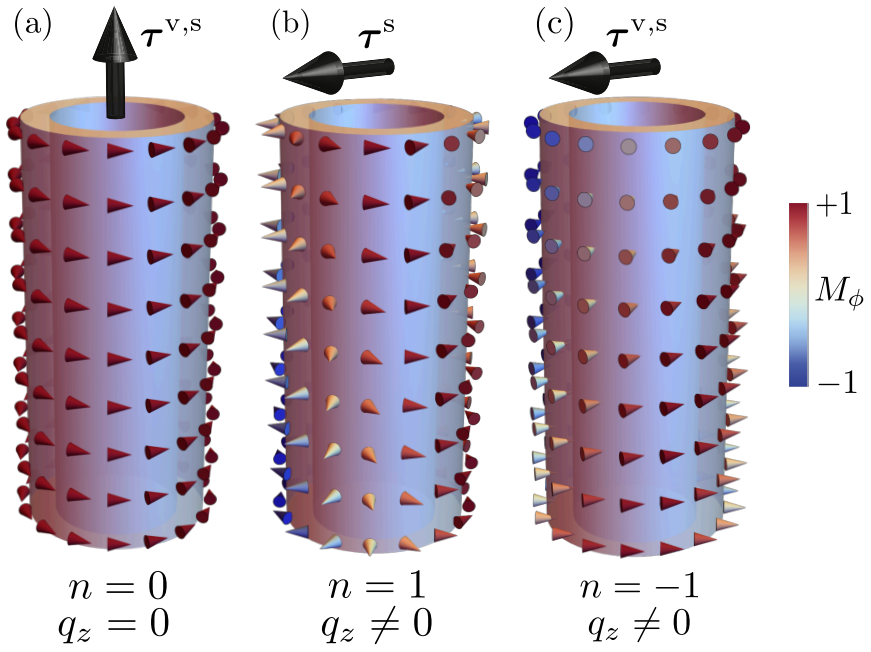

FIGURE 3.6: Illustration of three possible conical-helix magnetic textures on a nanotube described by Eq. (3.51). (a) Vortex state with $n = 0$, $q_z = 0$, and $\psi = \pi/2$, $\boldsymbol{\tau}$ points along the axis. Conical-helix state with (b) $n = 1$ and (c) $n = -1$, both with finite q_z, arbitrary ψ, resulting in toroidal moments transversal to the axis. Coloring according to the azimuthal direction of magnetization.

On the other hand, the surface toroidal moment $\boldsymbol{\tau}^{\mathrm{s}}$ for this texture is

$$\begin{aligned}\boldsymbol{\tau}^{\mathrm{s}} =& \frac{M_{\mathrm{s}}\pi(\beta-1)R\sin\Theta\sin\psi}{30q_z^3}\Bigg[3\sin\left(\frac{q_zL}{2}\right)\left(q_z^2\left(L^2+8\left(\beta^2+\beta+1\right)R^2\right)-8\right)\\ &+2q_zL\cos\left(\frac{q_zL}{2}\right)\left(\left(\beta^2+\beta+1\right)q_z^2R^2+6\right)\Bigg]\hat{z}\,\delta_{n,0}\\ &-\frac{M_{\mathrm{s}}\pi\left(\beta^2-1\right)R^2\sin\Theta\cos\psi}{20q_z^2}\Bigg[\sin\left(\frac{q_zL}{2}\right)\left(q_z^2\left(2L^2+3\left(\beta^2+1\right)R^2\right)+4\right)\\ &-2q_zL\cos\left(\frac{q_zL}{2}\right)\Bigg]\times\left(\cos\psi\,\hat{x}+\sin\,\psi\hat{y}\right)\delta_{n,-1}\\ &+\frac{M_{\mathrm{s}}\pi(\beta^2-1)R^2\sin\Theta}{20q_z^2}\left[\sin\left(\frac{q_zL}{2}\right)\left(\left(\beta^2+1\right)q_z^2R^2-4\right)+2q_zL\cos\left(\frac{q_zL}{2}\right)\right]\\ &\times\left(\cos\psi\,\hat{x}-\sin\psi\,\hat{y}\right)\delta_{n,1},\end{aligned}\tag{3.55}$$

which is only nonzero for $n=0$, $n=-1$ and $n=1$. $\boldsymbol{\tau}^{\mathrm{v}}$ does not account for this last case, that is, a toroidal moment for state $n=1$. This can be verified by calculating the total toroidal moment, which for the same texture is given by,

$$\begin{aligned}\boldsymbol{\tau} =& \frac{M_{\mathrm{s}}\pi(\beta-1)R\sin\Theta\sin\psi}{30q_z^3}\Bigg[\sin\left(\frac{q_zL}{2}\right)\left(q_z^2\left(3L^2+4\left(\beta^2+\beta+1\right)R^2\right)-24\right)\\ &+2q_zL\cos\left(\frac{q_zL}{2}\right)\left(\left(\beta^2+\beta+1\right)q_z^2R^2+6\right)\Bigg]\hat{z}\,\delta_{n,0}\\ &-\frac{M_{\mathrm{s}}\pi(\beta^2-1)R^2\sin\Theta}{20q_z^2}\left[\sin\left(\frac{q_zL}{2}\right)\left(q_z^2\left(2L^2+3\left(\beta^2+1\right)R^2\right)-16\right)+8q_zL\cos\left(\frac{q_zL}{2}\right)\right]\\ &\times\left(\cos\psi\,\hat{x}+\sin\,\psi\hat{y}\right)\delta_{n,-1}\\ &+\frac{M_{\mathrm{s}}\pi(\beta^2-1)R^2\sin\Theta}{20q_z^2}\left[\sin\left(\frac{q_zL}{2}\right)\left(\left(\beta^2+1\right)q_z^2R^2-4\right)+2q_zL\cos\left(\frac{q_zL}{2}\right)\right]\\ &\times\left(\cos\psi\,\hat{x}-\sin\psi\,\hat{y}\right)\delta_{n,1}.\end{aligned}\tag{3.56}$$

It can be noticed that the terms associated with $n=1$ are exactly the same for $\boldsymbol{\tau}$ and $\boldsymbol{\tau}^{\mathrm{s}}$ and because of that, those terms do not appear for $\boldsymbol{\tau}^{\mathrm{v}}$. Fig. 3.6 schematizes three possible states of conical-helical magnetization in tubes with i-DMI and their associated toroidal moments.

3.2.5 Cylindrical shells: Interplay between magnetization and geometry

A general magnetization configuration for thin cylindrical shells can be considered here, which can be written as

$$\mathbf{M}=M_\phi(z)\hat{\phi}+M_z(z)\hat{z}.\tag{3.57}$$

This expression can model border states at the tube caps [153, 154] or multivortex states [184, 185], among others. Such a generalized model may produce toroidal moments along different directions depending on the symmetries and explicit dependencies. For instance, in partially closed tubes up to an angle $\alpha\leq 2\pi$, as illustrated in Fig. 3.7(a), in-plane components of $\boldsymbol{\tau}$ may arise depending on the value of α and the symmetry properties of $M_\phi(z)$. The toroidal moment for this configuration

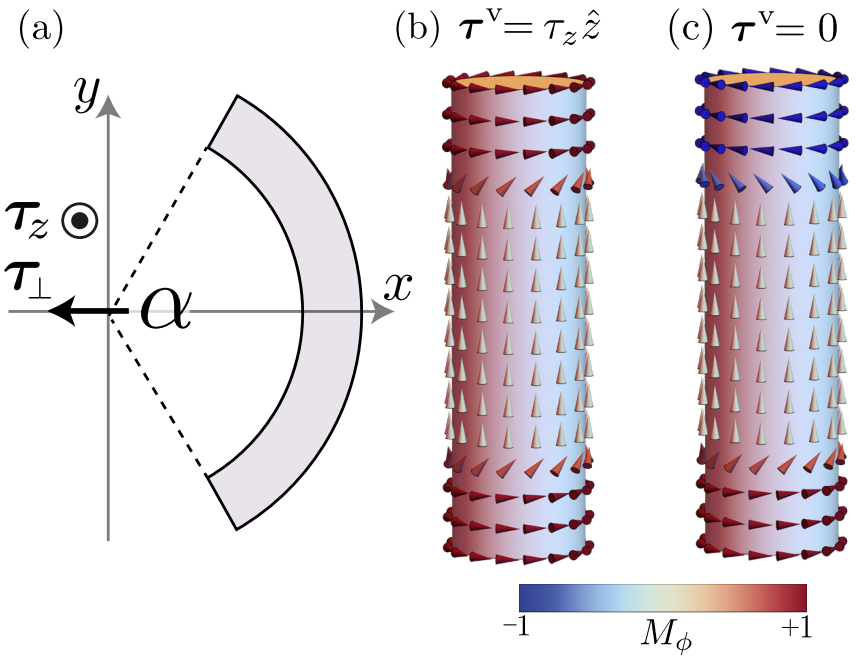

FIGURE 3.7: (a) Transversal cross-section of an incomplete tube with both axial and azimuthal magnetization components. Angle α defines the tubular section, such that $\alpha = 2\pi$ stands for a fully closed tube. As illustrated, the volume toroidal moment possesses both axial (τ_z) and transverse ($\tau_\perp$) components relative to the nanotube axis. (b-c) illustrate two closed nanotubes in an axial magnetization state, each with symmetric vortex domains at the end caps. In (b), the end vortices have the same helicity, producing a finite toroidal moment aligned with the tube axis. In (c), the vortices present opposite helicities, resulting in a zero toroidal moment.

is given by $\boldsymbol{\tau}^{\mathrm{v}} = \tau_\perp \hat{x} + \tau_z \hat{z}$, where

$$\tau_\perp = -\frac{R^2 - R_{\mathrm{i}}^2}{2} \sin\left(\frac{\alpha}{2}\right) \int_{-L/2}^{L/2} z\, M_\phi(z)\, \mathrm{d}z \tag{3.58}$$

and

$$\tau_z = \frac{R^3 - R_{\mathrm{i}}^3}{6} \left[\alpha + \frac{4}{\alpha} \sin^2\left(\frac{\alpha}{2}\right)\right] \int_{-L/2}^{L/2} M_\phi(z)\, \mathrm{d}z. \tag{3.59}$$

It can be seen that $\tau_\perp \neq 0$ for antisymmetric profiles of $M_\phi(z)$ with respect to the center of the tube. In the limit $\alpha = 2\pi$, the fully closed tube is recovered, and only the $z-$component of the toroidal moment remains, but determined by $\int dz\, M_\phi(z)$. From this, it can be easily seen, for example, that a shell with an axial state in bulk but with vortex domain states at the caps, as is illustrated in Fig. 3.7(b,c), presents a finite toroidal moment only if both vortex states have the same helicity. Otherwise, the toroidal moment cancels out. In summary, for partially closed tubes, transversal components of $\boldsymbol{\tau}^{\mathrm{v}}$ arise if $M_\phi(z)$ is asymmetric. For closed tubes, there are no transversal components. In both cases, the axial component is nonzero for symmetric $M_\phi(z)$ profiles. A similar system has been reported in Ref. [80] where the propagation of spin waves in waveguides is studied as they are curved from flat to a tubular cross-section through intermediate states, which are equivalent to a system with an angle $\alpha < 2\pi$. Some of these results are presented in the Chapter 5.

3.3 Magnetization graded structures

According to the calculations in this chapter, uniform $\mathbf{M}$ results in a zero toroidal moment, either $\boldsymbol{\tau}^{\mathrm{v}}$ and $\boldsymbol{\tau}^{\mathrm{s}}$. However, it is sufficient for M_{s} to be spatially dependent for a toroidal moment to be nonzero, even in the case of a magnetization vector along a single direction, which can be caused by an external field polarizing the sample. Consider a rectangular sample with a magnetization of the form

$$\mathbf{M}(\mathbf{r}) = M_{\mathrm{s}}(\mathbf{r})\,\mathbf{m}, \tag{3.60}$$

where $\mathbf{m} = (m_x, m_y, m_z)$ is a unit vector specifying the direction of magnetization. Assuming that the saturation magnetization varies only along some arbitrary direction $\mathbf{g}$, in rectangular coordinates. In this case, one can write

$$M_{\mathrm{s}}(\mathbf{r}) = M_{\mathrm{s}}(x_g), \tag{3.61}$$

with x_g denoting the coordinate along $\mathbf{g}$.

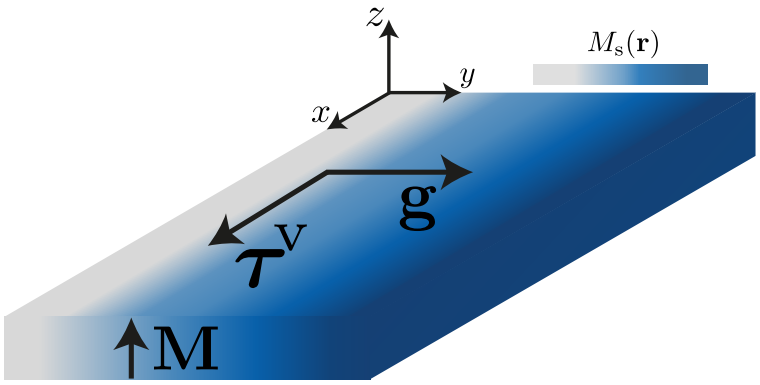

FIGURE 3.8: Graded ferromagnetic stripe with $\mathbf{M} = M_{\mathrm{s}}(x_g)\hat{z}$, where the saturation magnetization changes along a specific direction $\mathbf{g} = \hat{y}$. According to Eq. (3.64), this graded system exhibits a toroidal moment always oriented perpendicular to $\mathbf{M}$ and $\mathbf{g}$, with a magnitude that depends on the gradient profile.

The corresponding spatial average of the magnetization is then given by

$$\langle \mathbf{M} \rangle = \frac{1}{L_g} \int M_{\mathrm{s}}(x_g)\,\mathbf{m}\,\mathrm{d}x_g \equiv \langle M_{\mathrm{s}} \rangle\,\mathbf{m}, \tag{3.62}$$

where $\langle M_{\mathrm{s}} \rangle$ denotes the average value of the saturation magnetization along the direction $\mathbf{g}$. The toroidal volume moment is given by,

$$\begin{aligned}
\boldsymbol{\tau}^{\mathrm{v}} &= \frac{1}{2}\int_V \mathbf{r} \times (\mathbf{M} - \langle \mathbf{M} \rangle)\,\mathrm{d}V \\
&= \frac{1}{2}\int_V \mathbf{r} \times \left[M_{\mathrm{s}}(x_g)\mathbf{m} - \langle M_{\mathrm{s}} \rangle \mathbf{m}\right]\mathrm{d}V \\
&= \frac{1}{2}\int_V \left[(M_{\mathrm{s}}(x_g) - \langle M_{\mathrm{s}} \rangle)(ym_z - zm_y, -xm_z + zm_x, xm_y - ym_x)\right]\mathrm{d}V.
\end{aligned} \tag{3.63}$$

Here it can be seen that for a symmetric geometry, with origin at the center of the cuboid, and if M_{s} does not depend spatially, the result is canceled out. However, if

M_s is graded along the direction **g**, the result can be reduced to

$$\boldsymbol{\tau}^{v} = \frac{V}{2L_g}(\mathbf{g} \times \mathbf{m}) \int_{-L_g/2}^{L_g/2} x_g \left[M_s(x_g) - \langle M_s \rangle\right] \mathrm{d}x_g. \tag{3.64}$$

It is evident that if $M_s(x_g)$ remains constant, the integral vanishes, and consequently the volume toroidal moment is zero, i.e., $\boldsymbol{\tau}^{v} = 0$. In contrast, for a linearly graded profile of the saturation magnetization,

$$M_s(x_g) = \langle M_s \rangle + \frac{\Delta M_s}{L_g} x_g, \tag{3.65}$$

where ΔM_s denotes the total variation of the saturation magnetization across the system length L_g along the direction **g**, the expression for the toroidal moment takes the form [97]

$$\boldsymbol{\tau}^{v} = \frac{V L_g}{24} \Delta M_s \, (\mathbf{g} \times \mathbf{m}). \tag{3.66}$$

Figure 3.8 illustrates a ferromagnetic stripe with a graded saturation magnetization M_s along the width (y–direction) and an out-of-plane equilibrium magnetization (z–direction). In this configuration, an asymmetric M_s profile with respect to the stripe center gives rise to a toroidal moment oriented along the x–axis.

Chapter 4

Toroidal Moment and Magnon Nonreciprocity

4.1 Current-induced nonreciprocity

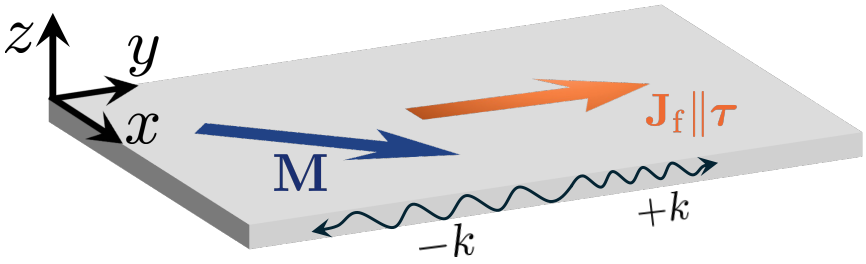

FIGURE 4.1: Ferromagnetic film with arbitrary magnetization (**M**) and a free electric current ($\mathbf{J}_\mathrm{f}$) flowing along the y–direction. The toroidal moment is parallel to the current, leading to nonreciprocal spin-wave propagation along y.

A uniform external electric current density $\mathbf{J}_\mathrm{f}$ flowing through a magnetic film of volume V gives rise to a toroidal moment according to Eq. (2.27). Consequently, a nonreciprocal propagation of spin waves is expected, as illustrated in Fig. 4.1. Considering an electric current $\mathbf{J}_\mathrm{f} = J\hat{y}$ flowing along the y-direction in a film of dimensions L_x, L_y, and L_z, with total volume $V = L_x L_y L_z$, the corresponding toroidal moment obtained from Eq. (2.27) reads

$$\boldsymbol{\tau} = -\frac{VJ}{12}(2L_x^2 + L_y^2 + 2L_z^2)\,\hat{y}, \tag{4.1}$$

which implies $\boldsymbol{\tau} \propto -V\,\mathbf{J}_\mathrm{f}$. This expression explicitly connects the toroidal moment to the macroscopic flow of charge carriers within the medium. Consequently, the nonreciprocity condition $\boldsymbol{\tau} \cdot \mathbf{k} \neq 0$ becomes equivalent to $\mathbf{J}_\mathrm{f} \cdot \mathbf{k} \neq 0$, indicating that nonreciprocal propagation arises whenever the spin-wave wave vector possesses a finite projection along the direction of the current. This result is fully consistent with previous theoretical and experimental studies. Indeed, an electric current, via spin-transfer torque, introduces a linear term in the magnonic dispersion relation, producing a Doppler-like frequency shift $\Delta f \propto \mathbf{J}_\mathrm{f} \cdot \mathbf{k}$, as originally predicted by theory [175, 186] and later confirmed experimentally in saturated ferromagnetic films [176, 187]. Figure 4.2 presents the experimental results reported by Vlaminck *et al.* (2008), where the influence of a direct current, acting through adiabatic spin-transfer torque (STT), on the propagation of spin waves in an out-of-plane magnetized permalloy

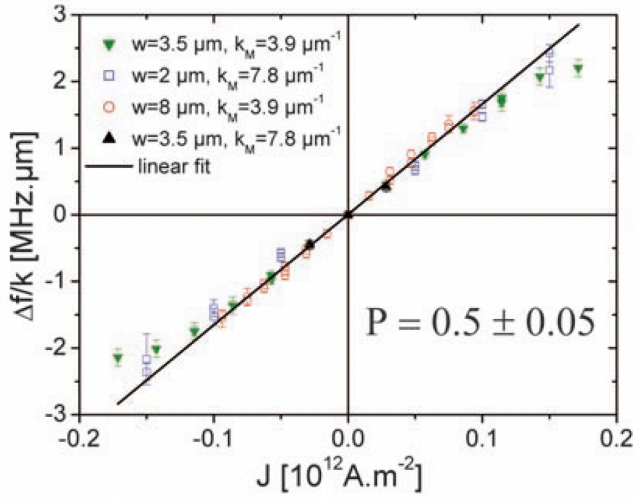

FIGURE 4.2: Experimental frequency shifts versus current density, normalized by k, where a linear response was achieved. Adapted from Ref. [176].

strip was investigated. The measurements revealed a clear nonreciprocal behavior in the spin-wave propagation.

Beyond this result, it can be observed that even in the presence of space-dependent magnetization, a free electric current inherently induces a finite toroidal moment, leading to nonreciprocal magnon transport. Moreover, when spatially nonuniform current distributions are considered, the analysis indicates that the resulting toroidal moment remains locally aligned with the current density, both for bulk and surface currents. Interestingly, the toroidal moment is cancelled for current densities with odd functions, always assuming spatially symmetric geometries, i.e., $(\mathbf{J} \propto J_0, J_0x^2, \ldots)$. However, it is always nonzero for even currents $(\mathbf{J} \propto J_0x, J_0x^3, \ldots)$. Nevertheless, the implications of a zero toroidal moment in particular cases need to be investigated further and are beyond the scope of this research. Finally, this demonstrates the intrinsic and robust nature of the current-induced toroidal character, establishing it as a fundamental feature of electrically driven magnonic systems.

On the other hand, it can be shown that the imaginary part of the spin-transfer torque magnetic tensor (due to an electric current $\mathbf{J}_\mathrm{f}$) is given by [188]

$$\mathrm{Im}[\mathcal{N}^{(21)}_{\mathrm{stt}}(\mathbf{k})] = \frac{\mu_\mathrm{B}\mathcal{P}}{\gamma\mu_0 M_\mathrm{s}^2 e}\left(\frac{1+\alpha\beta}{1+\beta^2}\right)(\mathbf{J}_\mathrm{f}\cdot\mathbf{k}), \tag{4.2}$$

which shows that the STT frequency nonreciprocity is linear in the wave vector [175, 176, 186]. Here, α is the Gilbert damping, β is the nonadiabatic STT term, μ_B the Bohr magneton, e the absolute value of the electron charge, and $\mathcal{P}$ the spin polarization. The adiabatic and nonadiabatic contributions to the effective field, for low currents, are proportional to $\mathbf{M}\times(\mathbf{J}_\mathrm{f}\cdot\nabla)\mathbf{M}$ and $(\mathbf{J}_\mathrm{f}\cdot\nabla)\mathbf{M}$, respectively. These STT effective fields do not accurately capture the dynamics for higher currents. As $\boldsymbol{\tau}\propto\mathbf{J}_\mathrm{f}$, it can be concluded that $\Delta f_{\mathrm{stt}}\propto(\boldsymbol{\tau}\cdot\mathbf{k})$, which is always linear in k for low current densities.

4.2 Texture-based nonreciprocity

Noncollinear forms of the magnetization [59, 77, 189] are able to produce toroidal moments in the absence of free currents but due to bound currents, as was already

shown in section 3.2. Examples of such noncollinear magnetizations are conical-helix (Bloch or Néel type) [61, 65, 124, 190, 191], vortex-like [18], skyrmion-like [140, 150, 192], or hopfion-like magnetic textures [193, 194]. The following subsections establish a connection between the findings presented in the previous section on the toroidal moments of these magnetic textures and the reports in the literature concerning spin-wave propagation in such states.

4.2.1 Conical-helical textures in thin films

Conical–helical (CH) magnetic textures stabilized by Dzyaloshinskii–Moriya interactions (DMI), among other competing interactions, in thin films such as those discussed in Subsection 3.2.1, give rise to finite toroidal moments, as previously demonstrated. In these systems, the xy-plane corresponds to the film plane, while the z-axis is oriented normal to it. The corresponding results are summarized in Table 3.1. These textures are primarily characterized by a pitch vector $\mathbf{q}$, analogous to a wave vector $\mathbf{k}$, which defines both the direction of periodicity and the associated wavelength ($\lambda = 2\pi/q$). One of the main findings is that the toroidal moment is always oriented perpendicular to the pitch vector, while other parameters, such as the helicity or phase, can further determine its specific direction. For an external magnetic field applied along the y-axis, it was shown that bulk DMI (b-DMI) stabilizes a Bloch-like texture with $\mathbf{q} = q\hat{y}$, whereas interfacial DMI (i-DMI) favors a Néel-like configuration with $\mathbf{q} = q\hat{x}$. As was reported in the previous section, the toroidal moments for the textures stabilized by b-DMI are parallel to $x(z)$, for the phase $\psi = \pi/2\,(0)$. Meanwhile for the one stabilized by i-DMI, $\boldsymbol{\tau}$ is only parallel to y for $\psi = \pi/2$ and zero for $\psi = 0$.

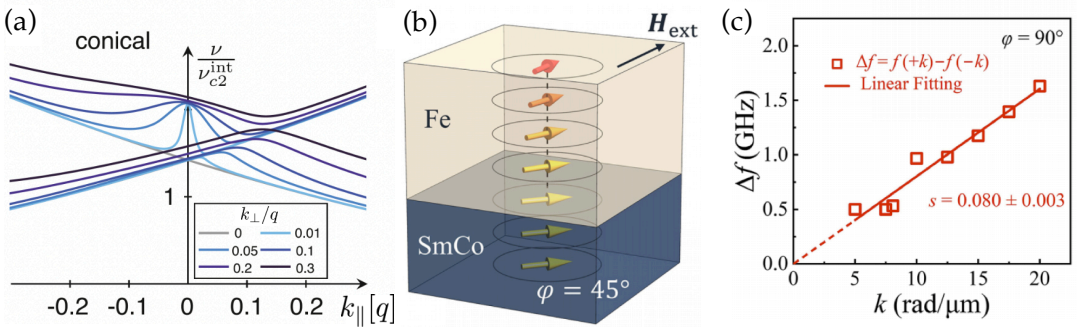

FIGURE 4.3: Nonreciprocal behavior in systems with magnetic textures. (a) Spin-wave dispersion relations for a conical magnetic state in a chiral magnet, where the horizontal axis ($k_\parallel$) represents the wavevector component parallel to the pitch vector. Different colors correspond to spin waves with varying perpendicular components of the wavevector. Nonreciprocity arises for $k_\perp \neq 0$. (b) Magnetic texture resulting from the interaction between two magnetic layers, which depends on the angle φ between the external magnetic field and the in-plane easy axis of the bottom layer. (c) Frequency shift of spin waves propagating at $\varphi = 90°$, with the wavevector $\mathbf{k}$ oriented perpendicular to the external magnetic field, as shown in (b).

These results and the nonreciprocity condition are consistent with the work from Ogawa *et. al* [66], where asymmetric dispersions were reported for spin waves excited over CH states in a Cu_2OSeO_3 single crystal with bulk DMI. Here, a frequency shift was observed for spin waves with a wavevector parallel to $\boldsymbol{\tau}^{\text{v}} = \tau_x^{\text{v}}\hat{x}$ (and perpendicular to $\mathbf{H}$), which is not the case for uniformly magnetized films with

bulk DMI, where nonreciprocity occurs for $\mathbf{k} \parallel \mathbf{H}$ [89]. The difference arises solely from the texture. It is worth noting that no analytical expressions currently exist for the frequency nonreciprocity or the effective magnetic tensor associated with the conical-helical texture, making the toroidal moment estimation very relevant for determining the presence or absence of nonreciprocity arising from spin-helical magnetic textures. A similar study was reported by Jiang et al. [195], who investigated the spin-wave dynamics in an exchange spring (ES) bilayer, where the competition between the magnetic materials, the in-plane easy axis anisotropy, and the external magnetic field gives rise to a Bloch-type magnetic texture gradually evolving from one layer to the other. According to our analysis based on the toroidal moment, such a configuration would yield an in-plane toroidal moment, consistent with their observation of nonreciprocal spin-wave propagation, which propagates perpendicular to the external field.

Recently, the work of Micaletti et al. [196] shows the spin-wave properties for a sinusoidal magnetization distribution which serves as a magnonic crystal based on texture. They take into account in-plane and out-of-plane sinusoidal undulations. The magnetization has the form,

$$\mathbf{m} = m_x(x)\hat{x} + m_y(x)\hat{y} + m_z(x)\hat{z}. \tag{4.3}$$

For this distribution, the volume toroidal moment calculated in a square film with length side L and thickness d is given by,

$$\boldsymbol{\tau}^{\mathrm{v}} = \frac{Ld}{2}\int_{-L/2}^{L/2} x\left[-m_z(x)\hat{y} + m_y(x)\hat{z}\right]\mathrm{d}x. \tag{4.4}$$

From this, it can be seen that if the magnetization points in-plane, the toroidal moment only has out-of-plane components. On the other hand, if the distribution has an out-of-plane component, a toroidal moment arises in the plane but perpendicular to the modulation axis (x here). Of course, the particular shape of the functions $m_i(x)$ and their spatial symmetry can also cancel out $\boldsymbol{\tau}$. This in perfect agreement with was already shown in previous chapter, particularly in Eq. 3.43, with $\boldsymbol{\tau} \propto \mathbf{m} \times \mathbf{G}$. Here $\mathbf{G}$ is parallel to the $x-$axis, the texture-variation direction. The authors point out that all calculated dispersions are reciprocal, both in Damon–Eshbach and Backward Volume configurations, for both out-of-plane and in-plane components. Although nonreciprocity could be expected in the case with out-of-plane magnetization and Damon–Eshbach configuration, the methodology used (via micromagnetic simulations) and the symmetry of the periodicity can cancel out the nonreciprocal effects.

As was already stated in the previous chapter, if more periodicities are present in the texture, they can be considered separately and analyzed for their contribution to the toroidal moment. In those cases, studying the toroidal moment associated with each periodicity vector $\mathbf{G}$ offers a straightforward way to identify nonreciprocal wave directions as well as the possibility of studying ferrotoroidal orders in molecular systems [102, 197] and artificial spin ices [114, 198, 199].

4.2.2 Skyrmionic textures

Skyrmionic or vortex textures in confined nanostructures produce toroidal moments pointing out of the plane for the vortex, meron, skyrmion, and bimeron textures, with the latter also exhibiting an in-plane component (see Table 3.4), based on simple analytical models for such textures [136, 150]. These toroidal-moment calculations are consistent with theoretical and experimental observations reported for

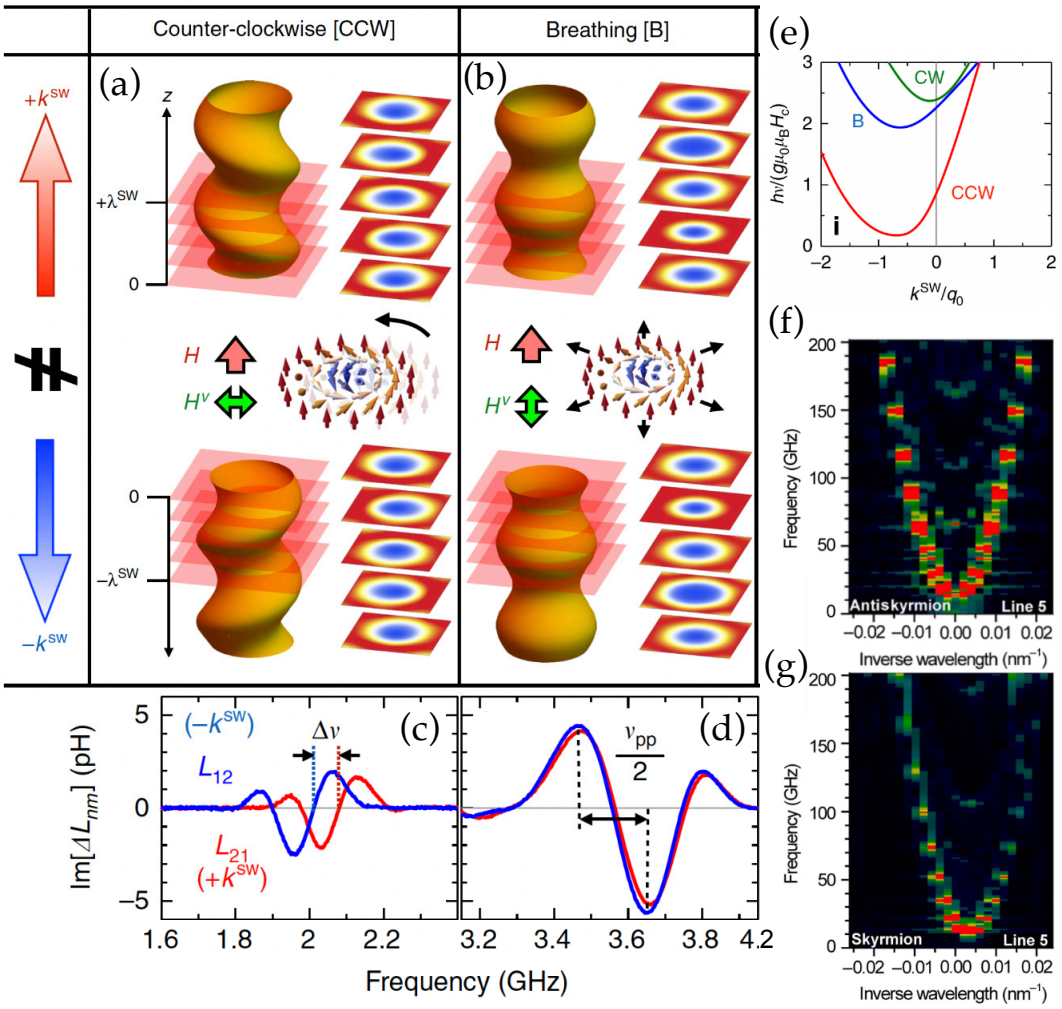

FIGURE 4.4: Spin-wave propagation along Skyrmion strings and Skyrmion/Antiskyrmion-based waveguides. (a–b) Schematic representation of counterclockwise and breathing spin-wave modes in Bloch-type Skyrmion strings, excited at $z = 0$ by an oscillating magnetic field H^v. The modes propagate nonreciprocally along the $\pm z$ directions. (c–d) Experimental measurements of the mutual inductances ΔL_{21} and ΔL_{12} in Cu_2OSeO_3, corresponding to spin waves with wavevectors $+k^{SW}$ and $-k^{SW}$, respectively, for the same modes shown above. (e) Theoretical dispersion relations of the distinct spin-wave modes. Figures extracted from Ref. [141]. (f–g) Spin-wave dispersions obtained from micromagnetic simulations for (f) antiskyrmion and (g) skyrmion tubes. The antiskyrmion spectrum remains reciprocal, whereas the skyrmion spectrum exhibits pronounced nonreciprocity. Figures extracted from Ref. [64].

skyrmion strings [141], as well as for skyrmion- and antiskyrmion-based magnonic waveguides studied through micromagnetic simulations [64]. Seki *et al.* investigated skyrmion strings, understood as arrays of parallel skyrmion tubes in the chiral magnet Cu_2OSeO_3. The temperature and the external magnetic field applied along the tube axis are key control parameters that stabilize Bloch-type skyrmion tubes, i.e., skyrmions extended continuously along the field direction. In their experiments, the skyrmion-string phase was stabilized at $T = 25$ K under a weak axial

field of approximately 20 mT. Using Au coplanar waveguides, they performed spin-wave spectroscopy by exciting the system with oscillatory magnetic fields H^{ν} and detecting the magnetic contribution to the complex mutual inductances ΔL_{12} and ΔL_{21} (normalized to a background). These mutual inductances are directly related to the propagation direction of the spin waves. Figures 4.4(a–b) schematically illustrate two characteristic eigenmodes of skyrmions: the counter-clockwise (CCW) and the breathing mode. The black arrows indicate the local sense of magnetization precession, and the propagation occurs along the z direction. The corresponding experimental spectra for ΔL_{21} and ΔL_{12} are presented in Figs. 4.4(c–d), revealing a pronounced spectral asymmetry, particularly for the CCW mode, which directly reflects the nonreciprocal nature of the spin-wave propagation. Complementary theoretical calculations of the dispersion relations, shown in Fig. 4.4(e), also confirm the strong nonreciprocity. Microscopically, this asymmetric propagation originates from the combined effects of the DMI and dipolar interactions inherent to Bloch-type skyrmions.

In parallel, Xing *et al.* [64] studied skyrmion and antiskyrmion tubes by means of micromagnetic simulations using OOMMF. In their model, skyrmion tubes, with squared cross-section, were stabilized by bulk-type DMI, whereas antiskyrmion tubes were stabilized by the D_{2d} form of DMI. After stabilization, spin waves were excited to propagate along the tube axis, and the resulting dispersion relations are plotted in Figs. 4.4(f–g). Antiskyrmion tubes exhibit a fully reciprocal dispersion relation, consistent with their vanishing toroidal moment. In contrast, skyrmion tubes display clear nonreciprocity, in agreement with the experimental findings of Seki *et al.* and with the fact that Bloch-type skyrmions possess a finite toroidal moment aligned with the tube axis. From these results, one can expect similar behavior for SWs propagating along bimeron-like structures such as strings or lattices since their toroidal moment, depending on γ, can point in any of the three main directions. Similar to the conical-helix texture, no analytical expressions are available for Δf, which makes the toroidal moment calculation very relevant for addressing the presence of nonreciprocity in skyrmionic textures.

4.3 Texture-based nonreciprocity in curved shells

Magnon propagation along the axis of nanotubes exhibiting vortex or curling magnetization states has been investigated. In these systems, asymmetric dispersion relations arising from the magnetostatic interaction have been theoretically predicted [14–19, 21] and experimentally observed [79]. As discussed in Subsection 2.1.3, the magnetization texture of the curling state, expressed in the cylindrical basis, is given by

$$\mathbf{M} = M_{\mathrm{s}}\big(0, \chi \sin\Theta, \cos\Theta\big), \tag{4.5}$$

where χ denotes the helicity (± 1) around the z-axis, and Θ represents the constant polar angle between the equilibrium magnetization and the z-axis. These magnetization textures generate finite toroidal moments of the form

$$\boldsymbol{\tau}^{\mathrm{v}} = \frac{\pi}{3}(R^3 - R_{\mathrm{i}}^3) L \chi M_{\mathrm{s}} \sin\Theta\, \hat{z}, \tag{4.6}$$

$$\boldsymbol{\tau}^{\mathrm{s}} = -\frac{\pi}{60} L d \left[L^2 + 28(R^2 + R R_{\mathrm{i}} + R_{\mathrm{i}}^2)\right] \chi M_{\mathrm{s}} \sin\Theta\, \hat{z}, \tag{4.7}$$

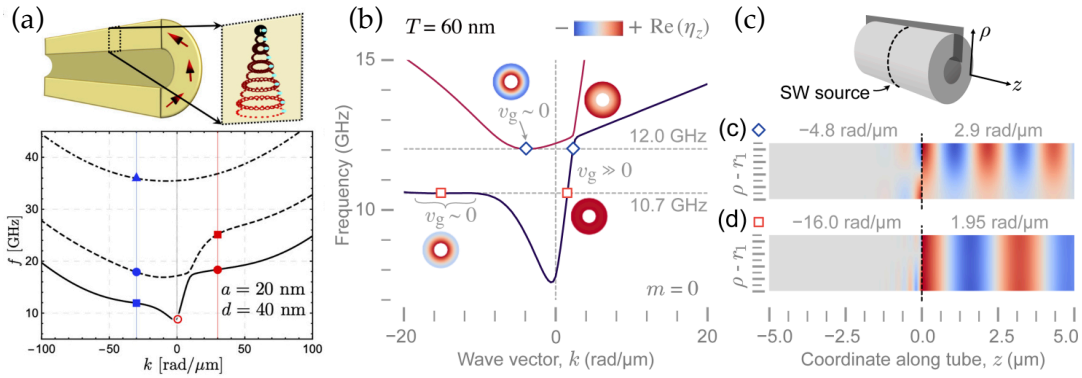

FIGURE 4.5: Spin-wave nonreciprocity in magnetic nanotubes with a vortex magnetic state. (a) Spin-wave dispersion for a tube with inner radius $a = 20$ nm and thickness $d = 40$ nm (adapted from Ref. [17]). (b) Spin-wave dispersion for a tube with thickness T = 60 nm, where different group velocity regimes are indicated. (c) Dynamic magnetization profiles at selected excitation frequencies, illustrating unidirectional spin-wave propagation (adapted from Ref. [18]).

where $R_i(R)$ is the internal(external) tube radius and $d = R - R_i$ is the shell thickness. For a vortex configuration, $\Theta = \pi/2$, and $\boldsymbol{\tau}^{\mathrm{v,s}}$ are parallel to the tube axis [18], explaining the emergence of dipolar nonreciprocity along the axis for this magnetic state. Fig. 4.5 shows spin-wave dispersions and dynamic magnetization profiles for tubes with vortex magnetic states, based on Refs. [17, 18]. One can clearly observe the nonreciprocity in the spectra in panels (a) and (b) for tubes with similar geometrical parameters, as well as the unidirectional propagation of spin waves at specific excitation frequencies in panel (c). In contrast, for axial magnetization, $\Theta = 0$ and $\boldsymbol{\tau}^{\mathrm{v}} = \boldsymbol{\tau}^{\mathrm{s}} = 0$, which indicates the symmetry in the propagation of spin waves along z, in agreement with previous works [14–21]. The curling magnetization in a closed nanotube is a particularly notable case, because analytical expressions for the frequency nonreciprocity are available. These include solutions incorporating purely dipolar interactions [14, 15, 17–19], both dipolar and exchange interactions [16], and the combined contributions of dipolar, exchange, and DMI [20, 21]. In the latter case, due to curvature, the spin waves are characterized by an axial wave vector k_z and a quantized azimuthal wave vector proportional to the mode-index $l = 0, \pm 1, ...$, that is $\mathbf{k} = k_z\hat{z} + (l/R)\hat{\phi}$. Then, the relevant magnetic tensors [see Eq. (2.40)], associated with each energy term, can be obtained, which leads to three contributions to the frequency asymmetry

$$\Delta f^{\mathrm{dip}} = -\frac{\mu_0\gamma}{\pi}\left(R_{\mathrm{m}}k_z M_\phi - Rk_\phi M_z\right)\mathcal{I}_1^{k_z,l}, \tag{4.8}$$

$$\Delta f^{\mathrm{ex}} = -\frac{\mu_0\gamma}{\pi}k_\phi M_z\left(\frac{2\ell_{\mathrm{ex}}^2}{R_i}\right), \tag{4.9}$$

and

$$\Delta f^{\mathrm{dm}} = \frac{\mu_0\gamma}{\pi}\left(\frac{2D}{\mu_0 M_{\mathrm{s}}^2}\right)\left(k_z M_\phi - k_\phi M_z\right), \tag{4.10}$$

respectively associated with the dipolar, exchange, and interfacial Dzyaloshinskii–Moriya interactions. Here, $R_{\mathrm{m}} = (R + R_i)/2$ is the average radius, D is the DM strength, ℓ_{ex} is the exchange length and $\mathcal{I}_1^{k_z,l}$ is an azimuthal integral arising from

dipolar coupling that is even in k_z and also depends on the mode-index l [20, 21]. Although there are three clearly identified sources of nonreciprocity, for the purposes of this thesis, only dipolar and DM interactions are relevant due to the fact that the linear toroidal moment is a global property and cannot account for the exchange-induced nonreciprocity from curvature, nor a circulating toroidal moment. In the small k_z limit, the leading term in $\mathcal{I}_1^{k_z,l}$ is a constant, explaining the linear Δf. Interestingly, in the thin-shell limit,

$$\Delta f^{\mathrm{dm+dip}} = -\frac{\mu_0\gamma}{\pi}\left(\frac{2D}{\mu_0 M_\mathrm{s}^2} + \frac{d}{2}\delta_{l,0}\right)(\mathbf{M}\times\hat{n})\cdot\mathbf{k}, \tag{4.11}$$

where $\hat{n} = \hat{\rho}$ is the normal to the cylindrical shell [97]. It is important to mention that higher-order contributions [$\mathcal{O}(k_z^2)$] in $\mathcal{I}_1^{k_z,l}$ arise for larger k_z [20, 21], which leads to a nonmonotonic $\Delta f(k)$ typical of the nonlocal dipolar coupling, which is the only energy term that produces a nonlinear term in $\Delta f(k_z)$. In the small k_z limit, and for ultrathin shells, the dipolar and DMI contributions are proportional to $\mathbf{K}_b\cdot\mathbf{k}$, where $\mathbf{K}_b = \mathbf{M}\times\hat{\rho}$ is the bound surface current in the outer cylindrical shell, leading to a surface toroidal moment proportional to $\mathbf{M}\times\hat{n}$ [200].

4.4 Magnon nonreciprocity in graded films, bilayers and multilayers

Section 3.3 presented the expressions for the toroidal moment in a ferromagnetic film with a graded saturation magnetization M_s, a representative configuration of which is shown in Fig. 4.6(a). From Eq. (3.64), it follows that if $(\mathbf{g}\times\mathbf{m}) \parallel \mathbf{k}$, spin-wave nonreciprocity is expected. This situation occurs, for instance, for Damon–Eshbach modes in a film magnetized parallel to the external field but with an M_s gradient along the normal, characterized by asymmetric profiles with respect to the film center [22]. On the other hand, the system should be reciprocal if $(\mathbf{g}\times\mathbf{m}) \perp \mathbf{k}$, as was already reported in Ref. [201] for the particular case of a laterally graded stripe. Note that the integral in Eq. (3.64) vanishes for any symmetric profile centered at $x_\mathrm{g} = 0$. Therefore, Eq. (3.64) suggests that for graded films $\Delta f \propto (\mathbf{g}\times\mathbf{m})\cdot\mathbf{k}$, which generalizes the results in Refs. [22, 201] for small wave vectors, and allows to predict the existence of nonreciprocity in a more general way.

The predicted nonreciprocity is now illustrated with an example. Fig. 4.6 shows a thin magnonic waveguide magnetized in the normal direction (z), which is graduated along the width (y), and spin waves propagate along x. In Fig. 4.6(c), a linear (asymmetric) graded magnetization profile is considered, resulting in a nonreciprocal dispersion, while in Fig. 4.6(d), a symmetric profile results in $\Delta f = 0$, since $\boldsymbol{\tau}^\mathrm{v} = 0$, regardless of the orientation of the wave vector. Both dispersions were obtained using the finite-element micromagnetic package TETRAX [164, 202]. TETRAX is a micromagnetic package that allows one to obtain the equilibrium states of magnonic waveguides as well as confined structures, and subsequently to compute the spin-wave spectrum by solving the LLG equation using the dynamical matrix method. The simulated system is a stripe with a cross-sectional width of 200 nm and a thickness of 60 nm, assuming translational invariance along the spin-wave propagation direction (x-axis). The magnetic parameters used are a gyromagnetic ratio $\gamma = 185.66$ GHz/T and an exchange stiffness constant $A_\mathrm{ex} = 10$ pJ/m. To saturate the sample, an external magnetic field of $B_\mathrm{ext} = 1$ T was applied along the normal direction. Two distinct saturation magnetization profiles were considered

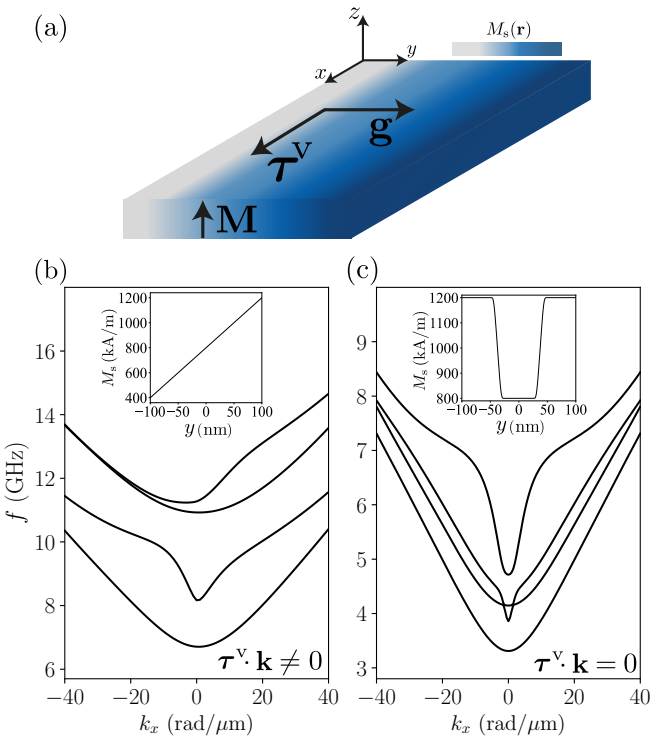

FIGURE 4.6: (a) Graded ferromagnetic stripe with $\mathbf{M} = M_s(x_g)\hat{z}$, where the saturation magnetization changes along a specific direction $\mathbf{g} = \hat{y}$. According to Eq. (3.64), this graded system exhibits a toroidal moment always oriented perpendicular to $\mathbf{M}$ and $\mathbf{g}$, with a magnitude that depends on the gradient profile. (b–c) Spin-wave dispersion spectra obtained from TETRAX for stripes with magnetization gradients, showing the four lowest-frequency modes. In (b), the saturation magnetization profile is linear and asymmetric, resulting in a toroidal moment and nonreciprocal spin-wave propagation. In (c), the magnetization profile is mirror-symmetric concerning the film center, leading to a vanishing toroidal moment and a reciprocal dispersion. Insets show the respective magnetization saturation profiles across direction x.

across the stripe width: a linear gradient and a symmetric profile. In both cases, the saturation magnetization M_s ranges from a minimum of 400 kA/m to a maximum of 1200 kA/m [see insets of the Figure 4.6(c-d)]. A specific class of magnetization-graded systems can be achieved using two ferromagnetic layers made of different materials in direct contact, each one uniformly magnetized. Here, $M_s(x_g)$ changes abruptly, and the bilayer can then be regarded as a graded system with a sharp step in M_s at the interface. Nonreciprocal waves have been measured with Brillouin light scattering (in Damon-Eshbach configuration) in parallelly magnetized Ni/NiFe [203], and CoFeB/NiFe bilayers [27], in perfect agreement with the predictions of Eq. (3.64). In a thick film that has a graduation of the saturation magnetization along the normal direction, it has been shown that $\Delta f(k)$ increases linearly, reaches a maximum value, and then decreases [22]. Because there is no analytical formula describing the associated magnetic tensor $\mathcal{N}^{(21)}(\mathbf{k})$ nor the frequency shift, the toroidal moment evaluation constitutes a very useful tool to anticipate the existence of nonreciprocity in graded magnetic films, which has only been determined numerically [22] and more recently measured in Nitrogen-implanted Fe films [23],

in full agreement with the insights provided by the toroidal moment in Eq. (3.64).

A magnetic multilayer comprising layers with different saturation magnetizations and distinct magnetization orientations can likewise be regarded as a particular realization of a graded system. In the specific case of a bilayer composed of two magnetic films with top/bottom surface area L^2, different thicknesses ($d_{1,2}$) and saturation magnetizations ($M_{s1,2}$), separated by a nonmagnetic spacer of thickness s [see Fig. 4.7(a)], depending on whether the magnetization in the lower layer $\mathbf{M}_1 = M_{s1}\mathbf{m}$ and upper layer $\mathbf{M}_2 = \sigma M_{s2}\mathbf{m}$ are parallel ($\sigma = +1$) or antiparallel ($\sigma = -1$), the average magnetization field is

$$\langle \mathbf{M} \rangle = \frac{M_{s1}d_1 + \sigma M_{s2}d_2}{d_1 + d_2}\mathbf{m} \equiv \langle M \rangle \mathbf{m}, \tag{4.12}$$

and the toroidal moment, according to Eq. (3.64), becomes

$$\boldsymbol{\tau}^{\mathrm{v}} = -\frac{L^2}{4}\frac{d_1 d_2 (d_1 + d_2 + 2s)}{(d_1 + d_2)}(M_{s1} - \sigma M_{s2})\,(\hat{z} \times \mathbf{m}). \tag{4.13}$$

This formula explicitly shows that the toroidal moment vanishes only for bilayers with parallel magnetizations ($\sigma = 1$) and $M_{s1} = M_{s2}$, as is schematized in Fig. 4.7(b). In all other cases, where the bilayers have antiparallel magnetizations, or they are parallel but with different M_s, the toroidal moment calculation suggests that nonreciprocity occurs for waves propagating parallel to $(\hat{z} \times \mathbf{m})$, with z being normal to the bilayer surface [24–28], as shown in Fig. 4.7(c,f,g). Nevertheless, these calculations can be extended to predict nonreciprocity in much more complex systems, such as multilayers composed of different magnetic materials and thicknesses. Fig. 4.7(b-i) summarizes the toroidal moments obtained for parallel (left) and antiparallelly (right) magnetized bilayers and trilayers, composed of (b-e) identical and (f-i) nonidentical magnetic materials. Through simple calculations, it can be shown that an antiferromagnetically coupled multilayer system (with magnetizations oriented along $\pm y$), with identical M_s and thicknesses, exhibits a nonzero toroidal moment along the in-plane x-direction if the number of layers is even. In contrast, when the number of identical layers is odd, the toroidal moment is zero, as can be seen in Fig. 4.7(d-e) for a trilayer configuration. However, for any number of layers, a finite toroidal moment emerges if the symmetry is broken along the normal concerning the multilayer center. This symmetry breaking can be achieved through the modulation of M_s, as depicted in Fig. 4.7(f-i), or thicknesses. This behavior applies to both ferromagnetic and antiferromagnetic coupled layers.

For a symmetric bilayer ($d_1 = d_2 = d$) with two identical ferromagnetic layers but antiparallel ($\sigma = -1$) the toroidal moment from Eq. (4.13) is $\boldsymbol{\tau}^{\mathrm{v}} = -\frac{L^2}{2}d(d + s)(\hat{z} \times \mathbf{M})$, such as depicted in Fig. 4.7(c). The antiparallelly magnetized symmetric bilayer is a particular case that allows for a simple analytical formula for the magnon frequency shift induced by the dynamic dipolar coupling in an extended wave-vector regime, which leads to a magnetic tensor [25]

$$\mathrm{Im}[\mathcal{N}^{(21)}(\mathbf{k})] = 2\sinh^2\left(\frac{kd}{2}\right)\frac{e^{-|k|(d+s)}}{kd}, \tag{4.14}$$

which is nonlinear with k. Only in the low-k regime, $\mathrm{Im}[\mathcal{N}^{(21)}(\mathbf{k})] \approx kd/2$ and the frequency shift is linear with k, which allows to write $\Delta f \propto \boldsymbol{\tau} \cdot \mathbf{k} \propto (\hat{z} \times \mathbf{M}) \cdot \mathbf{k}$.

Interestingly, the work of Kuznetsov and Fraerman [200] theoretically investigated spin-wave nonreciprocity in hybrid films consisting of a thin ferromagnet

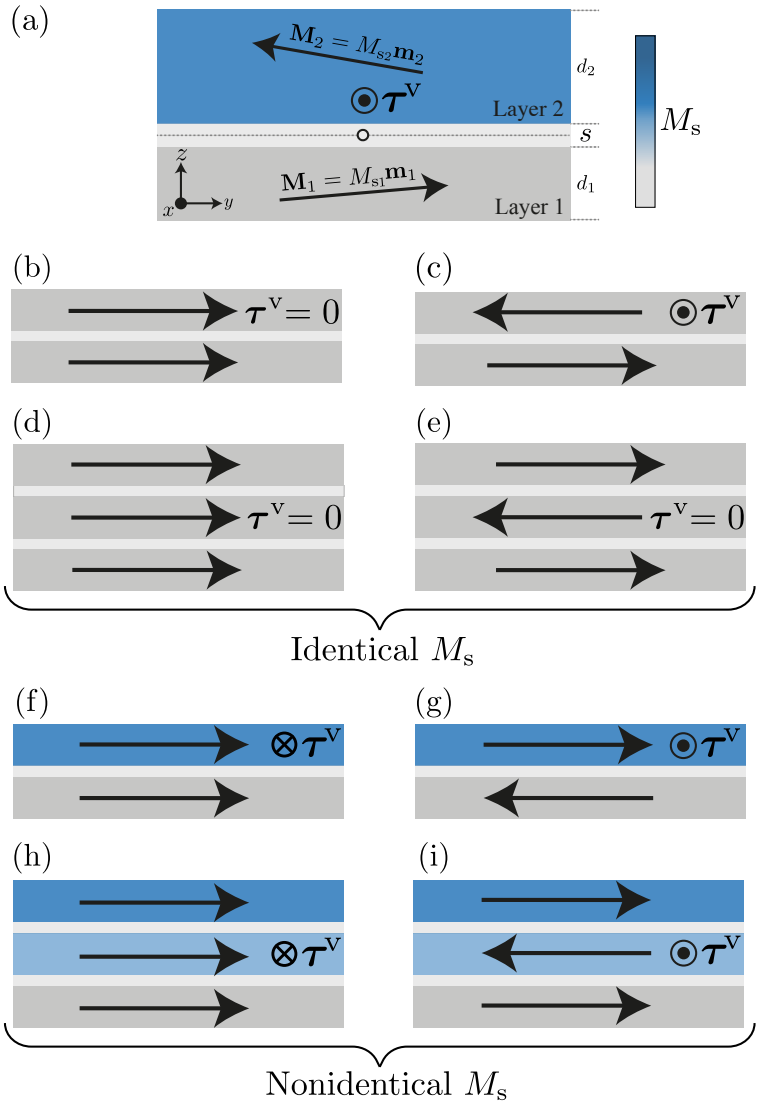

FIGURE 4.7: (a) Asymmetric ferromagnetic bilayer having thicknesses $d_{1,2}$ and magnetizations $\mathbf{M}_{1,2} = M_{\mathrm{s}1,2}\mathbf{m}_{1,2}$ separated by an spacer s. (b-e) illustrate bilayer (b-c) and trilayer (d-e) configurations with parallel and antiparallel magnetization orientations (indicated by black horizontal arrows), assuming identical M_{s}. Here, only the bilayer with an antiparallel configuration has a toroidal moment. The other cases have $\boldsymbol{\tau}^{\mathrm{v}} = 0$. (f-i) show similar configurations but with nonidentical M_{s} across layers (see color code), showing a finite toroidal moment for both parallel and antiparallel arrangements. In all cases (b–i), the layers have equal thickness.

(FM) coupled with either a paramagnet (PM) or a superconductor (SC) semi-infinite layer. In both cases, the nonreciprocity originates from the dipolar interaction between the FM layer and the PM/SC material, which breaks the symmetry along the normal direction. In the FM/PM case, spin waves induce a dynamic magnetization in the paramagnet, which in turn creates an asymmetric dipolar field that influences SW propagation. Then, the FM/PM bilayer behaves as the graded system presented earlier, where the induced dynamic magnetization in the paramagnet results in a symmetry breaking associated with a toroidal moment perpendicular to the equilibrium magnetization and the interface normal, in agreement with Eq. (3.64). For the

FM/SC system, SWs in the FM induce a superconducting current in the SC, which also creates an asymmetric dipole field that breaks the symmetry. This inhomogeneous field within the ferromagnet can be associated with a toroidal moment parallel to $\hat{n} \times \mathbf{M}$. In Ref. [200], the calculated frequency asymmetry Δf is proportional to $\mathbf{k} \cdot (\hat{n} \times \mathbf{M})$, which agrees with the nonreciprocity condition if $\boldsymbol{\tau} \to \hat{n} \times \mathbf{M}$.

4.5 Magnon nonreciprocity in DMI films

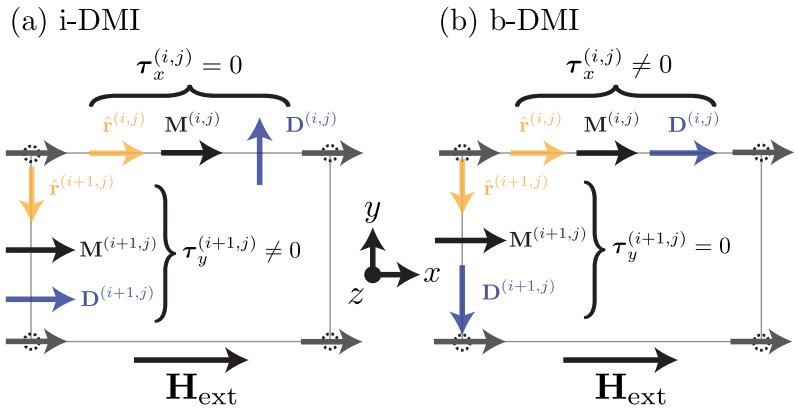

FIGURE 4.8: Bond magnetic toroidal moment for a square crystal lattice with magnetization and applied field parallel to the x-axis for a thin film with (a) interfacial DMI and (b) bulk DMI. The gray arrows at the corners represent the magnetic moment of each site (all oriented in the x-direction), while the yellow arrows depict the bond unit vectors $\hat{\mathbf{r}}^{(i,j)}$ and $\hat{\mathbf{r}}^{(i+1,j)}$ along x and y directions. Then, with the bond vector, the average magnetization, and the DM vector for each pair, the BMTD associated with each configuration can be obtained.

Dzyaloshinskii–Moriya materials may also present a toroidal moment [204]. For interfacial DMI, nonreciprocity is present in flat films for $\mathbf{M} \perp \mathbf{k}$, meanwhile for bulk DMI, nonreciprocity appears for $\mathbf{M} \,||\, \mathbf{k}$ [29, 30, 89]. From microscopic calculations, modulations in the dispersion bands can be expressed through magnetic toroidal bond multipoles linked to anisotropic current distributions in triangular antiferromagnetic lattices [205, 206]. These expressions are useful for predicting or estimating nonreciprocity and transport properties. From such a multipole description for microscopic systems, it is also possible to obtain a toroidal moment associated with the type of DMI, the crystal lattice, and the magnetic configuration [113]. This quantity, referred to as bond magnetic toroidal dipole (BMTD), is a microscopic indicator of DMI-induced nonreciprocity and fulfills the condition $\boldsymbol{\tau} \cdot \mathbf{k} \neq 0$ for asymmetric dispersions. The BMTD is calculated using $\boldsymbol{\tau}^{(ij)} \cdot \hat{\mathbf{r}}^{(ij)} = \mathbf{D}^{(ij)} \cdot \mathbf{M}^{(ij)}$, where $\mathbf{M}^{(ij)}$ is the averaged magnetic moment for the ith and jth spins, $\hat{\mathbf{r}}^{(ij)}$ is the unit vector connecting these spins, and $\boldsymbol{\tau}^{(ij)}$ represents the bond magnetic toroidal dipole on the bond (ij) [113]. Therefore, the BMTD is active if $\mathbf{D}^{(ij)} \cdot \mathbf{M}^{(ij)} \neq 0$ and then, nonreciprocity due to DMI arises for magnons moving parallel to BMTD. For interfacial DMI, it is known that the DM vector ($\mathbf{D}^{(ij)}$) is perpendicular to $\hat{\mathbf{r}}^{(ij)}$ and nonreciprocity appears for $\mathbf{M} \perp \mathbf{k}$, meanwhile for bulk DMI the DM vector is parallel to $\hat{\mathbf{r}}^{(ij)}$, and nonreciprocity can occur for $\mathbf{M} \,||\, \mathbf{k}$, in perfect agreement with well-known results [29, 30, 89]. These two situations are illustrated in Fig. 4.8, where two square lattices are schematized at whose sites there are localized spins in the presence of DMI. These magnetic moments are aligned along the x-axis due to a bias field so that the

average magnetization in each bond points in that direction. In Fig. 4.8(a), interfacial DMI is considered, while in Fig. 4.8(b), bulk DMI is depicted. Thus, in (a) [(b)] the DM vector points perpendicular [parallel] to the vector joining two consecutive sites ($\hat{\mathbf{r}}^{(i,j)}$), representing the condition for an active BMTD to occur on each bond.

Chapter 5

From flat to curvilinear magnetic waveguides

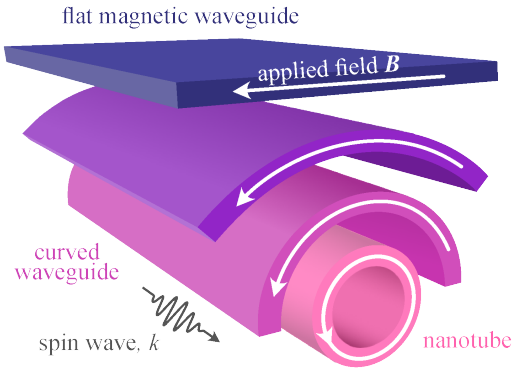

FIGURE 5.1: Schematic representation of a ferromagnetic waveguide undergoing a geometrical transformation from a flat strip (blue) to a fully closed tube (pink).

In this Chapter, the main results of the published article "Curvature-induced parity loss and hybridization of magnons: Exploring the connection of flat and tubular magnetic shells" [80] are presented. Historically, static and dynamic magnetic properties of planar and curved systems have been treated separately, often emphasizing the advantages of one geometry over the other. For instance, curvature-induced anisotropy has been shown to facilitate the propagation of magnons with large group velocities [207], and to enable nonreciprocal phenomena, i.e., $f(\mathbf{k}) \neq f(-\mathbf{k})$ [17, 18]. Moreover, the bending of a nanotube with bulk DMI has been demonstrated to affect texture nucleation, thereby allowing additional equilibrium states and modifying the dynamical response at $k = 0$ [208]. Nevertheless, it is possible to explore the geometrical transition starting from flat waveguides, rolling them up, and ultimately forming a complete tube, as illustrated in Fig. 5.1. For each geometry along this transition, the static and dynamic magnetic properties were computed and analyzed, revealing a strong dependence on the equilibrium magnetization, which can be tuned by the applied external field. Figure 5.2(a) shows the geometric evolution from a flat waveguide to a tubular one as the relative curvature κ_{rel} increases, indicating the relevant dimensions, such as the thickness T, the strip width W, the average radius R_κ and their connection to the definition of κ_{rel}. This relative curvature $0 \leq \kappa_{\text{rel}} \leq 1$ is defined in order to describe any geometry between the flat and the tube shapes, with $\kappa_{\text{rel}} = R_\kappa / R_\circ$, $R_\kappa = W/(2\pi\kappa_{\text{rel}})$ and $R_\circ = W/(2\pi)$, the tube radius. Therefore, $\kappa_{\text{rel}} = 0\,(R_\kappa \to 0)$ refers to the flat waveguide, while $\kappa_{\text{rel}} = 1\,(R_\kappa \to R_\circ)$ to the full tube.

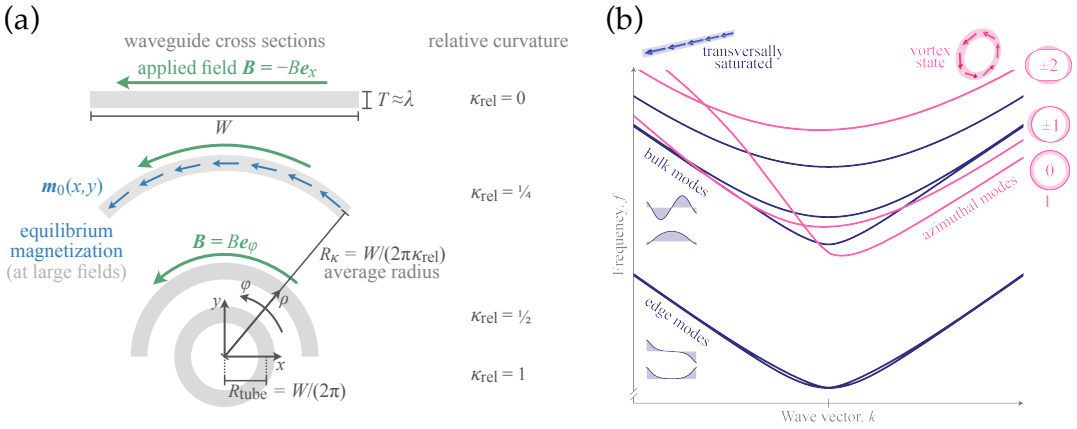

FIGURE 5.2: (a) Schematics describing the waveguides cross-sections from flat to tubular geometries, as a function of the relative curvature κ_{rel}. (b) Spin-wave dispersions for waveguides with flat (blue) and tubular (pink) cross-sections. The equilibrium magnetizations in the cross-section of the flat and tubular waveguides are transversally saturated and vortex-state, respectively. Mode profiles are shown as insets. Figure adapted from Ref. [80].

In the geometries considered here, spin waves propagate along infinite waveguides in the z-axis and cross-sections, as depicted in Fig. 5.2(a) for a rectangular waveguide with a width of $W = 160$ nm, and a thickness of $T = 10$ nm, that is in the order of the dipole-exchange length. When rolling up the waveguide, both the central arc length (W) and thickness (T) are kept constant. The equilibrium magnetization $\mathbf{M}_0(x,y) = M_s\,\mathbf{m}_0(x,y)$, with $\mathbf{m}_0(x,y)$ the unitary equilibrium magnetization, depends on the externally applied magnetic field $\mathbf{B}$, which is oriented transversally. For the rectangular waveguide, this field is parallel to the negative x-direction, while for all the other cases ($\kappa > 0$), it is aligned to the azimuthal direction (ϕ). According to the magnitude of the field, $\mathbf{m}_0(x,y)$ will be saturated transversely, axially, or somewhere in between. The linear magnon spectra in these waveguides are studied by using the finite-element dynamic-matrix method for propagating spin waves implemented in the micromagnetic modeling package TETRAX [209], where it is possible to obtain the angular frequency ω_ν and the unitless complex-valued spatial mode profiles $\mathbf{m}_\nu(\mathbf{r})$ of the νth magnon eigenmode. These solutions are computed by numerically solving the linearized Landau-Lifshitz equation in the vicinity of a stable equilibrium magnetization, using the dynamic-matrix method Ref. [164]. The equilibrium states and magnon spectrum are obtained by considering only the symmetric exchange interaction, dipole-dipole interactions, and the Zeeman energy contribution. Fig. 5.2(b) summarizes the main differences in the spin-wave dispersion between a flat, transversely saturated waveguide and a tube in a vortex state, which can be regarded as its curved counterpart. The contrast is striking: the flat system exhibits a fully reciprocal dispersion, characterized by a doublet of edge modes and an infinite set of nondegenerate bulk modes, whereas the tubular system in the vortex state displays a nonreciprocal dispersion, whose eigenmodes are classified by integer azimuthal indices $l \in \mathbb{Z}$. In the tubular case, modes with opposite azimuthal indices $\pm l$ remain degenerate for a given wavevector k, i.e., $\omega_l(k) = \omega_{-l}(k)$. This is fully consistent with the ideas developed in the previous chapters regarding the toroidal moment: for the tube in the vortex state, a finite toroidal moment parallel to the tube axis is expected, whereas the flat waveguide, with constant saturation magnetization M_s and a spatially uniform magnetization, has a vanishing toroidal

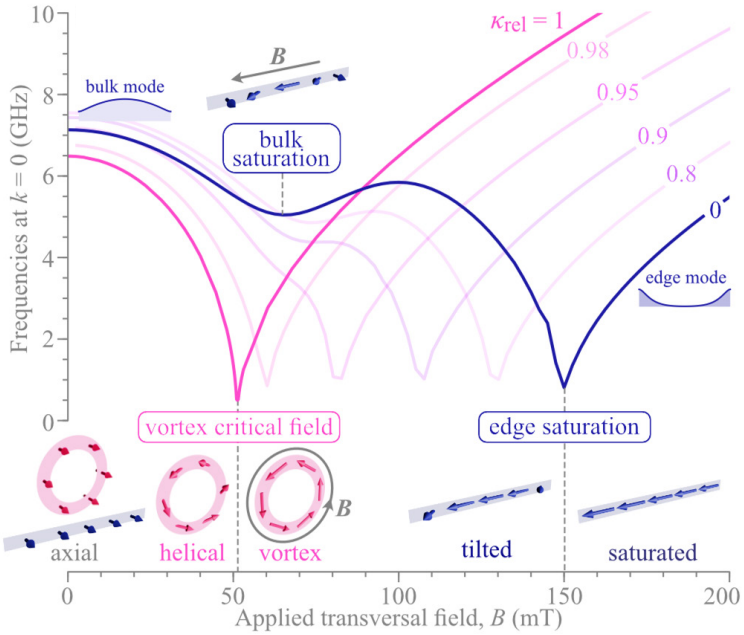

FIGURE 5.3: Ferromagnetic resonance modes and their dependence on the applied transversal field for different κ_{rel} values. Insets show the equilibrium magnetization states for flat (blue) and tubular (pink) waveguides, as well as some bulk and edge modes. Figure adapted from Ref. [80].

moment and thus is not expected to exhibit any nonreciprocal behavior.

The intimate dependence of magnetization on curvature and the applied field can be extracted from the analysis of ferromagnetic resonance modes. This can be seen in Fig. 5.3, where the fundamental-mode frequency as a function of the external field for different values of κ_{rel} is shown. The transition from $\kappa_{\text{rel}} = 0$ (flat) to $\kappa_{\text{rel}} = 1$ (closed tube) is evident at first glance, as the shape of the curves undergoes a gradual shift. At zero field, the magnetization is axially oriented due to the waveguide geometry, as shown in the insets. In the flat case, at zero field, the spin-wave excitations correspond to a symmetrically distributed bulk mode that becomes edge-symmetric as the field increases and the magnetization becomes oriented towards the field. Two minima can be distinguished, denoted here as bulk saturation and edge saturation, which mark the transition from an axial-homogeneous equilibrium state to tilted states (see insets) to ultimately reach the saturated state. As the relative curvature κ_{rel} increases and the flat waveguide is rolled up, the bulk-saturation field partially increases while the edge-saturation field decreases significantly. As the system approaches the tubular geometry, a single sharp minimum emerges, marking the transition between axial, helical/curling, and vortex states.

Another aspect to compare, as the geometry changes and chiral interactions become relevant, is the symmetry of the modes. Magnon modes beyond the fundamental mode can be inhomogeneous in the waveguide cross-section, even at $k = 0$. To study the symmetry of these modes, it is useful to perform a quantification by using the parity with respect to the mirror plane of the cross-section. Based on Ref. [210], the expectation value of the parity operator $\hat{P}$ is

$$P_\nu := \langle \tilde{\boldsymbol{\eta}}_{\nu,k} | \hat{P} | \tilde{\boldsymbol{\eta}}_{\nu,k} \rangle = \int_{\mathrm{A}} \mathrm{d}x\, \mathrm{d}y\, \tilde{\boldsymbol{\eta}}^*_{\nu,k}(x,y) \cdot \tilde{\boldsymbol{\eta}}_{\nu,k}(-x,y), \tag{5.1}$$

where $\tilde{\boldsymbol{\eta}}_{\nu,k}$ is the normalized complex-valued lateral mode profile of the νth mode, obtained from $\mathbf{m}_\nu(\mathbf{r}) = \boldsymbol{\eta}_{\nu,k}(x,y)e^{ikz}$, according to the frame of reference locally orthogonal to the equilibrium magnetization $\mathbf{m}_0$. With this, $-1 \leq P_\nu \leq 1$, and $P_\nu = +1(-1)$, indicate that the modes are even (odd) with respect to the mirror plane, that is, symmetric (antisymmetric) and for $P_\nu \neq 1$ the modes are referred to as heterosymmetric [211], as illustrated in Fig. 5.4(a).

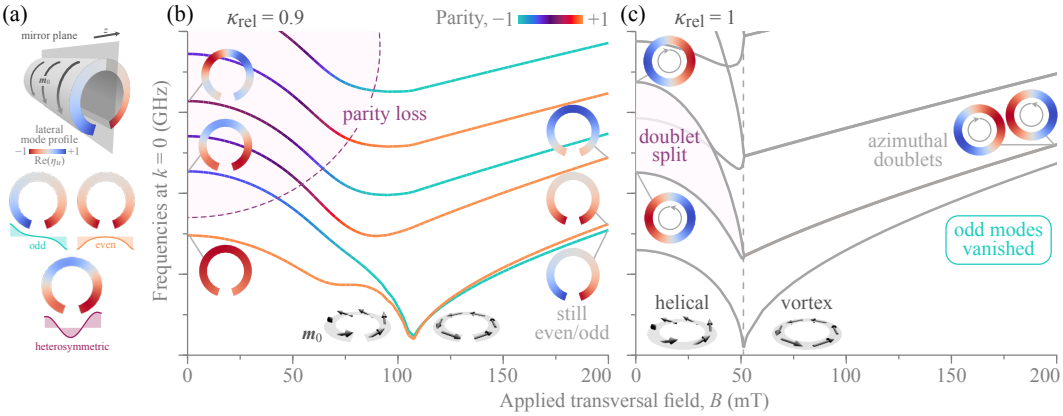

FIGURE 5.4: (a) Illustration of the mirror-plane used to obtain the parity according to the Eq. 5.1 and mode profiles with their respective parity. (b-c) Ferromagnetic resonances for the waveguides with $\kappa_{rel} = 0.9$ and $\kappa_{rel} = 1.0$ for different modes, colored according to parity for (b), meanwhile for (c) the parity is meaningless and modes are gray colored. Insets show the modes profiles and equilibrium states. Figure adapted from Ref. [80].

For the planar case (not shown), the parity is even/odd ($P_\nu = \pm 1$) for each mode and all field values, with alternating parity between them. Notably, as the field increases, the second mode undergoes a transition and degenerates with the first mode at the frequency minimum, thereby forming odd and even edge states. This degeneracy starts to disappear for $\kappa_{rel} = 0.9$ [see Fig. 5.4(b)] for the first two modes. The parity of the modes remains even or odd, although below 110 mT, the higher modes exhibit a loss of parity, as indicated by the blue and purple colors in their spectral lines; these modes are heterosymmetric at these fields. The origin of this heterosymmetry lies in the curvature-induced DMI-like contribution resulting from the exchange interaction [212, 213]. A way to understand this parity loss is to consider higher-order modes as standing waves formed by two counter-propagating components. When symmetry between the $+\phi$ and $-\phi$ directions is broken, these waves have different wavelengths, a symmetric superposition is not allowed, and heterosymmetry emerges. The fundamental mode is unaffected, as it lacks such counter-propagating parts. The curvature-induced DMI only participates as long as $\mathbf{m}_0$ has a nonzero z component (below 110 mT in this case). As $\mathbf{m}_0$ is saturated along ϕ, the modes parity is ± 1. A more detailed discussion is provided in [80]. At large fields, for $\kappa_{rel} \lesssim 1$, it can be seen that the modes are even/odd laterally standing waves. When the loop is closed, and the full tube is formed ($\kappa_{rel} = 1$), the odd modes vanish because they are not allowed by the edgeless boundary condition, representing a discontinuity for the closed case. In contrast, the even modes become doublets. Parity is no longer well-defined for full tubes, and consequently, modes are colored gray.

The connection between flat and tubular waveguides has been established at $k = 0$ through a change in the critical fields and the heterosymmetry of the higher

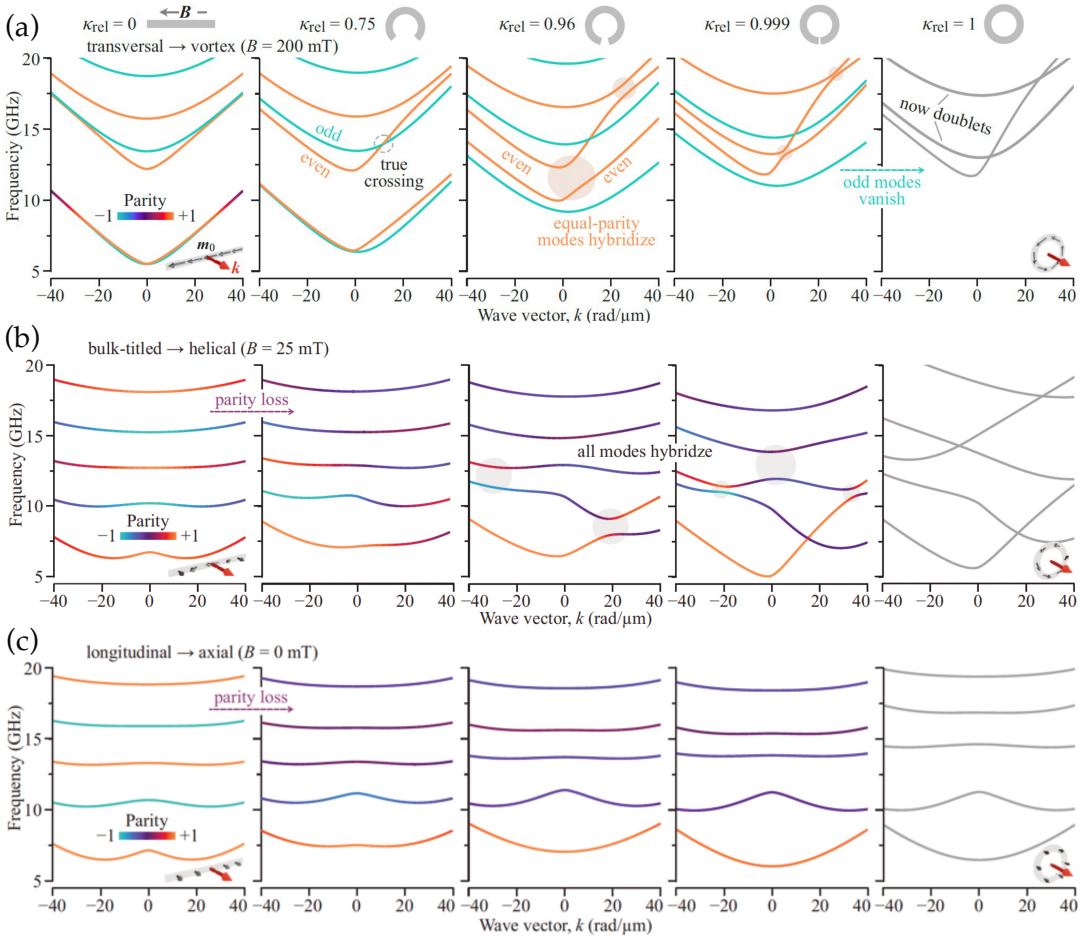

FIGURE 5.5: Spin-wave dispersion relations for three different equilibrium magnetization regimes, as a function of the applied field and for various values of the relative curvature ($\kappa_{\text{rel}} = 0, 0.75, 0.96, 0.999, 1$): (a) evolution from the transverse to the vortex state at $B = 200$ mT, (b) evolution from the bulk-tilted to the global helical state at $B = 25$ mT, and (c) evolution from the longitudinal to the axial state at $B = 0$. Modes are color coded according to their parity, and the insets depict the corresponding equilibrium magnetization configurations. Gray shaded circles indicate anticrossings between different modes.

modes, which strongly depend on the equilibrium states. A similar analysis can be done with the propagating modes with $k \neq 0$, as can be seen in Fig. 5.5. For the $\phi-$saturated state ($x-$ for the flat waveguide) at $B = 200$ mT, the parity is preserved for each geometry with $P_\nu = \pm 1$. The flat waveguide exhibits a fully symmetric dispersion between $f(\mathbf{k})$ and $f(-\mathbf{k})$ with edge modes as the first two modes. As the curvature increases, nonreciprocity induced by dipole-dipole interaction and level crossover between modes arises. However, modes with the same parity do not undergo level crossover, but instead they hybridize, exhibiting level gaps. This hybridization occurs for modes with spatial overlap and is satisfied only for modes of equal parity. As for $k = 0$, when the tube is formed, all odd-parity modes disappear, while the even-parity modes evolve into doublets of counter-propagating azimuthal modes. At $B = 25$ mT, the equilibrium state is no longer saturated and is bulk-tilted for the flat waveguide and helical/curling for the curved cross-sections with

a significant $z-$component. As the curvature increases, so does the nonreciprocity, and the parity loss emerges. The latter leads to hybridization and anticrossings between all modes. For the axial state at zero field, the higher-order modes exhibit heterosymmetry; however, the dispersions are reciprocal for all κ_{rel}, which typically leads to less level crossings in the spectrum. Therefore, hybridization can be absent in these systems. From the perspective of the toroidal moment, and in agreement with the discussion in Section 4.3 for curling magnetization textures, whenever the equilibrium magnetization acquires an azimuthal component, a finite toroidal moment parallel to the tube axis is generated. This is precisely the case for the states at $B = 200$ mT and $B = 25$ mT, for which all spin-wave dispersions are nonreciprocal. In contrast, at $B = 0$ the longitudinal/axial magnetization has no azimuthal component, the toroidal moment vanishes, and the corresponding spin-wave dispersions are fully reciprocal.

Chapter 6

Toroidicity and dynamic effects

In this chapter the dynamical aspects of toroidal order in magnetic media are briefly addressed. First, an equation of motion for the toroidization is derived from the Landau–Lifshitz–Gilbert equation, revealing how toroidal dynamics are coupled to both the magnetization and the monopolar contribution of the magnetoelectric multipole expansion. Second, the influence of a finite toroidal moment on the dispersion of electromagnetic waves is analyzed on the basis of the modified constitutive relations in a toroidal medium, showing how a term proportional to $\boldsymbol{\tau} \cdot \mathbf{k}$ gives rise to direction-dependent attenuation or amplification and, consequently, to nonreciprocal light propagation.

6.1 Toroidization Dynamics

Analogously to the dynamics of magnetization it is possible to obtain an expression for the dynamics of toroidization. We begin with the definition of toroidization,

$$\mathbf{T} = \frac{1}{2}\,\mathbf{r} \times \mathbf{M}, \tag{6.1}$$

and the toroidal moment is,

$$\boldsymbol{\tau} = \int \mathrm{d}V\, \mathbf{T}. \tag{6.2}$$

Deriving $\mathbf{T}$ with respect to time,

$$\frac{\mathrm{d}\mathbf{T}}{\mathrm{d}t} = \frac{1}{2}\,\mathbf{r} \times \frac{\mathrm{d}\mathbf{M}}{\mathrm{d}t} + \frac{1}{2}\,\frac{\mathrm{d}\mathbf{r}}{\mathrm{d}t} \times \mathbf{M}. \tag{6.3}$$

But $\frac{\mathrm{d}\mathbf{r}}{\mathrm{d}t} = 0$ because the spin positions are localized. But $\frac{\mathrm{d}\mathbf{r}}{\mathrm{d}t}$ could be important in magnetoelastic systems or under the effects of temperature because of the vibration of the electronic positions. With this we could have a coupling between the lattice and the magnetization (magnon-phonon coupling) and an additional term would emerge in $\frac{\mathrm{d}\mathbf{T}}{\mathrm{d}t}$. Out of these cases we simply have that,

$$\frac{\mathrm{d}\mathbf{T}}{\mathrm{d}t} = \frac{1}{2}\,\mathbf{r} \times \frac{\mathrm{d}\mathbf{M}}{\mathrm{d}t}. \tag{6.4}$$

On the other hand, the magnetization dynamics is described by the Landau-Lifshitz-Gilbert (LLG) equation,

$$\frac{\mathrm{d}\mathbf{M}}{\mathrm{d}t} = -\gamma_0 \mathbf{M} \times \mathbf{H}_{\mathrm{eff}} + \frac{\alpha}{M_{\mathrm{s}}}\mathbf{M} \times \frac{\mathrm{d}\mathbf{M}}{\mathrm{d}t}, \tag{6.5}$$

and replacing,

$$\begin{aligned}\frac{\mathrm{d}\mathbf{T}}{\mathrm{d}t} &= \frac{1}{2}\,\mathbf{r}\times\left(-\gamma_0\mathbf{M}\times\mathbf{H}_{\mathrm{eff}}+\frac{\alpha}{M_{\mathrm{s}}}\mathbf{M}\times\frac{\mathrm{d}\mathbf{M}}{\mathrm{d}t}\right)\\ &= -\frac{\gamma_0}{2}\mathbf{r}\times(\mathbf{M}\times\mathbf{H}_{\mathrm{eff}})+\frac{\alpha}{2M_{\mathrm{s}}}\mathbf{r}\times\left(\mathbf{M}\times\frac{\mathrm{d}\mathbf{M}}{\mathrm{d}t}\right).\end{aligned} \tag{6.6}$$

By using the the Jacobi's identity,

$$\mathbf{A}\times(\mathbf{B}\times\mathbf{C})+\mathbf{C}\times(\mathbf{A}\times\mathbf{B})+\mathbf{B}\times(\mathbf{C}\times\mathbf{A})=0, \tag{6.7}$$

and replacing in the last equation,

$$\frac{\mathrm{d}\mathbf{T}}{\mathrm{d}t}=\frac{\gamma_0}{2}\left[\mathbf{H}_{\mathrm{eff}}\times(\mathbf{r}\times\mathbf{M})+\mathbf{M}\times(\mathbf{H}_{\mathrm{eff}}\times\mathbf{r})\right]-\frac{\alpha}{2M_{\mathrm{s}}}\left[\frac{\mathrm{d}\mathbf{M}}{\mathrm{d}t}\times(\mathbf{r}\times\mathbf{M})+\mathbf{M}\times\left(\frac{\mathrm{d}\mathbf{M}}{\mathrm{d}t}\times\mathbf{r}\right)\right]. \tag{6.8}$$

It is useful to define,

$$\mathbf{T}_{\mathrm{H}}\equiv\frac{1}{2}\mathbf{r}\times\mathbf{H}_{\mathrm{eff}}, \tag{6.9}$$

which can be regarded as an effective-field torque. By considering the definition for toroidization, the following dynamical equation is obtained:

$$\boxed{\frac{\mathrm{d}\mathbf{T}}{\mathrm{d}t}=\gamma_0\left(\mathbf{H}_{\mathrm{eff}}\times\mathbf{T}-\mathbf{M}\times\mathbf{T}_{\mathrm{H}}\right)+\frac{\alpha}{M_{\mathrm{s}}}\left[\mathbf{M}\times\frac{\mathrm{d}\mathbf{T}}{\mathrm{d}t}-\frac{\mathrm{d}\mathbf{M}}{\mathrm{d}t}\times\mathbf{T}\right]} \tag{6.10}$$

Additionally, by exploiting standard vector identities, one can derive further equivalent expressions, such as

$$\mathbf{M}\times\frac{\mathrm{d}\mathbf{T}}{\mathrm{d}t}=\mathbf{M}\times\left(\frac{1}{2}\mathbf{r}\times\frac{\mathrm{d}\mathbf{M}}{\mathrm{d}t}\right)=\frac{1}{2}\left[\mathbf{r}\left(\mathbf{M}\cdot\frac{\mathrm{d}\mathbf{M}}{\mathrm{d}t}\right)-\frac{\mathrm{d}\mathbf{M}}{\mathrm{d}t}(\mathbf{M}\cdot\mathbf{r})\right], \tag{6.11}$$

Where inserting again the LLG equation,

$$\begin{aligned}\frac{\mathrm{d}\mathbf{T}}{\mathrm{d}t} &= \gamma_0\left(\mathbf{H}_{\mathrm{eff}}\times\mathbf{T}-\mathbf{M}\times\mathbf{T}_{\mathrm{H}}\right)+\frac{\alpha}{M_{\mathrm{s}}}\left[\mathbf{M}\times\frac{\mathrm{d}\mathbf{T}}{\mathrm{d}t}+\mathbf{T}\times\left(-\gamma_0\mathbf{M}\times\mathbf{H}_{\mathrm{eff}}+\frac{\alpha}{M_{\mathrm{s}}}\mathbf{M}\times\frac{\mathrm{d}\mathbf{M}}{\mathrm{d}t}\right)\right]\\ &= \gamma_0\left(\mathbf{H}_{\mathrm{eff}}\times\mathbf{T}-\mathbf{M}\times\mathbf{T}_{\mathrm{H}}\right)+\frac{\alpha}{M_{\mathrm{s}}}\mathbf{M}\times\frac{\mathrm{d}\mathbf{T}}{\mathrm{d}t}-\gamma_0\frac{\alpha}{M_{\mathrm{s}}}\mathbf{T}\times(\mathbf{M}\times\mathbf{H}_{\mathrm{eff}})+\mathcal{O}(\alpha^2),\end{aligned} \tag{6.12}$$

and by using the identity $\mathbf{A}\times(\mathbf{B}\times\mathbf{C})=\mathbf{B}(\mathbf{A}\cdot\mathbf{C})-\mathbf{C}(\mathbf{A}\cdot\mathbf{B})$, we have

$$\begin{aligned}\frac{\mathrm{d}\mathbf{T}}{\mathrm{d}t} &= \gamma_0\left(\mathbf{H}_{\mathrm{eff}}\times\mathbf{T}-\mathbf{M}\times\mathbf{T}_{\mathrm{H}}\right)+\frac{\alpha}{M_{\mathrm{s}}}\mathbf{M}\times\frac{\mathrm{d}\mathbf{T}}{\mathrm{d}t}-\gamma_0\frac{\alpha}{M_{\mathrm{s}}}\left[\mathbf{M}(\mathbf{T}\cdot\mathbf{H}_{\mathrm{eff}})-\mathbf{H}_{\mathrm{eff}}(\mathbf{T}\cdot\mathbf{M})\right]+\mathcal{O}(\alpha^2)\\ &= \gamma_0\left(\mathbf{H}_{\mathrm{eff}}\times\mathbf{T}-\mathbf{M}\times\mathbf{T}_{\mathrm{H}}\right)+\frac{\alpha}{M_{\mathrm{s}}}\mathbf{M}\times\frac{\mathrm{d}\mathbf{T}}{\mathrm{d}t}-\gamma_0\frac{\alpha}{M_{\mathrm{s}}}(\mathbf{T}\cdot\mathbf{H}_{\mathrm{eff}})\mathbf{M}+\mathcal{O}(\alpha^2).\end{aligned} \tag{6.13}$$

On the other hand, by using this last identity instead of the Jacobi's identity in the first treatment,

$$\begin{aligned}\frac{\mathrm{d}\mathbf{T}}{\mathrm{d}t} &= -\frac{\gamma_0}{2}\mathbf{r}\times(\mathbf{M}\times\mathbf{H}_{\mathrm{eff}}) + \frac{\alpha}{2M_{\mathrm{s}}}\mathbf{r}\times\left(\mathbf{M}\times\frac{\mathrm{d}\mathbf{M}}{\mathrm{d}t}\right)\\ &= -\frac{\gamma_0}{2}\left[\mathbf{M}(\mathbf{r}\cdot\mathbf{H}_{\mathrm{eff}}) - \mathbf{H}_{\mathrm{eff}}(\mathbf{r}\cdot\mathbf{M})\right] + \frac{\alpha}{2M_{\mathrm{s}}}\left[\mathbf{M}\frac{\mathrm{d}}{\mathrm{d}t}(\mathbf{r}\cdot\mathbf{M}) - \frac{\mathrm{d}\mathbf{M}}{\mathrm{d}t}(\mathbf{r}\cdot\mathbf{M})\right]. \quad (6.14)\end{aligned}$$

The monopole moment term, which comes from the magnetoelectric multipole expansion, is

$$a = \frac{1}{3}\int \mathrm{d}^3\mathbf{r}\,(\mathbf{r}\cdot\mathbf{M}). \quad (6.15)$$

Then, a density of monopole moment or "monopolization" can be defined as,

$$\tilde{a} = \frac{1}{3}(\mathbf{r}\cdot\mathbf{M}). \quad (6.16)$$

Replacing this term in the last equation for the dynamics of the toroidization,

$$\boxed{\frac{\mathrm{d}\mathbf{T}}{\mathrm{d}t} = -\frac{\gamma_0}{2}\left[\mathbf{M}(\mathbf{r}\cdot\mathbf{H}_{\mathrm{eff}}) - 3\,\mathbf{H}_{\mathrm{eff}}\,\tilde{a}\right] + \frac{3\alpha}{2M_{\mathrm{s}}}\left[\mathbf{M}\frac{\mathrm{d}\tilde{a}}{\mathrm{d}t} - \tilde{a}\frac{\mathrm{d}\mathbf{M}}{\mathrm{d}t}\right]} \quad (6.17)$$

This final expression highlights that the toroidization dynamics are governed not only by the effective field, through the scalar projection $(\mathbf{r}\cdot\mathbf{H}_{\mathrm{eff}})$, but also by the monopolar contribution $\tilde{a}$ and its time evolution. In other words, $\mathbf{T}$ is coupled to both the magnetization precession and the magnetoelectric monopole density, so that any process that drives $\mathbf{M}$ or $\tilde{a}$ out of equilibrium will also induce a dynamical toroidal response. This provides a convenient framework to analyze toroidic relaxation and dissipation, as well as its possible impact on nonreciprocal phenomena in magnetoelectric media.

6.2 Dispersion relation for electromagnetic waves and the toroidal moment

Previous chapters have demonstrated that the toroidal moment is intimately linked to nonreciprocal phenomena in magnonics. In addition, it has been shown that the presence of $\boldsymbol{\tau}$, associated with the magnetoelectric effect, modifies the dispersion of electromagnetic waves in a medium through a contribution proportional to $\boldsymbol{\tau}\cdot\mathbf{k}$ [214], and likewise affects the propagation of surface plasmons in nanowires [215]. Although the existing derivations in the literature are rather limited, it is possible to obtain an explicit expression describing the modification of the dispersion relation of light propagating in a toroidal medium, as will be outlined below. The modified constitutive relations in the presence of a toroidal moment are given by

$$\mathbf{D} = \varepsilon_0\mathbf{E} + \frac{b}{4\pi}(\boldsymbol{\tau}\times\mathbf{H}), \quad (6.18)$$

$$\mathbf{B} = \mu_0\mathbf{H} - \mu_0\frac{b}{4\pi}(\boldsymbol{\tau}\times\mathbf{E}). \quad (6.19)$$

In Fourier space, spatial derivatives are replaced by $i\mathbf{k}$ and time derivatives by $-i\omega$. Consequently, these equations can be written as

$$\mathbf{k} \cdot \mathbf{D} = 0, \quad \mathbf{k} \cdot \mathbf{B} = 0, \tag{6.20}$$

$$\mathbf{k} \times \mathbf{E} = i\omega\mathbf{B}, \quad \mathbf{k} \times \mathbf{H} = -i\omega\mathbf{D}. \tag{6.21}$$

Using the constitutive relations, $\mathbf{D}$ and $\mathbf{B}$ are substituted into Maxwell's equations. In particular, substituting $\mathbf{B}$ into $\mathbf{k} \times \mathbf{E} = i\omega\mathbf{B}$,

$$\mathbf{k} \times \mathbf{E} = i\omega\mu_0\mathbf{H} - i\omega\mu_0\frac{b}{4\pi}(\boldsymbol{\tau} \times \mathbf{E}). \tag{6.22}$$

Analogously for $\mathbf{D}$,

$$\mathbf{k} \times \mathbf{H} = -i\omega\varepsilon_0\mathbf{E} - i\omega\frac{b}{4\pi}(\boldsymbol{\tau} \times \mathbf{H}). \tag{6.23}$$

From these two last equations, it can be obtained that

$$\frac{1}{i\omega\mu_0}\mathbf{k} \times (\mathbf{k} \times \mathbf{E}) + \frac{b}{4\pi}\mathbf{k} \times (\boldsymbol{\tau} \times \mathbf{E}) = -i\omega\varepsilon_0\mathbf{E}. \tag{6.24}$$

Using $\mathbf{k} \times (\mathbf{k} \times \mathbf{E}) = \mathbf{k}(\mathbf{k} \cdot \mathbf{E}) - k^2\mathbf{E}$, the first term becomes,

$$-\frac{k^2}{\omega^2\mu_0}\mathbf{E} + \frac{\mathbf{k}(\mathbf{k} \cdot \mathbf{E})}{\omega^2\mu_0}. \tag{6.25}$$

The second term expands as,

$$\mathbf{k} \times (\boldsymbol{\tau} \times \mathbf{E}) = (\boldsymbol{\tau} \cdot \mathbf{k})\mathbf{E} - (\mathbf{k} \cdot \mathbf{E})\boldsymbol{\tau}. \tag{6.26}$$

Finally,

$$\frac{1}{i\omega\mu_0}\left[\mathbf{k}(\mathbf{k} \cdot \mathbf{E}) - k^2\mathbf{E}\right] + \frac{b}{4\pi}\left[(\boldsymbol{\tau} \cdot \mathbf{k})\mathbf{E} - (\mathbf{k} \cdot \mathbf{E})\boldsymbol{\tau}\right] = -i\omega\epsilon_0\mathbf{E}. \tag{6.27}$$

There is a usual consideration for electromagnetic waves, which is their transverse nature, expressed as $\mathbf{k} \cdot \mathbf{E} = 0$. Under this assumption, the terms $\mathbf{k}(\mathbf{k} \cdot \mathbf{E})$ and $(\mathbf{k} \cdot \mathbf{E})\boldsymbol{\tau}$ vanish, simplifying the equation to:

$$-\frac{k^2}{i\omega\mu_0}\mathbf{E} + \frac{b}{4\pi}(\boldsymbol{\tau} \cdot \mathbf{k})\mathbf{E} = -i\omega\epsilon_0\mathbf{E}. \tag{6.28}$$

Then,

$$\omega^2 + i\frac{\mu_0}{\epsilon_0}\frac{b}{4\pi}(\boldsymbol{\tau} \cdot \mathbf{k})\omega - \frac{k^2}{\mu_0\epsilon_0} = 0 \tag{6.29}$$

This is a quadratic equation in ω of the form:

$$a\omega^2 + b\omega + c = 0, \tag{6.30}$$

whose solution is

$$\omega = -i\frac{\mu_0}{\epsilon_0}\frac{b}{8\pi}(\boldsymbol{\tau}\cdot\mathbf{k}) \pm \frac{1}{2}\sqrt{\frac{4k^2}{\mu_0\epsilon_0} - \left(\frac{\mu_0}{\epsilon_0}\frac{b}{4\pi}(\boldsymbol{\tau}\cdot\mathbf{k})\right)^2}. \tag{6.31}$$

Finally, it is possible to approximate for small $(\boldsymbol{\tau}\cdot\mathbf{k})$. The discriminant simplifies and the solution becomes

$$\boxed{\omega \approx \frac{k}{\sqrt{\mu_0\epsilon_0}} - i\frac{\mu_0}{2\epsilon_0}\frac{b}{4\pi}(\boldsymbol{\tau}\cdot\mathbf{k}),} \tag{6.32}$$

which for the particular case $\boldsymbol{\tau}\cdot\mathbf{k} = 0$, the light dispersion in vacuum is recovered. The presence of an imaginary contribution to the frequency in the dispersion relation implies that the amplitude of the electromagnetic wave is no longer conserved in time. Depending on the sign of $(\boldsymbol{\tau}\cdot\mathbf{k})$, the mode is either attenuated or amplified, leading to direction-dependent or nonreciprocal propagation in the toroidal medium [214].

Conclusions

The central objective of this thesis has been to elucidate the role of the toroidal moment ($\boldsymbol{\tau}$) in micromagnetism and to establish its connection with nonreciprocal spin-wave propagation in a broad class of magnetic systems. The work combines analytical theory and micromagnetic modelling to formulate the different toroidal moments in terms of continuous magnetization textures, quantify their volume and surface contributions, and connect them to asymmetric magnon dispersion relations. A first achievement of this thesis is the development of a consistent micromagnetic description of the toroidal moment. Starting from current density based definitions and the multipole expansion, the toroidal moment is rewritten in terms of the magnetization field and separated into volume and surface contributions for confined structures. This approach shows how boundaries, geometry, and commensuration contribute to the toroidal moment, and how the choice of origin modifies its value in finite systems, where the commensurate part must be subtracted in practical calculations. Within this framework, the toroidal moment is connected to the antisymmetric part of the dynamic magnetic tensor, providing a direct link between symmetry arguments and measurable spin-wave responses. In particular, the nonreciprocity condition $\boldsymbol{\tau} \cdot \mathbf{k} \neq 0$, with $\mathbf{k}$ the spin-wave wave vector, plays a central role. The formalism is then applied to a variety of magnetic textures and geometries. Analytical expressions for the toroidal moment are obtained for magnetic films under the influence of electric currents, conical–helical textures in thin films and tubes, both in presence of the Dzyaloshinskii–Moriya interaction, for skyrmions, merons and bimerons in confined structures, and for systems with graded saturation magnetization. These case studies show that spatially varying magnetization and gradients in material parameters such as M_s generate finite toroidal moments whose direction is constrained by the underlying symmetry but can be tuned by external fields and geometry. As a big summary, it is found that $\boldsymbol{\tau} \propto \mathbf{m} \times \mathbf{g}$, where $\mathbf{m}$ is the unitary magnetization and $\mathbf{g}$ the direction along which either the magnetization direction changes, or M_s changes.

A second major conclusion is that the toroidal moment provides a framework to predict nonreciprocal magnon transport. Within the linearized Landau–Lifshitz–Gilbert formalism, it is shown that a finite projection $\boldsymbol{\tau} \cdot \mathbf{k}$ between the toroidal moment and the spin-wave wave vector is the natural condition for the appearance of k-odd terms in the dispersion relation and, consequently, for nonreciprocal propagation. This criterion is applied to several distinct physical situations, demonstrating its validity. In films under the influence of an electric current, the toroidal moment is linked to the magnonic Doppler shift and establishes that nonreciprocity arises whenever the current direction has a finite component along the wave vector. In systems with graded magnetization, the asymmetry of the M_s profile and its relation with the magnetization direction, generate a toroidal moment that encodes the breaking symmetry, again leading to dispersion asymmetries consistent with the $\boldsymbol{\tau} \cdot \mathbf{k} \neq 0$ condition. For chiral magnets with interfacial or bulk Dzyaloshinskii–Moriya interaction, the toroidal description recovers the known selection rules for nonreciprocity in terms of the relative orientation between equilibrium magnetization, wave vector, and DMI vector, connecting them to microscopic bond magnetic toroidal dipoles.

A third important conclusion concerns the impact of geometric curvature on the static and dynamic properties of magnetic waveguides. By studying the evolution from flat stripes to closed nanotubes, the presented work demonstrates that curvature acts as a control parameter that continuously connects planar and tubular magnonic systems. This transition is accompanied by curvature-induced modifications of the equilibrium magnetization, changes in the ferromagnetic resonance spectra, and the emergence of heterosymmetric spin-wave modes. The analysis shows that, as curvature increases, dipolar interaction and curvature-induced exchange terms produce nonreciprocal dispersion relations and level hybridization between modes of the same parity, while preserving the symmetry constraints that forbid hybridization between modes of opposite parity in open geometries. These results highlight curvature and geometry as effective means to engineer mode profiles, parity, and nonreciprocity in realistic magnonic conduits. They can be naturally interpreted in terms of the toroidal moment, which is intrinsically tied to both the geometry and the underlying magnetization textures.

Finally, the thesis briefly explores the dynamics of the toroidization and also its implications for electromagnetic wave propagation. By combining the micromagnetic Landau–Lifshitz–Gilbert equation with the definition of the toroidization, an equation of motion formally analogous to the LLG equation is obtained, showing how the toroidization precesses in the effective field, is damped, and couples to the monopolar contribution of the magnetoelectric multipole expansion, conveniently described through a "monopolization" density. In parallel, the propagation of electromagnetic waves in a toroidal medium is analyzed by incorporating toroidal terms into the constitutive relations, leading to a dispersion relation with an imaginary correction proportional to $\boldsymbol{\tau} \cdot \mathbf{k}$. This term gives rise to direction-dependent attenuation or amplification of light, thus extending nonreciprocal behavior from magnonic to optical excitations in toroidal media.

Outlook

The results of this thesis point toward several promising directions for future research:

- **Comparison with calculations and micromagnetic simulations.** The analyses presented here include several predictions that could be quantitatively tested by analytical calculation, numerical implementations, or micromagnetic simulations. In particular, the occurrence of reciprocal or nonreciprocal helimagnons in films and nanotubes stabilized by DMI, as well as the spin-wave properties of films with graded saturation magnetization and different geometries, can be directly examined through numerical calculations.

- **Extension to complex textures.** The toroidal framework developed for ferromagnets can be generalized to antiferromagnets and ferrimagnets, where the analysis of the toroidal moment and the symmetries can play an interesting role in magnetoelectricity. Moreover, three-dimensional topological textures such as hopfions provide fertile ground for exploring toroidal characteristics in fully three-dimensional magnonic systems. Finally, an analysis of the remaining terms in the multipolar expansion, such as the quadrupole q, may also reveal information about symmetry breaking and properties associated with nonreciprocity.

- **Reconfigurable nonreciprocal devices.** From an applied perspective, the identification of toroidal moments as control parameters suggests routes to engineer reconfigurable nonreciprocal elements, such as magnonic crystals where the unit cells have a finite toroidal moment, magnonic diodes, isolators, and circulators, and also by combining electric currents, Dzyaloshinskii–Moriya interaction, curvature and graded magnetization. Integrating such elements into magnonic circuits could contribute to energy-efficient, wave-based information processing architectures.

- **Toroidal order in artificial spin ice.** Artificial spin-ice arrays, i.e., arrays of magnetic nanoblocks arranged in complex patterns, offer a highly tunable platform in which emergent vertex configurations can be naturally classified in terms of toroidal and higher-order multipole moments. Extending the present toroidal formalism to these structures would enable a new description of their spin-wave spectra, including the emergence of nonreciprocity. This, in turn, could guide the design of programmable magnonic metamaterials in which toroidal order is written, erased, and reconfigured by external fields or local switching protocols [114].

In summary, this thesis establishes the toroidal moment as a useful descriptor of symmetry breaking in magnetic media, capable of unifying a wide range of nonreciprocal magnonic phenomena and extending naturally to optical regimes. By bridging multipole concepts, micromagnetism, and magnonics, it lays the groundwork for the systematic use of the toroidal order as a design principle in future magnon-based technologies.

Appendix A

Extended calculations

A.1 Calculation of the Surface Toroidal Moment (τ^s)

The toroidal moment associated with any current proposed by Dubovik and Tugushev [98] is

$$\boldsymbol{\tau} = \frac{1}{10}\int \left[\mathbf{r}(\mathbf{r}\cdot\mathbf{J}) - 2r^2\mathbf{J}\right] \mathrm{d}V. \tag{A.1}$$

In order to investigate the connection between the magnetization ($\mathbf{M}$) and the toroidal moment ($\boldsymbol{\tau}$), consider that a magnetization distribution may create a bound current ($\mathbf{J_b}$), defined as

$$\mathbf{J_b}(\mathbf{r}) = \nabla \times \mathbf{M}, \tag{A.2}$$

and in the absence of free and polarization currents, $\mathbf{J} = \mathbf{J}_\mathrm{b}$. Replacing this expression into the Eq (A.1),

$$\boldsymbol{\tau} = \frac{1}{10}\int \left[\mathbf{r}(\mathbf{r}\cdot(\nabla\times\mathbf{M})) - 2r^2(\nabla\times\mathbf{M})\right] \mathrm{d}V. \tag{A.3}$$

As $\nabla \times \mathbf{r} = 0$, then, the divergence of a cross-product can be written as

$$\nabla\cdot(\mathbf{r}\times\mathbf{M}) = -\mathbf{r}\cdot(\nabla\times\mathbf{M}). \tag{A.4}$$

On the other hand, the curl of the product between a scalar function ψ and a vector function $\mathbf{M}$ can be expanded as

$$\nabla\times(\psi\mathbf{M}) = \psi(\nabla\times\mathbf{M}) + (\nabla\psi)\times\mathbf{M}. \tag{A.5}$$

Considering that $\psi = -2r^2$, the second term in Eq. A.3 gives

$$-2r^2(\nabla\times\mathbf{M}) = -2\nabla\times(r^2\mathbf{M}) + 4\mathbf{r}\times\mathbf{M}, \tag{A.6}$$

then, the toroidal moment becomes

$$\boldsymbol{\tau} = \frac{1}{10}\int \left[\,-\mathbf{r}[\nabla\cdot(\mathbf{r}\times\mathbf{M})] - 2\nabla\times(r^2\mathbf{M}) + 4\mathbf{r}\times\mathbf{M}\right] \mathrm{d}V. \tag{A.7}$$

From vector calculus identities,

$$\int_V \psi\nabla\cdot\mathbf{A}\mathrm{d}V = \oiint_S \psi\mathbf{A}\cdot d\mathbf{S} - \int_V \mathbf{A}\cdot\nabla\psi\,\mathrm{d}V. \tag{A.8}$$

On the other hand, in Cartesian coordinates, it can be considered that,

$$\int \mathbf{r}[\nabla \cdot (\mathbf{r} \times \mathbf{M})]\mathrm{d}V = \hat{r}_i \int r_i[\nabla \cdot (\mathbf{r} \times \mathbf{M})]\mathrm{d}V \tag{A.9}$$

Where $r_i = x, y, z$, and the Einstein notation is used. Considering $\psi = r_i$ and $\mathbf{A} = \mathbf{r} \times \mathbf{M}$, then

$$\int_V r_i \nabla \cdot (\mathbf{r} \times \mathbf{M})\, \mathrm{d}V = \oiint_S r_i (\mathbf{r} \times \mathbf{M}) \cdot d\mathbf{S} - \int_V (\mathbf{r} \times \mathbf{M}) \cdot \nabla r_i \, \mathrm{d}V, \tag{A.10}$$

but we have that $\nabla r_i = \hat{r}_i$, then

$$\int_V r_i \nabla \cdot (\mathbf{r} \times \mathbf{M})\, \mathrm{d}V = \oiint_S r_i (\mathbf{r} \times \mathbf{M}) \cdot d\mathbf{S} - \int_V (\mathbf{r} \times \mathbf{M})_i \, \mathrm{d}V, \tag{A.11}$$

and adding the three components,

$$\hat{r}_i \int_V r_i \nabla \cdot (\mathbf{r} \times \mathbf{M})\, \mathrm{d}V = \hat{r}_i \oiint_S r_i (\mathbf{r} \times \mathbf{M}) \cdot d\mathbf{S} - \int_V (\mathbf{r} \times \mathbf{M})\, \mathrm{d}V. \tag{A.12}$$

Replacing the obtained result into the toroidal moment in Eq. A.7,

$$\boldsymbol{\tau} = -\frac{1}{10} \oiint_S \mathbf{r}[(\mathbf{M} \times \mathbf{n}) \cdot \mathbf{r}]\mathrm{d}S - \frac{2}{5} \int \nabla \times (r^2 \mathbf{M})\, \mathrm{d}V + \frac{1}{2} \int (\mathbf{r} \times \mathbf{M})\, \mathrm{d}V. \tag{A.13}$$

The volume integral of the curl of a function, which can be obtained from the Gauss Theorem, is

$$\int_V \nabla \times \mathcal{G}\, \mathrm{d}V = -\oiint_S \mathcal{G} \times d\mathbf{S}. \tag{A.14}$$

By considering that $\mathcal{G} = r^2 \mathbf{M}$ and $d\mathbf{S} = \mathbf{n}\, dS$ where $\mathbf{n}$ is the unit vector normal to the surface,

$$\boldsymbol{\tau} = -\frac{1}{10} \oiint_S \mathbf{r}[(\mathbf{M} \times \mathbf{n}) \cdot \mathbf{r}]\mathrm{d}S + \frac{1}{5} \oiint_S r^2 (\mathbf{M} \times \mathbf{n})\, \mathrm{d}S + \frac{1}{2} \int \mathbf{r} \times \mathbf{M}\, \mathrm{d}V. \tag{A.15}$$

It follows that $\mathbf{M} \times \mathbf{n}$ corresponds to the bound surface current $\mathbf{K}_b$ [216], and the toroidal moment is

$$\boldsymbol{\tau} = \frac{1}{2} \int_V (\mathbf{r} \times \mathbf{M})\, \mathrm{d}V - \frac{1}{10} \oiint_S \left[\mathbf{r}(\mathbf{r} \cdot \mathbf{K}_b) - 2r^2 \mathbf{K}_b\right]\, \mathrm{d}S. \tag{A.16}$$

Then, the toroidal moment splits into two contributions, $\boldsymbol{\tau} = \boldsymbol{\tau}^{\mathrm{v}} + \boldsymbol{\tau}^{\mathrm{s}}$, where

$$\boldsymbol{\tau}^{\mathrm{v}} = \frac{1}{2} \int_V (\mathbf{r} \times \mathbf{M}) \mathrm{d}V \tag{A.17}$$

is the volume term and the standard expression to evaluate the toroidal moment [33, 150], and

$$\boldsymbol{\tau}^{\mathrm{s}} = -\frac{1}{10} \oiint_S \left[\mathbf{r}(\mathbf{r} \cdot \mathbf{K}_b) - 2r^2 \mathbf{K}_b\right]\, \mathrm{d}S \tag{A.18}$$

is the emergent toroidal moment due to surface-bound current $\mathbf{K}_{\mathrm{b}}$. Notice that $\boldsymbol{\tau}^{\mathrm{s}}$ is analogous to Eq. (A.1) but with a closed surface integral and opposite sign.

A.2 Surface toroidal moment for the conical-helix texture in planar films with arbitrary pitch vector.

Next, the surface toroidal moments for a conical–helical texture in a planar system are presented, where the pitch vector (**q**) is allowed to point along an arbitrary in-plane direction.

$$\boldsymbol{\tau}_x^{\mathrm{s}} = -\frac{M_{\mathrm{s}} d}{3q^3}\sin\theta\sin\psi\Bigg\{\csc\varphi\sin\left(\frac{Lq_y}{2}\right)\Bigg[\sin\left(\frac{Lq_x}{2}\right)\left(q^2\left(2d^2+9L^2\right)-24\csc^2\varphi\right) + 3Lq(\cos 2\varphi+3)\csc\varphi\sec^2\varphi\cos\left(\frac{Lq_x}{2}\right)\Bigg] - 3L^2q^2\sec\varphi\cos\left(\frac{Lq_y}{2}\right)\cos\left(\frac{Lq_x}{2}\right)\Bigg\} \tag{A.19}$$

$$\boldsymbol{\tau}_y^{\mathrm{s}} = \frac{M_{\mathrm{s}} d}{3q^3}\sin\theta\sin\psi\Bigg\{\sec\varphi\sin\left(\frac{Lq_x}{2}\right)\sin\left(\frac{Lq_y}{2}\right)\left[q^2\left(2d^2+9L^2\right)-24\sec^2\varphi\right] + 3Lq\cos\left(\frac{Lq_y}{2}\right)\left[2\sin\left(\frac{Lq_x}{2}\right)\left(\csc^2\varphi+2\sec^2\varphi\right)-Lq\csc\varphi\cos\left(\frac{Lq_x}{2}\right)\right]\Bigg\} \tag{A.20}$$

$$\boldsymbol{\tau}_z^{\mathrm{s}} = -\frac{M_{\mathrm{s}} d}{3q^3}\sin\theta\csc\varphi\cos\psi\Bigg\{\sin\left(\frac{Lq_x}{2}\right)\sin\left(\frac{Lq_y}{2}\right)\left[q^2\left(d^2+12L^2\right)-48\csc^2\varphi+12\sec^2\varphi\right] - 6Lq\sec\varphi\sin\left(\frac{Lq_x}{2}\right)\cos\left(\frac{Lq_y}{2}\right)+24Lq\csc\varphi\cos\left(\frac{Lq_x}{2}\right)\sin\left(\frac{Lq_y}{2}\right)\Bigg\} \tag{A.21}$$

Bibliography

1. G. Finocchio, J. A. C. Incorvia, J. S. Friedman, Q. Yang, A. Giordano, J. Grollier, H. Yang, F. Ciubotaru, A. V. Chumak, A. J. Naeemi, S. D. Cotofana, R. Tomasello, C. Panagopoulos, M. Carpentieri, P. Lin, G. Pan, J. J. Yang, A. Todri-Sanial, G. Boschetto, K. Makasheva, V. K. Sangwan, A. R. Trivedi, M. C. Hersam, K. Y. Camsari, P. L. McMahon, S. Datta, B. Koiller, G. H. Aguilar, G. P. Temporão, D. R. Rodrigues, S. Sunada, K. Everschor-Sitte, K. Tatsumura, H. Goto, V. Puliafito, J. Åkerman, H. Takesue, M. D. Ventra, Y. V. Pershin, S. Mukhopadhyay, K. Roy, I Ting Wang, W. Kang, Y. Zhu, B. K. Kaushik, J. Hasler, S. Ganguly, A. W. Ghosh, W. Levy, V. Roychowdhury & S. Bandyopadhyay. Roadmap for unconventional computing with nanotechnology. *Nano Futures* **8,** 012001. doi:10.1088/2399-1984/ad299a (2024).
2. S. Chen. Data centres will use twice as much energy by 2030 — driven by AI. *Nature.* doi:10.1038/d41586-025-01113-z (2025).
3. A. Hirohata, K. Yamada, Y. Nakatani, I.-L. Prejbeanu, B. Diény, P. Pirro & B. Hillebrands. Review on spintronics: Principles and device applications. *Journal of Magnetism and Magnetic Materials* **509,** 166711. doi:10.1016/j.jmmm.2020.166711 (2020).
4. B. Lenk, H. Ulrichs, F. Garbs & M. Münzenberg. The building blocks of magnonics. *Physics Reports* **507,** 107–136. doi:10.1016/j.physrep.2011.06.003 (2011).
5. V. V. Kruglyak, S. O. Demokritov & D. Grundler. Magnonics. *Journal of Physics D: Applied Physics* **43,** 264001. doi:10.1088/0022-3727/43/26/264001 (2010).
6. S. A. Nikitov, A. R. Safin, D. V. Kalyabin, A. V. Sadovnikov, E. N. Beginin, M. V. Logunov, M. A. Morozova, S. A. Odintsov, S. A. Osokin, A. Y. Sharaevskaya, Y. P. Sharaevsky & A. I. Kirilyuk. Dielectric magnonics: from gigahertz to terahertz. *Physics-Uspekhi* **63,** 945. doi:10.3367/UFNe.2019.07.038609 (2020).
7. B. Flebus. Magnonics in collinear magnetic insulating systems. *Journal of Applied Physics* **129,** 161101. doi:10.1063/5.0047042 (2021).
8. B. Flebus, D. Grundler, B. Rana, Y. Otani, I. Barsukov, A. Barman, G. Gubbiotti, P. Landeros, J. Akerman, U. Ebels, P. Pirro, V. E. Demidov, K. Schultheiss, G. Csaba, Q. Wang, F. Ciubotaru, D. E. Nikonov, P. Che, R. Hertel, T. Ono, D. Afanasiev, J. Mentink, T. Rasing, B. Hillebrands, S. V. Kusminskiy, W. Zhang, C. R. Du, A. Finco, T. van der Sar, Y. K. Luo, Y. Shiota, J. Sklenar, T. Yu & J. Rao. The 2024 magnonics roadmap. *J. Phys. Condens. Matter* **36,** 363501. doi:10.1088/1361-648X/ad399c (2024).
9. M. Cocconcelli, F. Maspero, A. Micelli, A. Toniato, A. Del Giacco, N. Pellizzi, A. E. Plaza, A. Cattoni, M. Madami, R. Silvani, C. Adelmann, A. A. Hamadeh, P. Pirro, S. Tacchi, F. Ciubotaru & R. Bertacco. Standalone Integrated Magnonic Devices. *Advanced Materials,* 2503493. doi:10.1002/adma.202503493 (2025).
10. T. J. Sato & K. Matan. Nonreciprocal Magnons in Noncentrosymmetric Magnets. *Journal of the Physical Society of Japan* **88,** 081007. doi:10.7566/JPSJ.88.081007 (2019).

11. A. Barman, G. Gubbiotti, S Ladak, A. O. Adeyeye, M Krawczyk, J Gräfe, C Adelmann, S Cotofana, A Naeemi, V. I. Vasyuchka, B Hillebrands, S. A. Nikitov, H Yu, D Grundler, A. V. Sadovnikov, A. A. Grachev, S. E. Sheshukova, J.-Y. Duquesne, M Marangolo, G Csaba, W Porod, V. E. Demidov, S Urazhdin, S. O. Demokritov, E Albisetti, D Petti, R Bertacco, H Schultheiss, V. V. Kruglyak, V. D. Poimanov, S Sahoo, J Sinha, H Yang, M Münzenberg, T Moriyama, S Mizukami, P Landeros, R. A. Gallardo, G Carlotti, J.-V. Kim, R. L. Stamps, R. E. Camley, B Rana, Y Otani, W Yu, T Yu, G. E. W. Bauer, C Back, G. S. Uhrig, O. V. Dobrovolskiy, B Budinska, H Qin, S van Dijken, A. V. Chumak, A Khitun, D. E. Nikonov, I. A. Young, B. W. Zingsem & M Winklhofer. The 2021 Magnonics Roadmap. *J. Phys. Condens. Matter* **33,** 413001. doi:10.1088/1361-648X/abec1a (2021).
12. J. Chen, H. Yu & G. Gubbiotti. Unidirectional spin-wave propagation and devices. *J. Phys. D: Appl. Phys.* **55,** 123001. doi:10.1088/1361-6463/ac31f4 (2021).
13. H. Yuan, Y. Cao, A. Kamra, R. A. Duine & P. Yan. Quantum magnonics: When magnon spintronics meets quantum information science. *Physics Reports* **965.** Quantum magnonics: When magnon spintronics meets quantum information science, 1–74. doi:10.1016/j.physrep.2022.03.002 (2022).
14. J. A. Otálora, M. Yan, H. Schultheiss, R. Hertel & A. Kákay. Curvature-Induced Asymmetric Spin-Wave Dispersion. *Phys. Rev. Lett.* **117,** 227203. doi:10.1103/PhysRevLett.117.227203 (2016).
15. D. D. Sheka, O. V. Pylypovskyi, P. Landeros, Y. Gaididei, A. Kákay & D. Makarov. Nonlocal chiral symmetry breaking in curvilinear magnetic shells. *Commun. Phys.* **3,** 128. doi:10.1038/s42005-020-0387-2 (2020).
16. M. M. Salazar-Cardona, L. Körber, H. Schultheiss, K. Lenz, A. Thomas, K. Nielsch, A. Kákay & J. A. Otálora. Nonreciprocity of spin waves in magnetic nanotubes with helical equilibrium magnetization. *Appl. Phys. Lett.* **118,** 262411. doi:10.1063/5.0048692 (2021).
17. R. A. Gallardo, P. Alvarado-Seguel & P. Landeros. High spin-wave asymmetry and emergence of radial standing modes in thick ferromagnetic nanotubes. *Phys. Rev. B* **105,** 104435. doi:10.1103/PhysRevB.105.104435 (2022).
18. L. Körber, R. Verba, J. A. Otálora, V. Kravchuk, J. Lindner, J. Fassbender & A. Kákay. Curvilinear spin-wave dynamics beyond the thin-shell approximation: Magnetic nanotubes as a case study. *Phys. Rev. B* **106,** 014405. doi:10.1103/PhysRevB.106.014405 (2022).
19. R. Gallardo, P. Alvarado-Seguel & P. Landeros. Unidirectional Chiral Magnonics in Cylindrical Synthetic Antiferromagnets. *Phys. Rev. Appl.* **18,** 054044. doi:10.1103/PhysRevApplied.18.054044 (2022).
20. L. Körber. *Spin Waves in Curved Magnetic Shells* Doctoral Thesis (Technische Universität Dresden, 2023). doi:10.25368/2023.131.
21. B. Mimica-Figari, P. Landeros & R. A. Gallardo. Dzyaloshinskii-Moriya interaction and dipole-exchange curvature effects on the spin-wave spectra of magnetic nanotubes. *Phys. Rev. B* **112,** 024421. doi:10.1103/8b55-79md (2025).
22. R. A. Gallardo, P. Alvarado-Seguel, T. Schneider, C. Gonzalez-Fuentes, A. Roldán-Molina, K. Lenz, J. Lindner & P. Landeros. Spin-wave non-reciprocity in magnetization-graded ferromagnetic films. *New J. Phys.* **21,** 033026. doi:10.1088/1367-2630/ab0449 (2019).

23. L. Christienne, J. Jiménez-Bustamante, P. Rovillain, M. Eddrief, Y. Zheng, F. Fortuna, M. Marangolo, M. Madami, R. Gallardo, P. Landeros & S. Tacchi. Nonreciprocal spin-wave propagation in anisotropy-graded iron films prepared by nitrogen implantation. *Phys. Rev. Appl.* **24,** 064040. doi:10.1103/1qrj-gtjb (2025).

24. V. Sluka, T. Schneider, R. A. Gallardo, A. Kákay, M. Weigand, T. Warnatz, R. Mattheis, A. Roldán-Molina, P. Landeros, V. Tiberkevich, A. Slavin, G. Schütz, A. Erbe, A. Deac, J. Lindner, J. Raabe, J. Fassbender & S. Wintz. Emission and propagation of 1D and 2D spin waves with nanoscale wavelengths in anisotropic spin textures. *Nat. Nanotechnol.* **14,** 328–333. doi:10.1038/s41565-019-0383-4 (2019).

25. R. Gallardo, T. Schneider, A. Chaurasiya, A. Oelschlägel, S. Arekapudi, A. Roldán-Molina, R. Hübner, K. Lenz, A. Barman, J. Fassbender, J. Lindner, O. Hellwig & P. Landeros. Reconfigurable Spin-Wave Nonreciprocity Induced by Dipolar Interaction in a Coupled Ferromagnetic Bilayer. *Phys. Rev. Appl.* **12,** 034012. doi:10.1103/PhysRevApplied.12.034012 (2019).

26. E. Albisetti, S. Tacchi, R. Silvani, G. Scaramuzzi, S. Finizio, S. Wintz, C. Rinaldi, M. Cantoni, J. Raabe, G. Carlotti, R. Bertacco, E. Riedo & D. Petti. Optically Inspired Nanomagnonics with Nonreciprocal Spin Waves in Synthetic Antiferromagnets. *Adv. Mater.* **32,** 1906439. doi:10.1002/adma.201906439 (2020).

27. M. Grassi, M. Geilen, D. Louis, M. Mohseni, T. Brächer, M. Hehn, D. Stoeffler, M. Bailleul, P. Pirro & Y. Henry. Slow-Wave-Based Nanomagnonic Diode. *Phys. Rev. Applied* **14,** 024047. doi:10.1103/PhysRevApplied.14.024047 (2020).

28. C. Heins, V. Iurchuk, O. Gladii, L. Körber, A. Kákay, J. Fassbender, K. Schultheiss & H. Schultheiss. Nonreciprocal spin-wave dispersion in magnetic bilayers. *Phys. Rev. B* **111,** 134434. doi:10.1103/PhysRevB.111.134434 (2025).

29. R. A. Gallardo, D. Cortés-Ortuño, R. E. Troncoso & P. Landeros. *Three-Dimensional Magnonics* (ed G. Gubbiotti) 121–160 (Jenny Stanford Publishing, Berlin, Heidelberg, 2019).

30. M. Kuepferling, A. Casiraghi, G. Soares, G. Durin, F. Garcia-Sanchez, L. Chen, C. H. Back, C. H. Marrows, S. Tacchi & G. Carlotti. Measuring interfacial Dzyaloshinskii-Moriya interaction in ultrathin magnetic films. *Rev. Mod. Phys.* **95,** 015003. doi:10.1103/RevModPhys.95.015003 (2023).

31. S.-W. Cheong, D. Talbayev, V. Kiryukhin & A. Saxena. Broken symmetries, non-reciprocity, and multiferroicity. *npj Quantum Mater.* **3,** 19. doi:10.1038/s41535-018-0092-5 (2018).

32. Y. Tokura & N. Nagaosa. Nonreciprocal responses from non-centrosymmetric quantum materials. *Nat. Commun.* **9,** 3740. doi:10.1038/s41467-018-05759-4 (2018).

33. N. A. Spaldin, M. Fiebig & M. Mostovoy. The toroidal moment in condensed-matter physics and its relation to the magnetoelectric effect. *J. Phys. Condens. Matter* **20,** 434203. doi:10.1088/0953-8984/20/43/434203 (2008).

34. H. Yu, O. d'Allivy Kelly, V. Cros, R. Bernard, P. Bortolotti, V. E. Demidov, S. O. Demokritov, A. Anane, A. Fukushima, K. Yakushiji, H. Kubota, S. Yuasa, W. Zinn & A. Fert. Approaching soft X-ray wavelengths in nanomagnet-based microwave technology. *Nature Communications* **7,** 11255. doi:10.1038/ncomms11255 (2016).

35. A. V. Chumak, V. I. Vasyuchka, A. A. Serga & B. Hillebrands. Magnon spintronics. *Nature Physics* **11,** 453–461. doi:10.1038/nphys3347 (2015).

36. Q. Wang, A. V. Chumak & P. Pirro. Inverse-design magnonic devices. *Nature Communications* **12,** 2636. doi:10.1038/s41467-021-22897-4 (2021).

37. D. Petti, S. Tacchi & E. Albisetti. Review on magnonics with engineered spin textures. *Journal of Physics D: Applied Physics* **55,** 293003. doi:10.1088/1361-6463/ac6465 (2022).

38. T. Kampfrath, A. Sell, G. Klatt, A. Pashkin, S. Mährlein, T. Dekorsy, M. Wolf, M. Fiebig, A. Leitenstorfer & R. Huber. Coherent terahertz control of antiferromagnetic spin waves. *Nature Photonics* **5,** 31–34. doi:10.1038/nphoton.2010.259 (2011).

39. F. Heussner, G. Talmelli, M. Geilen, B. Heinz, T. Brächer, T. Meyer, F. Ciubotaru, C. Adelmann, K. Yamamoto, A. A. Serga, B. Hillebrands & P. Pirro. Experimental Realization of a Passive Gigahertz Frequency-Division Demultiplexer for Magnonic Logic Networks. *physica status solidi (RRL) – Rapid Research Letters* **14,** 1900695. doi:10.1002/pssr.201900695 (2020).

40. K. O. Nikolaev, D. Raskhodchikov, J. Bensmann, E. Lomonte, L. Jin, R. Schmidt, J. Kern, S. Michaelis de Vasconcellos, R. Bratschitsch, S. O. Demokritov, W. H. P. Pernice & V. E. Demidov. A spin-wave frequency demultiplexer based on YIG nanowaveguides intersecting at a small angle. *Applied Physics Letters* **124,** 212402. doi:10.1063/5.0203425 (2024).

41. G. Gubbiotti, S. Tacchi, M. Madami, G. Carlotti, Z. Yang, J. Ding, A. O. Adeyeye & M. Kostylev. Collective spin excitations in bicomponent magnonic crystals consisting of bilayer permalloy/Fe nanowires. *Phys. Rev. B* **93,** 184411. doi:10.1103/PhysRevB.93.184411 (2016).

42. S. Tacchi, G. Duerr, J. W. Klos, M. Madami, S. Neusser, G. Gubbiotti, G. Carlotti, M. Krawczyk & D. Grundler. Forbidden Band Gaps in the Spin-Wave Spectrum of a Two-Dimensional Bicomponent Magnonic Crystal. *Phys. Rev. Lett.* **109,** 137202. doi:10.1103/PhysRevLett.109.137202 (2012).

43. H. Yu, G. Duerr, R. Huber, M. Bahr, T. Schwarze, F. Brandl & D. Grundler. Omnidirectional spin-wave nanograting coupler. *Nature Communications* **4,** 2702. doi:10.1038/ncomms3702 (2013).

44. R. A. Gallardo, D. Cortés-Ortuño, T. Schneider, A. Roldán-Molina, F. Ma, R. E. Troncoso, K. Lenz, H. Fangohr, J. Lindner & P. Landeros. Flat Bands, Indirect Gaps, and Unconventional Spin-Wave Behavior Induced by a Periodic Dzyaloshinskii-Moriya Interaction. *Phys. Rev. Lett.* **122,** 067204. doi:10.1103/PhysRevLett.122.067204 (2019).

45. M. Krawczyk & D. Grundler. Review and prospects of magnonic crystals and devices with reprogrammable band structure. *Journal of Physics: Condensed Matter* **26,** 123202. doi:10.1088/0953-8984/26/12/123202 (2014).

46. A. V. Chumak, A. A. Serga & B Hillebrands. Magnonic crystals for data processing. *Journal of Physics D: Applied Physics* **50,** 244001. doi:10.1088/1361-6463/aa6a65 (2017).

47. M. Krawczyk & H. Puszkarski. Plane-wave theory of three-dimensional magnonic crystals. *Phys. Rev. B* **77,** 054437. doi:10.1103/PhysRevB.77.054437 (2008).

48. J. Flores-Farías, R. A. Gallardo, F. Brevis, A. Roldán-Molina, D. Cortés-Ortuño & P. Landeros. Omnidirectional Flat Bands in Chiral Magnonic Crystals. *Scientific Reports* **12,** 17831. doi:10.1038/s41598-022-20539-3 (2022).

49. G Gubbiotti, S Tacchi, M Madami, G Carlotti, A. O. Adeyeye & M Kostylev. Brillouin light scattering studies of planar metallic magnonic crystals. *Journal of Physics D: Applied Physics* **43,** 264003. doi:10.1088/0022-3727/43/26/264003 (2010).

50. S Tacchi, G Gubbiotti, M Madami & G Carlotti. Brillouin light scattering studies of 2D magnonic crystals. *Journal of Physics: Condensed Matter* **29,** 073001. doi:10.1088/1361-648X/29/7/073001 (2016).

51. J. Rychły-Gruszecka, J. Walowski, C. Denker, M. Ferch, M. Albrecht, S. Wintz, J. Rychły, A. Maziewski, J. Fassbender, B. Hillebrands, N. Dadoenkova, E. Dadoenkova, I. Lyubchanskii, S. Demokritov, V. Vasyuchka, A. Chumak & P. Gruszecki. Shaping the spin wave spectra of planar 1D magnonic crystals by the geometrical constraints. *Scientific Reports* **12,** 20678. doi:10.1038/s41598-022-24969-x (2022).

52. S. Tacchi, J. Flores-Farías, D. Petti, F. Brevis, A. Cattoni, G. Scaramuzzi, D. Girardi, D. Cortés-Ortuño, R. A. Gallardo, E. Albisetti, G. Carlotti & P. Landeros. Experimental Observation of Flat Bands in One-Dimensional Chiral Magnonic Crystals. *Nano Letters* **23,** 6776–6783. doi:10.1021/acs.nanolett.2c04215 (2023).

53. F. Wei, Y. Zhou, W. Zhang, Z. Ren, G. Chen, H. Li, G. Han, S. Yan & S. Kang. Flat band structure in chiral magnonic crystals with tunable indirect band gaps. *Phys. Rev. Appl.* **23,** 024023. doi:10.1103/PhysRevApplied.23.024023 (2025).

54. F. Wei, Y. Zhou, W. Zhang, Z. Ren, G. Chen, H. Li, G. Han, S. Yan & S. Kang. Fractal properties and tunable flat band structures in chiral magnonic quasicrystals. *Phys. Rev. B* **112,** 144405. doi:10.1103/ww5w-xgbf (2025).

55. J. Flores-Farías, D. Cortés-Ortuño, F. Brevis, P. Landeros & R. A. Gallardo. Selective nonreciprocal localization of flat magnonic modes induced by a periodic Dzyaloshinskii-Moriya interaction. *Phys. Rev. B* **109,** 054423. doi:10.1103/PhysRevB.109.054423 (2024).

56. J. Flores-Farías, F. Brevis, R. Arias, P. Landeros & R. A. Gallardo. Flat modes in one-dimensional chiral magnonic superlattices. *Phys. Rev. B* **111,** 104438. doi:10.1103/PhysRevB.111.104438 (2025).

57. M. Uchida, Y. Onose, Y. Matsui & Y. Tokura. Real-Space Observation of Helical Spin Order. *Science* **311,** 359–361. doi:10.1126/science.1120639 (2006).

58. A. S. Ahmed, J. Rowland, B. D. Esser, S. R. Dunsiger, D. W. McComb, M. Randeria & R. K. Kawakami. Chiral bobbers and skyrmions in epitaxial FeGe/Si(111) films. *Phys. Rev. Mater.* **2,** 041401. doi:10.1103/PhysRevMaterials.2.041401 (2018).

59. H. Yu, J. Xiao & H. Schultheiss. Magnetic texture based magnonics. *Phys. Rep.* **905,** 1–59. doi:10.1016/j.physrep.2020.12.004 (2021).

60. M. Janoschek, F. Bernlochner, S. Dunsiger, C. Pfleiderer, P. Böni, B. Roessli, P. Link & A. Rosch. Helimagnon bands as universal excitations of chiral magnets. *Phys. Rev. B* **81,** 214436. doi:10.1103/PhysRevB.81.214436 (2010).

61. M. Garst, J. Waizner & D. Grundler. Collective spin excitations of helices and magnetic skyrmions: review and perspectives of magnonics in non-centrosymmetric magnets. *J. Phys. D: Appl. Phys.* **50,** 293002. doi:10.1088/1361-6463/aa7573 (2017).

62. K. Wagner, A. Kákay, K. Schultheiss, A. Henschke, T. Sebastian & H. Schultheiss. Magnetic domain walls as reconfigurable spin-wave nanochannels. *Nature Nanotechnology* **11,** 432–436. doi:10.1038/nnano.2015.339 (2016).

63. O. Wojewoda, T. Hula, L. Flajšman, M. Vaňatka, J. Gloss, J. Holobrádek, M. Staňo, S. Stienen, L. Körber, K. Schultheiss, M. Schmid, H. Schultheiss & M. Urbánek. Propagation of spin waves through a Néel domain wall. *Applied Physics Letters* **117,** 022405. doi:10.1063/5.0013692 (2020).

64. X. Xing, Y. Zhou & H. Braun. Magnetic Skyrmion Tubes as Nonplanar Magnonic Waveguides. *Phys. Rev. Appl.* **13,** 034051. doi:10.1103/PhysRevApplied.13.034051 (2020).

65. M. Kugler, G. Brandl, J. Waizner, M. Janoschek, R. Georgii, A. Bauer, K. Seemann, A. Rosch, C. Pfleiderer, P. Böni & M. Garst. Band Structure of Helimagnons in MnSi Resolved by Inelastic Neutron Scattering. *Phys. Rev. Lett.* **115,** 097203. doi:10.1103/PhysRevLett.115.097203 (2015).

66. N. Ogawa, L. Köhler, M. Garst, S. Toyoda, S. Seki & Y. Tokura. Nonreciprocity of spin waves in the conical helix state. *PNAS* **118,** e2022927118. doi:10.1073/pnas.2022927118 (2021).

67. X. Xu, F.-T. Huang & S.-W. Cheong. Magnetic toroidicity. *J. Phys. Condens. Matter* **36,** 203002. doi:10.1088/1361-648x/ad2426 (2024).

68. M. Haidar & M. Bailleul. Thickness dependence of degree of spin polarization of electrical current in permalloy thin films. *Phys. Rev. B* **88,** 054417. doi:10.1103/PhysRevB.88.054417 (2013).

69. R. Gallardo, M. Weigand, K. Schultheiss, A. Kakay, R. Mattheis, J. Raabe, G. Schütz, A. Deac, J. Lindner & S. Wintz. Coherent Magnons with Giant Nonreciprocity at Nanoscale Wavelengths. *ACS Nano* **18.** PMID: 38314709, 5249–5257. doi:10.1021/acsnano.3c08390 (2024).

70. F. Garcia-Sanchez, P. Borys, R. Soucaille, J.-P. Adam, R. L. Stamps & J.-V. Kim. Narrow Magnonic Waveguides Based on Domain Walls. *Phys. Rev. Lett.* **114,** 247206. doi:10.1103/PhysRevLett.114.247206 (2015).

71. R. Camley. Nonreciprocal surface waves. *Surf. Sci. Rep* **7,** 103–187. doi:10.1016/0167-5729(87)90006-9 (1987).

72. J. Lan, W. Yu, R. Wu & J. Xiao. Spin-Wave Diode. *Phys. Rev. X* **5,** 041049. doi:10.1103/PhysRevX.5.041049 (2015).

73. X. Ge, R. Verba, P. Pirro, A. V. Chumak & Q. Wang. Nanoscaled magnon transistor based on stimulated three-magnon splitting. *Applied Physics Letters* **124,** 122413. doi:10.1063/5.0189619 (2024).

74. J. Cheng, R. Yu, L. Sun, *et al.* A nonvolatile magnon field effect transistor at room temperature. *Nature Communications* **15,** 9314. doi:10.1038/s41467-024-53524-7 (2024).

75. A. V. Chumak, A. A. Serga & B. Hillebrands. Magnon transistor for all-magnon data processing. *Nature Communications* **5,** 4700. doi:10.1038/ncomms5700 (2014).

76. R. Damon & J. Eshbach. Magnetostatic modes of a ferromagnet slab. *J. Phys. Chem. Solids* **19,** 308 –320. doi:https://doi.org/10.1016/0022-3697(61)90041-5 (1961).

77. T. Yu, Z. Luo & G. E. Bauer. Chirality as generalized spin–orbit interaction in spintronics. *Phys. Rep.* **1009,** 1–115. doi:10.1016/j.physrep.2023.01.002 (2023).

78. R. Verba, V. Tiberkevich, E. Bankowski, T. Meitzler, G. Melkov & A. Slavin. Conditions for the spin wave nonreciprocity in an array of dipolarly coupled magnetic nanopillars. *Applied Physics Letters* **103,** 082407. doi:10.1063/1.4819435 (2013).

79. L. Körber, M. Zimmermann, S. Wintz, S. Finizio, M. Kronseder, D. Bougeard, F. Dirnberger, M. Weigand, J. Raabe, J. A. Otálora, H. Schultheiss, E. Josten, J. Lindner, I. Kézsmárki, C. H. Back & A. Kákay. Symmetry and curvature effects on spin waves in vortex-state hexagonal nanotubes. *Phys. Rev. B* **104,** 184429. doi:10.1103/PhysRevB.104.184429 (2021).

80. F. Brevis, P. Landeros, J. Lindner, A. Kákay & L. Körber. Curvature-induced parity loss and hybridization of magnons: Exploring the connection of flat and tubular magnetic shells. *Phys. Rev. B* **110,** 134428. doi:10.1103/PhysRevB.110.134428 (2024).

81. M. Xu, A. J. M. Deenen, H. Guo, P. Morales-Fernández, S. Wintz, E. Zhakina, M. Weigand, C. Donnelly & D. Grundler. Geometry-induced spin chirality in a non-chiral ferromagnet at zero field. *Nature Nanotechnology*. doi:10.1038/s41565-025-02055-3 (2025).

82. A. Fert & P. M. Levy. Role of Anisotropic Exchange Interactions in Determining the Properties of Spin-Glasses. *Phys. Rev. Lett.* **44,** 1538–1541. doi:10.1103/PhysRevLett.44.1538 (1980).

83. A. Crépieux & C. Lacroix. Dzyaloshinsky–Moriya interactions induced by symmetry breaking at a surface. *Journal of Magnetism and Magnetic Materials* **182,** 341–349. doi:10.1016/S0304-8853(97)01044-5 (1998).

84. R. E. Camley & K. L. Livesey. Consequences of the Dzyaloshinskii-Moriya interaction. *Surf. Sci. Rep.* **78,** 100605. doi:10.1016/j.surfrep.2023.100605 (2023).

85. N. Nagaosa & Y. Tokura. Topological properties and dynamics of magnetic skyrmions. *Nature Nanotechnology* **8,** 899–911. doi:10.1038/nnano.2013.243 (2013).

86. A. O. Leonov, Y. Togawa, T. L. Monchesky, A. N. Bogdanov, J. Kishine, Y. Kousaka, M. Miyagawa, T. Koyama, J. Akimitsu, T. Koyama, K. Harada, S. Mori, D. McGrouther, R. Lamb, M. Krajnak, S. McVitie, R. L. Stamps & K. Inoue. Chiral Surface Twists and Skyrmion Stability in Nanolayers of Cubic Helimagnets. *Phys. Rev. Lett.* **117,** 087202. doi:10.1103/PhysRevLett.117.087202 (2016).

87. L. Udvardi & L. Szunyogh. Chiral Asymmetry of the Spin-Wave Spectra in Ultrathin Magnetic Films. *Phys. Rev. Lett.* **102,** 207204. doi:10.1103/PhysRevLett.102.207204 (2009).

88. A. T. Costa, R. B. Muniz, S. Lounis, A. B. Klautau & D. L. Mills. Spin-orbit coupling and spin waves in ultrathin ferromagnets: The spin-wave Rashba effect. *Phys. Rev. B* **82,** 014428. doi:10.1103/PhysRevB.82.014428 (2010).

89. D Cortés-Ortuño & P Landeros. Influence of the Dzyaloshinskii–Moriya interaction on the spin-wave spectra of thin films. *J. Phys. Condens. Matter* **25,** 156001 (2013).

90. L. R. Brewer. Deciphering the structure of DNA toroids. *Integr. Biol.* **3,** 540–547. doi:10.1039/C0IB00128G (2011).

91. J. Xu & J. L. Han. The Huge Magnetic Toroids in the Milky Way Halo. *The Astrophysical Journal* **966,** 240. doi:10.3847/1538-4357/ad3a61 (2024).

92. Tokamaks and stellarators. *Nature* **289,** 625–625. doi:10.1038/289625b0 (1981).

93. ITER Organization. *ITER — the way to new energy* https://www.iter.org/. Accessed: October 20, 2025. 2025.

94. S. Gorbunov, A. Volkov & R. Voronkov. Periodic boundary conditions effects on atomic dynamics analysis. *Computer Physics Communications* **279,** 108454. doi:10.1016/j.cpc.2022.108454 (2022).

95. M. Bianchi, G. Pradisi & A. Sagnotti. Toroidal compactification and symmetry breaking in open-string theories. *Nuclear Physics B* **376,** 365–386. doi:10.1016/0550-3213(92)90129-Y (1992).

96. M. Coli, P. Palazzari & R. Rughi. *The toroidal neural networks 2000 IEEE International Symposium on Circuits and Systems (ISCAS)* **4** (2000), 137–140 vol.4. doi:10.1109/ISCAS.2000.858707.

97. F. Brevis, L. Körber, B. Mimica-Figari, R. Gallardo, A. Kákay & P. Landeros. Toroidal moments in confined nanomagnets and their impact on magnonics. *Phys. Rev. Appl.* **24,** 024058. doi:10.1103/2pzb-n2q2 (2025).

98. V. Dubovik & V. Tugushev. Toroid moments in electrodynamics and solid-state physics. *Phys. Rep.* **187,** 145–202. doi:10.1016/0370-1573(90)90042-z (1990).

99. C. Ederer & N. A. Spaldin. Towards a microscopic theory of toroidal moments in bulk periodic crystals. *Phys. Rev. B* **76,** 214404. doi:10.1103/PhysRevB.76.214404 (2007).

100. S. Toyoda, N. Abe & T. Arima. Nonreciprocal Refraction of Light in a Magnetoelectric Material. *Phys. Rev. Lett.* **123,** 077401. doi:10.1103/PhysRevLett.123.077401 (2019).

101. B. B. Van Aken, J.-P. Rivera, H. Schmid & M. Fiebig. Observation of ferrotoroidic domains. *Nature* **449,** 702–705. doi:10.1038/nature06139 (2007).

102. A. S. Zimmermann, D. Meier & M. Fiebig. Ferroic nature of magnetic toroidal order. *Nat. Commun.* **5,** 4796. doi:10.1038/ncomms5796 (2014).

103. M. Fiebig. Revival of the magnetoelectric effect. *Journal of Physics D: Applied Physics* **38,** R123. doi:10.1088/0022-3727/38/8/R01 (2005).

104. P. Toledano, D. D. Khalyavin & L. C. Chapon. Spontaneous toroidal moment and field-induced magnetotoroidic effects in $Ba_2CoGe_2O_7$. *Phys. Rev. B* **84,** 094421. doi:10.1103/PhysRevB.84.094421 (2011).

105. J. Mund, D. R. Yakovlev, A. N. Poddubny, R. M. Dubrovin, M. Bayer & R. V. Pisarev. Toroidal nonreciprocity of optical second harmonic generation. *Phys. Rev. B* **103,** L180410. doi:10.1103/PhysRevB.103.L180410 (2021).

106. S. Miyahara & N. Furukawa. Nonreciprocal Directional Dichroism and Toroidal-magnons in Helical Magnets. *Journal of the Physical Society of Japan* **81,** 023712. doi:10.1143/JPSJ.81.023712 (2012).

107. D. Szaller, S. Bordács & I. Kézsmárki. Symmetry conditions for nonreciprocal light propagation in magnetic crystals. *Phys. Rev. B* **87,** 014421. doi:10.1103/PhysRevB.87.014421 (2013).

108. X. Luo, D. Obeysekera, C. Won, S. H. Sung, N. Schnitzer, R. Hovden, S.-W. Cheong, J. Yang, K. Sun & L. Zhao. Ultrafast Modulations and Detection of a Ferro-Rotational Charge Density Wave Using Time-Resolved Electric Quadrupole Second Harmonic Generation. *Phys. Rev. Lett.* **127,** 126401. doi:10.1103/PhysRevLett.127.126401 (2021).

109. X. Guo, R. Owen, A. Kaczmarek, X. Fang, C. De, Y. Ahn, W. Hu, N. Agarwal, S. H. Sung, R. Hovden, S.-W. Cheong & L. Zhao. Ferrorotational domain walls revealed by electric quadrupole second harmonic generation microscopy. *Phys. Rev. B* **107,** L180102. doi:10.1103/PhysRevB.107.L180102 (2023).

110. D. A. Kleinman. Theory of Second Harmonic Generation of Light. *Phys. Rev.* **128,** 1761–1775. doi:10.1103/PhysRev.128.1761 (1962).

111. T. Kaelberer, V. A. Fedotov, N. Papasimakis, D. P. Tsai & N. I. Zheludev. Toroidal dipolar response in a metamaterial. *Science* **330,** 1510–1512. doi:10.1126/science.1197172 (2010).

112. F. Foggetti, S.-W. Cheong & S. Artyukhin. Magnetic monopoles and toroidal moments in $LuFeO_3$ and related compounds. *Phys. Rev. B* **100,** 180408. doi:10.1103/PhysRevB.100.180408 (2019).

113. T. Matsumoto & S. Hayami. Nonreciprocal magnon excitations by the Dzyaloshinskii-Moriya interaction on the basis of bond magnetic toroidal multipoles. *Phys. Rev. B* **104,** 134420. doi:10.1103/PhysRevB.104.134420 (2021).

114. J. Lehmann, C. Donnelly, P. M. Derlet, L. J. Heyderman & M. Fiebig. Poling of an artificial magneto-toroidal crystal. *Nat. Nanotechnol.* **14,** 141–144. doi:10.1038/s41565-018-0321-x (2018).

115. N. Talebi, S. Guo & P. A. van Aken. Theory and applications of toroidal moments in electrodynamics: their emergence, characteristics, and technological relevance. *Nanophotonics* **7,** 93–110. doi:10.1515/nanoph-2017-0017 (2017).

116. J. William Fuller Brown. *Micromagnetics* (Interscience Publishers, New York, 1963).

117. A. Aharoni. *Introduction to the Theory of Ferromagnetism* 2nd ed. (Oxford University Press, Oxford, 2000).

118. A. Zangwill. *Modern Electrodynamics* en (Cambridge University Press, Cambridge, England, 2012).

119. *Advanced Magnetic Nanostructures* 1st ed. (eds D. J. Sellmyer & R. Skomski) XIV + 508. doi:10.1007/b101199 (Springer Science+Business Media, New York, NY, 2006).

120. A. A. Thiele. The theory of cylindrical magnetic domains. *The Bell System Technical Journal* **48,** 3287–3335. doi:10.1002/j.1538-7305.1969.tb01747.x (1969).

121. M. Cepeda-Arancibia, F. Brevis, S. J. R. Holt, D. Cortés-Ortuño, H. Fangohr & P. Landeros. Micromagnetics of conical-helix textures in thin films with different kinds of Dzyaloshinskii-Moriya interactions. *npj Computational Materials.* doi:10.1038/s41524-025-01926-6 (2026).

122. A. N. Bogdanov & D. A. Yablonskii. Thermodynamically stable vortices in magnetically ordered crystals. The mixed state of magnets. *Sov. Phys. JETP* **68,** 101–103 (1989).

123. U. K. Rößler, A. N. Bogdanov & C. Pfleiderer. Spontaneous skyrmion ground states in magnetic metals. *Nature* **442,** 797–801. doi:10.1038/nature05056 (2006).

124. C. Ríos-Venegas, F. Brevis, R. A. Gallardo & P. Landeros. Dynamic origin of conical helix magnetization textures stabilized by Dzyaloshinskii-Moriya interaction. *Phys. Rev. B* **105,** 224403. doi:10.1103/PhysRevB.105.224403 (2022).

125. B. Mimiça-Figari, F. Brevis, D. Cortés-Ortuño, R. A. Gallardo & P. Landeros. Asymmetric Reversal and Quantized Helical Modes in Ultrathin Nanotubes with Interfacial Dzyaloshinskii-Moriya Interaction. *unpublished* (2025).

126. I. A. Ado, A. Qaiumzadeh, A. Brataas & M. Titov. Chiral ferromagnetism beyond Lifshitz invariants. *Phys. Rev. B* **101,** 161403. doi:10.1103/PhysRevB.101.161403 (2020).

127. E. J. Torok, A. L. Olson & H. N. Oredson. Transition between Bloch and Néel Walls. *Journal of Applied Physics* **36,** 1394–1399. doi:10.1063/1.1714317 (1965).

128. P. Landeros & A. S. Núñez. Domain wall motion on magnetic nanotubes. *J. Appl. Phys.* **108,** 033917. doi:10.1063/1.3466747 (2010).

129. M. R. Scheinfein, J. Unguris, R. J. Celotta & D. T. Pierce. Influence of the surface on magnetic domain-wall microstructure. *Phys. Rev. Lett.* **63,** 668–671. doi:10.1103/PhysRevLett.63.668 (1989).

130. F. Humphrey & M. Redjdal. Domain wall structure in bulk magnetic materials. *Journal of Magnetism and Magnetic Materials* **133,** 11–15. doi:https://doi.org/10.1016/0304-8853(94)90476-6 (1994).

131. T. Trunk, M. Redjdal, A. Kákay, M. F. Ruane & F. B. Humphrey. Domain wall structure in Permalloy films with decreasing thickness at the Bloch to Néel transition. *Journal of Applied Physics* **89,** 7606–7608. doi:10.1063/1.1355357 (2001).

132. K. J. A. Franke, C. Ophus, A. K. Schmid & C. H. Marrows. Switching between Magnetic Bloch and Néel Domain Walls with Anisotropy Modulations. *Phys. Rev. Lett.* **127,** 127203. doi:10.1103/PhysRevLett.127.127203 (2021).

133. R. Cheng, M. Li, A. Sapkota, A. Rai, A. Pokhrel, T. Mewes, C. Mewes, D. Xiao, M. De Graef & V. Sokalski. Magnetic domain wall skyrmions. *Phys. Rev. B* **99,** 184412. doi:10.1103/PhysRevB.99.184412 (2019).

134. M Kläui, C. A. F. Vaz, L Lopez-Diaz & J. A. C. Bland. Vortex formation in narrow ferromagnetic rings. *Journal of Physics: Condensed Matter* **15,** R985. doi:10.1088/0953-8984/15/21/201 (2003).

135. D Altbir, J Escrig, P Landeros, F. S. Amaral & M Bahiana. Vortex core size in interacting cylindrical nanodot arrays. *Nanotechnology* **18,** 485707. doi:10.1088/0957-4484/18/48/485707 (2007).

136. P. G. Radaelli, J. Radaelli, N. Waterfield-Price & R. D. Johnson. Micromagnetic modeling and imaging of vortex|meron structures in an oxide|metal heterostructure. *Phys. Rev. B* **101,** 144420. doi:10.1103/PhysRevB.101.144420 (2020).

137. C. Heins, J.-V. Kim, L. Körber, J. Fassbender, H. Schultheiss & K. Schultheiss. Benchmarking a magnon-scattering reservoir with modal and temporal multiplexing. *Phys. Rev. Appl.* **23,** 054087. doi:10.1103/PhysRevApplied.23.054087 (2025).

138. A. Fehrmann. *Nonlinear Interaction Between Spin-Waves and the Gyroscopic Vortex Motion for Reservoir Computing* Bachelor's Thesis (Technische Universität Dresden, 2023).

139. S. Mühlbauer, B. Binz, F. Jonietz, C. Pfleiderer, A. Rosch, A. Neubauer, R. Georgii & P. Böni. Skyrmion Lattice in a Chiral Magnet. *Science* **323,** 915–919. doi:10.1126/science.1166767 (2009).

140. J. Rowland, S. Banerjee & M. Randeria. Skyrmions in chiral magnets with Rashba and Dresselhaus spin-orbit coupling. *Phys. Rev. B* **93,** 020404. doi:10.1103/PhysRevB.93.020404 (2016).

141. S. Seki, M. Garst, J. Waizner, R. Takagi, N. D. Khanh, Y. Okamura, K. Kondou, F. Kagawa, Y. Otani & Y. Tokura. Propagation dynamics of spin excitations along skyrmion strings. *Nat. Commun.* **11,** 256. doi:10.1038/s41467-019-14095-0 (2020).

142. M. N. Wilson, A. B. Butenko, A. N. Bogdanov & T. L. Monchesky. Chiral skyrmions in cubic helimagnet films: The role of uniaxial anisotropy. *Phys. Rev. B* **89,** 094411. doi:10.1103/PhysRevB.89.094411 (2014).

143. X. S. Wang, H. Y. Yuan & X. R. Wang. A theory on skyrmion size. *Communications Physics* **1,** 31. doi:10.1038/s42005-018-0029-0 (2018).

144. L. Flacke, V. Ahrens, S. Mendisch, L. Körber, T. Böttcher, E. Meidinger, M. Yaqoob, M. Müller, L. Liensberger, A. Kákay, M. Becherer, P. Pirro, M. Althammer, S. Geprägs, H. Huebl, R. Gross & M. Weiler. Robust formation of nanoscale magnetic skyrmions in easy-plane anisotropy thin film multilayers with low damping. *Phys. Rev. B* **104,** L100417. doi:10.1103/PhysRevB.104.L100417 (2021).

145. M. Beg, M. Albert, M.-A. Bisotti, D. Cortés-Ortuño, W. Wang, R. Carey, M. Vousden, O. Hovorka, C. Ciccarelli, C. S. Spencer, C. H. Marrows & H. Fangohr. Dynamics of skyrmionic states in confined helimagnetic nanostructures. *Phys. Rev. B* **95,** 014433. doi:10.1103/PhysRevB.95.014433 (2017).

146. J. C. Bellizotti Souza, N. P. Vizarim, C. J. O. Reichhardt, C Reichhardt & P. A. Venegas. Skyrmionium dynamics and stability on one dimensional anisotropy patterns. *Journal of Physics: Condensed Matter* **37,** 195802. doi:10.1088/1361-648X/adc648 (2025).

147. B. Göbel, A. Mook, J. Henk, I. Mertig & O. A. Tretiakov. Magnetic bimerons as skyrmion analogues in in-plane magnets. *Phys. Rev. B* **99,** 060407. doi:10.1103/PhysRevB.99.060407 (2019).

148. A. A. Kovalev & S. Sandhoefner. Skyrmions and Antiskyrmions in Quasi-Two-Dimensional Magnets. *Frontiers in Physics* **Volume 6 - 2018.** doi:10.3389/fphy.2018.00098 (2018).

149. M. Hassan, S. Koraltan, A. Ullrich, F. Bruckner, R. O. Serha, K. V. Levchenko, G. Varvaro, N. S. Kiselev, M. Heigl, C. Abert, D. Suess & M. Albrecht. Dipolar skyrmions and antiskyrmions of arbitrary topological charge at room temperature. *Nature Physics* **20,** 615–622. doi:10.1038/s41567-023-02358-z (2024).

150. S. Bhowal & N. A. Spaldin. Magnetoelectric Classification of Skyrmions. *Phys. Rev. Lett.* **128,** 227204. doi:10.1103/PhysRevLett.128.227204 (2022).

151. P. Sutcliffe. Hopfions in chiral magnets. *Journal of Physics A: Mathematical and Theoretical* **51,** 375401. doi:10.1088/1751-8121/aad521 (2018).

152. F. Zheng, N. S. Kiselev, F. N. Rybakov, L. Yang, W. Shi, S. Blügel & R. E. Dunin-Borkowski. Hopfion rings in a cubic chiral magnet. *Nature* **623,** 718–723. doi:10.1038/s41586-023-06658-5 (2023).

153. P. Landeros, J. A. Otálora, R. Streubel & A. Kákay. *Curvilinear Micromagnetism: From Fundamentals to Applications* (eds D. Makarov & D. D. Sheka) 163–213 (Springer International Publishing, Cham, 2022). doi:10.1007/978-3-031-09086-8_4.

154. P. Landeros, O. J. Suarez, A. Cuchillo & P. Vargas. Equilibrium states and vortex domain wall nucleation in ferromagnetic nanotubes. *Phys. Rev. B* **79,** 024404. doi:10.1103/PhysRevB.79.024404 (2009).

155. A. Buchter, J. Nagel, D. Rüffer, F. Xue, D. P. Weber, O. F. Kieler, T. Weimann, J. Kohlmann, A. B. Zorin, E. Russo-Averchi, R. Huber, P. Berberich, A. Fontcuberta i Morral, M. Kemmler, R. Kleiner, D. Koelle, D. Grundler & M. Poggio. Reversal Mechanism of an Individual Ni Nanotube Simultaneously Studied by Torque and SQUID Magnetometry. *Phys. Rev. Lett.* **111,** 067202. doi:10.1103/PhysRevLett.111.067202 (2013).

156. A. Mehlin, B. Gross, M. Wyss, T. Schefer, G. Tütüncüoglu, F. Heimbach, A. Fontcuberta i Morral, D. Grundler & M. Poggio. Observation of end-vortex nucleation in individual ferromagnetic nanotubes. *Phys. Rev. B* **97,** 134422. doi:10.1103/PhysRevB.97.134422 (2018).

157. L. Landau, E. Lifshitz, *et al.* On the theory of the dispersion of magnetic permeability in ferromagnetic bodies. *Phys. Z. Sowjetunion* **8,** 101–114 (1935).

158. T. L. Gilbert. A Lagrangian formulation of the gyromagnetic equation of the magnetic field. *Physical Review* **100,** 1243 (1955).

159. T. L. Gilbert. A phenomenological theory of damping in ferromagnetic materials. *IEEE Transactions on Magnetics* **40,** 3443–3449. doi:10.1109/TMAG.2004.836740 (2004).

160. B. A. Kalinikos & A. N. Slavin. Theory of dipole-exchange spin wave spectrum for ferromagnetic films with mixed exchange boundary conditions. *Journal of Physics C: Solid State Physics* **19,** 7013. doi:10.1088/0022-3719/19/35/014 (1986).

161. A. Mahmoud, F. Ciubotaru, F. Vanderveken, A. V. Chumak, S. Hamdioui, C. Adelmann & S. Cotofana. Introduction to spin wave computing. *Journal of Applied Physics* **128,** 161101. doi:10.1063/5.0019328 (2020).

162. A. G. Gurevich & G. A. Melkov. *Magnetization Oscillations and Waves* 1st, 456 (CRC Press, Boca Raton, FL, 1996).

163. I. D. Mayergoyz, G. Bertotti & C. Serpico. *Nonlinear Magnetization Dynamics in Nanosystems* 1st (Elsevier, Amsterdam, 2009).

164. L Körber, G Quasebarth, A Otto & A Kákay. Finite-element dynamic-matrix approach for spin-wave dispersions in magnonic waveguides with arbitrary cross section. en. *AIP Adv.* **11,** 095006. doi:10.1063/5.0054169 (2021).

165. M. J. Donahue & D. G. Porter. *OOMMF User's Guide, Version 1.0* http://math.nist.gov/oommf/. National Institute of Standards and Technology (Gaithersburg, MD, 1999).

166. A. Vansteenkiste, J. Leliaert, M. Dvornik, M. Helsen, F. Garcia-Sanchez & B. Van Waeyenberge. The design and verification of Mumax3. *AIP Advances* **4,** 107133. doi:10.1063/1.4899186 (2014).

167. M.-A. Bisotti, M. Beg, W. Wang, M. Albert, D. Chernyshenko, D. Cortés-Ortuño, R. A. Pepper, M. Vousden, R. Carey, H. Fuchs, A. Johansen, G. Balaban, L. Breth, T. Kluyver & H. Fangohr. *FinMag: finite-element micromagnetic simulation tool* Github https://github.com/fangohr/finmag. Version 0.1. 2018. doi:10.5281/zenodo.1216011.

168. S.-W. Cheong & X. Xu. Magnetic chirality. *npj Quantum Mater.* **7,** 40. doi:10.1038/s41535-022-00447-5 (2022).

169. D. Cortés-Ortuño, N. Romming, M. Beg, K. von Bergmann, A. Kubetzka, O. Hovorka, H. Fangohr & R. Wiesendanger. Nanoscale magnetic skyrmions and target states in confined geometries. *Phys. Rev. B* **99,** 214408. doi:10.1103/PhysRevB.99.214408 (2019).

170. M. Yan, C. Andreas, A. Kákay, F. García-Sánchez & R. Hertel. Fast domain wall dynamics in magnetic nanotubes: Suppression of Walker breakdown and Cherenkov-like spin wave emission. *Applied Physics Letters* **99,** 122505. doi:10.1063/1.3643037 (2011).

171. P. Borys, O. Kolokoltsev, N. Qureshi, M. L. Plumer & T. L. Monchesky. Unidirectional spin wave propagation due to a saturation magnetization gradient. *Phys. Rev. B* **103,** 144411. doi:10.1103/PhysRevB.103.144411 (2021).

172. R. Birss. *Symmetry and Magnetism* (North-Holland Publishing Company, 1964).

173. L. Ding, X. Xu, H. O. Jeschke, X. Bai, E. Feng, A. S. Alemayehu, J. Kim, F.-T. Huang, Q. Zhang, X. Ding, N. Harrison, V. Zapf, D. Khomskii, I. I. Mazin, S.-W. Cheong & H. Cao. Field-tunable toroidal moment in a chiral-lattice magnet. *Nat. Commun.* **12,** 5339. doi:10.1038/s41467-021-25657-6 (2021).

174. F. Thöle, A. Keliri & N. A. Spaldin. Concepts from the linear magnetoelectric effect that might be useful for antiferromagnetic spintronics. *J. Appl. Phys.* **127,** 213905. doi:10.1063/5.0006071 (2020).

175. J. Fernández-Rossier, M. Braun, A. S. Núñez & A. H. MacDonald. Influence of a uniform current on collective magnetization dynamics in a ferromagnetic metal. *Phys. Rev. B* **69,** 174412. doi:10.1103/PhysRevB.69.174412 (2004).

176. V. Vlaminck & M. Bailleul. Current-Induced Spin-Wave Doppler Shift. *Science* **322,** 410–413. doi:10.1126/science.1162843 (2008).

177. L. Körber & A. Kákay. Numerical reverse engineering of general spin-wave dispersions: Bridge between numerics and analytics using a dynamic-matrix approach. *Phys. Rev. B* **104,** 174414. doi:10.1103/PhysRevB.104.174414 (2021).

178. N. A. Spaldin, M. Fechner, E. Bousquet, A. Balatsky & L. Nordström. Monopole-based formalism for the diagonal magnetoelectric response. *Phys. Rev. B* **88.** doi:10.1103/physrevb.88.094429 (2013).

179. A. Aharoni. Demagnetizing factors for rectangular ferromagnetic prisms. *Journal of Applied Physics* **83,** 3432–3434. doi:10.1063/1.367113 (1998).

180. R. Takagi, J. S. White, S. Hayami, R. Arita, D. Honecker, H. M. Rønnow, Y. Tokura & S. Seki. Multiple-q noncollinear magnetism in an itinerant hexagonal magnet. *Sci. Adv.* **4,** eaau3402. doi:10.1126/sciadv.aau3402 (2018).

181. Y. Fujishiro, N. Kanazawa, T. Nakajima, X. Z. Yu, K. Ohishi, Y. Kawamura, K. Kakurai, T. Arima, H. Mitamura, A. Miyake, K. Akiba, M. Tokunaga, A. Matsuo, K. Kindo, T. Koretsune, R. Arita & Y. Tokura. Topological transitions among skyrmion- and hedgehog-lattice states in cubic chiral magnets. *Nat. Commun.* **10,** 1059. doi:10.1038/s41467-019-08985-6 (2019).

182. S. Hayami. Multiple-Q magnetism by anisotropic bilinear-biquadratic interactions in momentum space. *J. Magn. Magn. Mater.* **513,** 167181. doi:10.1016/j.jmmm.2020.167181 (2020).

183. K. V. Yershov, V. P. Kravchuk, D. D. Sheka & U. K. Rößler. Curvature effects on phase transitions in chiral magnets. *SciPost Phys.* **9,** 043. doi:10.21468/SciPostPhys.9.4.043 (2020).

184. W. L. Gan, M. Chandra Sekhar, D. W. Wong, I. Purnama, S. Y. Chiam, L. M. Wong & W. S. Lew. Multi-vortex states in magnetic nanoparticles. *Applied Physics Letters* **105,** 152405. doi:10.1063/1.4898349 (2014).

185. R. Streubel, P. Fischer, F. Kronast, V. P. Kravchuk, D. D. Sheka, Y. Gaididei, O. G. Schmidt & D. Makarov. Magnetism in curved geometries. *J. Phys. D: Appl. Phys.* **49,** 363001. doi:10.1088/0022-3727/49/36/363001 (2016).

186. P. Lederer & D. L. Mills. Possible Experimental Test of the Band Theory of Magnetism. *Phys. Rev.* **148,** 542–547. doi:10.1103/PhysRev.148.542 (1966).

187. M. Zhu, C. L. Dennis & R. D. McMichael. Temperature dependence of magnetization drift velocity and current polarization in $Ni_{80}Fe_{20}$ by spin-wave Doppler measurements. *Phys. Rev. B* **81,** 140407. doi:10.1103/PhysRevB.81.140407 (2010).

188. R. A. Gallardo, J. Flores-Farias, D. Cortés-Ortuño & P. Landeros. Nonreciprocal spin waves induced by the combined action of the Dzyaloshinskii-Moriya interaction and spin-transfer torques. *Unpublished* (2025).

189. X. Yu, M. Mostovoy, Y. Tokunaga, W. Zhang, K. Kimoto, Y. Matsui, Y. Kaneko, N. Nagaosa & Y. Tokura. Magnetic stripes and skyrmions with helicity reversals. *PNAS* **109,** 8856–8860. doi:10.1073/pnas.1118496109 (2012).

190. T. Schwarze, J. Waizner, M. Garst, A. Bauer, I. Stasinopoulos, H. Berger, C. Pfleiderer & D. Grundler. Universal helimagnon and skyrmion excitations in metallic, semiconducting and insulating chiral magnets. *Nat. Mater.* **14,** 478 EP – (2015).

191. M. Weiler, A. Aqeel, M. Mostovoy, A. Leonov, S. Geprägs, R. Gross, H. Huebl, T. T. M. Palstra & S. T. B. Goennenwein. Helimagnon Resonances in an Intrinsic Chiral Magnonic Crystal. *Phys. Rev. Lett.* **119,** 237204. doi:10.1103/PhysRevLett.119.237204 (2017).

192. B. Göbel, A. Mook, J. Henk & I. Mertig. Magnetoelectric effect and orbital magnetization in skyrmion crystals: Detection and characterization of skyrmions. *Phys. Rev. B* **99,** 060406. doi:10.1103/PhysRevB.99.060406 (2019).

193. F. N. Rybakov, N. S. Kiselev, A. B. Borisov, L. Döring, C. Melcher & S. Blügel. Magnetic hopfions in solids. *APL Mater.* **10,** 111113. doi:10.1063/5.0099942 (2022).

194. C. Saji, R. E. Troncoso, V. L. Carvalho-Santos, D. Altbir & A. S. Nunez. Hopfion-Driven Magnonic Hall Effect and Magnonic Focusing. *Phys. Rev. Lett.* **131,** 166702. doi:10.1103/PhysRevLett.131.166702 (2023).

195. M. Jiang, G. Xu, L. Sun, H. Niu, C. Li, X. Yang, T. Ji, M. Yang, J. Cheng, J. Ma, G. Chen, G. Chai, B. Miao & H. Ding. Realizing nonreciprocal spin-wave propagation with large tunability in SmCo/Fe bilayers. *Phys. Rev. B* **112,** L020409. doi:10.1103/l93m-gb54 (2025).

196. P. Micaletti, A. Roxburgh, E. Iacocca, M. Marzolla & F. Montoncello. A sinusoidal magnetization distribution as an original way to generate a versatile magnonic crystal for magnon propagation. *Journal of Magnetism and Magnetic Materials* **622,** 172959. doi:10.1016/j.jmmm.2025.172959 (2025).

197. K. R. Vignesh, A. Soncini, S. K. Langley, W. Wernsdorfer, K. S. Murray & G. Rajaraman. Ferrotoroidic ground state in a heterometallic {CrIIIDyIII6} complex displaying slow magnetic relaxation. *Nature Communications* **8,** 1023. doi:10.1038/s41467-017-01102-5 (2017).

198. W.-C. Yue, Z. Yuan, P. Huang, Y. Sun, T. Gao, Y.-Y. Lyu, X. Tu, S. Dong, L. He, Y. Dong, X. Cao, L. Kang, H. Wang, P. Wu, C. Nisoli & Y.-L. Wang. Toroidic phase transitions in a direct-kagome artificial spin ice. *Nature Nanotechnology* **19,** 1101–1107. doi:10.1038/s41565-024-01666-6 (2024).

199. C. Rodríguez-Gallo, A. Ortiz-Ambriz, C. Nisoli & P. Tierno. Ice rule breakdown and frustrated antiferrotoroidicity in an artificial colloidal Cairo ice. *New Journal of Physics* **25,** 103007. doi:10.1088/1367-2630/acfc60 (2023).

200. M. A. Kuznetsov & A. A. Fraerman. Temperature-sensitive spin-wave nonreciprocity induced by interlayer dipolar coupling in ferromagnet/paramagnet and ferromagnet/superconductor hybrid systems. *Phys. Rev. B* **105,** 214401. doi:10.1103/PhysRevB.105.214401 (2022).

201. R. A. Gallardo, P. Alvarado-Seguel, F. Brevis, A. Roldán-Molina, K. Lenz, J. Lindner & P. Landeros. Spin-Wave Channeling in Magnetization-Graded Nanostrips. *Nanomaterials* **12,** 2785. doi:10.3390/nano12162785 (2022).

202. L. Körber, G. Quasebarth, A. Hempel, F. Zahn, A. Otto, E. Westphal, R. Hertel & A. Kakay. *TetraX: Finite-Element Micromagnetic-Modeling Package* 2022. doi:10.14278/rodare.1418.

203. M. Mruczkiewicz, P. Graczyk, P. Lupo, A. Adeyeye, G. Gubbiotti & M. Krawczyk. Spin-wave nonreciprocity and magnonic band structure in a thin permalloy film induced by dynamical coupling with an array of Ni stripes. *Phys. Rev. B* **96,** 104411. doi:10.1103/PhysRevB.96.104411 (2017).

204. L. Tan, G. Ma, S. Zheng, M. Liu, J. Min, J. Zhang, Y. Li, Y. Xie, Z. Ma, Y. Zhang, L. Lin, X. Wang, H. Li, S. Dong & J.-M. Liu. Possible role of toroidal moments and Dzyaloshinskii-Moriya interaction in the magnetoelectric effect of the hyperkagome compound $Mn_3Al_2Ge_3O_{12}$. *Phys. Rev. B* **110,** 245116. doi:10.1103/PhysRevB.110.245116 (2024).

205. S. Hayami, Y. Yanagi & H. Kusunose. Spontaneous antisymmetric spin splitting in noncollinear antiferromagnets without spin-orbit coupling. *Phys. Rev. B* **101,** 220403. doi:10.1103/PhysRevB.101.220403 (2020).

206. S. Hayami, Y. Yanagi & H. Kusunose. Bottom-up design of spin-split and reshaped electronic band structures in antiferromagnets without spin-orbit coupling: Procedure on the basis of augmented multipoles. *Phys. Rev. B* **102,** 144441. doi:10.1103/PhysRevB.102.144441 (2020).

207. I. Turčan, L. Flajšman, O. Wojewoda, V. Roučka, O. Man & M. Urbánek. Spin Wave Propagation in Corrugated Waveguides. *Applied Physics Letters* **118,** 092405. doi:10.1063/5.0041138 (2021).

208. M.-A. Garrido-Tamayo, E. Saavedra, C. Saji, U. Guevara, L. M. Pérez, L. Pedraja-Rejas, P. Díaz & D. Laroze. Stability and Spin Waves of Skyrmion Tubes in Curved FeGe Nanowires. *Nanomaterials* **14.** doi:10.3390/nano14181468 (2024).

209. L. Körber, G. Quasebarth, A. Hempel, F. Zahn, A. Otto, E. Westphal, R. Hertel & A. Kakay. *TetraX: Finite-Element Micromagnetic-Modeling Package* 2022. doi:10.14278/rodare.1418.

210. C. Trevillian & V. Tyberkevych. Formation of chirality in propagating spin waves. *npj Spintronics* **2,** 23. doi:10.1038/s44306-024-00026-3 (2024).

211. G. Dieterle, J. Förster, H. Stoll, A. S. Semisalova, S. Finizio, A. Gangwar, M. Weigand, M. Noske, M. Fähnle, I. Bykova, J. Gräfe, D. A. Bozhko, H. Y. Musiienko-Shmarova, V. Tiberkevich, A. N. Slavin, C. H. Back, J. Raabe, G. Schütz & S. Wintz. Coherent Excitation of Heterosymmetric Spin Waves with Ultrashort Wavelengths. *Phys. Rev. Lett.* **122,** 117202. doi:10.1103/PhysRevLett.122.117202 (2019).

212. D. D. Sheka, V. P. Kravchuk & Y. Gaididei. Curvature effects in statics and dynamics of low dimensional magnets. *Journal of Physics A: Mathematical and Theoretical* **48,** 125202. doi:10.1088/1751-8113/48/12/125202 (2015).

213. Y. Gaididei, V. P. Kravchuk & D. D. Sheka. Curvature Effects in Thin Magnetic Shells. *Phys. Rev. Lett.* **112,** 257203. doi:10.1103/PhysRevLett.112.257203 (2014).

214. A. N. Kalish & A. K. Zvezdin. *Optical properties of toroidal media* (eds O. A. Aktsipetrov, V. M. Shalaev, S. V. Gaponenko & N. I. Zheludev) International Society for Optics and Photonics, 2007. doi:10.1117/12.752467.

215. N. A. Gusev, V. I. Belotelov & A. K. Zvezdin. Surface plasmons in nanowires with toroidal magnetic structure. *Opt. Lett.* **39,** 4108–4111. doi:10.1364/OL.39.004108 (2014).

216. D. J. Griffiths. *Introduction to Electrodynamics* 4th ed. (Cambridge University Press, 2017).

List of Publications and Presentations

Publications

The following publications were produced during the course of this doctoral research:

1. C. Ríos-Venegas, **F. Brevis**, R. A. Gallardo, and P. Landeros, "Dynamic origin of conical helix magnetization textures stabilized by Dzyaloshinskii–Moriya interaction," *Phys. Rev. B* **105**, 224403 (2022).

2. R. A. Gallardo, P. Alvarado-Seguel, **F. Brevis**, A. Roldán-Molina, K. Lenz, J. Lindner, and P. Landeros, "Spin-wave channeling in magnetization-graded nanostrips," *Nanomaterials* **12**, 2785 (2022).

3. J. Flores-Farías, R. A. Gallardo, **F. Brevis**, A. Roldán-Molina, D. Cortés-Ortuño, and P. Landeros, "Omnidirectional flat bands in chiral magnonic crystals," *Scientific Reports* **12**, 17831 (2022).

4. S. Tacchi, J. Flores-Farías, D. Petti, **F. Brevis**, A. Cattoni, G. Scaramuzzi, D. Girardi, D. Cortés-Ortuño, R. A. Gallardo, E. Albisetti, G. Carlotti, and P. Landeros, "Experimental observation of flat bands in one-dimensional chiral magnonic crystals," *Nano Letters* **23**, 6776–6783 (2023).

5. J. Flores-Farías, D. Cortés-Ortuño, **F. Brevis**, P. Landeros, and R. A. Gallardo, "Selective nonreciprocal localization of flat magnonic modes induced by a periodic Dzyaloshinskii–Moriya interaction," *Phys. Rev. B* **109**, 054423 (2024).

6. **F. Brevis**, P. Landeros, J. Lindner, A. Kákay, and L. Körber, "Curvature-induced parity loss and hybridization of magnons: Exploring the connection of flat and tubular magnetic shells," *Phys. Rev. B* **110**, 134428 (2024).

7. R. A. Gallardo, P. Alvarado-Seguel, **F. Brevis**, C. Gonzalez-Fuentes, J. W. González, K. Lenz, J. Lindner, and A. Roldán-Molina, "Nonreciprocal spin-wave channeling in ferromagnetic/heavy-metal nanostrips," *Results in Physics* **67**, 108057 (2024).

8. J. Flores-Farías, **F. Brevis**, R. Arias, P. Landeros, and R. A. Gallardo, "Flat modes in one-dimensional chiral magnonic superlattices," *Phys. Rev. B* **111**, 104438 (2025).

9. **F. Brevis**, L. Körber, B. Mimica-Figari, R. A. Gallardo, A. Kákay, and P. Landeros, "Toroidal moments in confined nanomagnets and their impact on magnonics," *Phys. Rev. Appl.* **24**, 024058 (2025).

10. J. Flores-Farías, P. Contreras-Gallardo, **F. Brevis**, J. W. González, N. Vidal-Silva, and R. A. Gallardo, "Emergence of flat bands and localized spin-wave modes in coupled bilayer magnonic crystals with different periodicities," *Chinese Journal of Physics* **98**, 384–398 (2025).

11. P. Contreras-Gallardo, J. Jiménez-Bustamante, N. Vidal-Silva, **F. Brevis**, J. W. González, O. Hellwig, J. Lindner, and R. A. Gallardo, "Spin-wave softening and the emergence of stripe domains in synthetic antiferromagnetic multilayers," *Phys. Rev. B* **112**, 224435 (2025).

12. M. Cepeda-Arancibia, **F. Brevis**, S. J. R. Holt, D. Cortés-Ortuño, H. Fangohr, and P. Landeros, "Micromagnetics of conical-helix textures in thin films with different kinds of Dzyaloshinskii–Moriya interactions," *npj Comput Mater* (2026).

Under review, submitted or in preparation

13. J. Flores-Farías, P. Contreras-Gallardo, **F. Brevis**, N. Vidal-Silva, P. Landeros, R. Arias, and R. A. Gallardo, "Mode localization in chiral Fibonacci magnonic quasicrystals," (under review).

14. B. Mimica-Figari, **F. Brevis**, D. Cortés-Ortuño, R. A. Gallardo, and P. Landeros, "Asymmetric reversal and quantized helical modes in ultrathin magnetic nanotubes with interfacial Dzyaloshinskii–Moriya interaction," (under review).

15. **F. Brevis**, F. Dietrich, P. Díaz, E. Cisternas, E. Vogel, J. W. González, R. A. Gallardo, and N. Vidal-Silva, "Magnon transport in vanadium-doped Ti_2C MXenes," (submitted).

16. J. Flores-Farías, P. Contreras-Gallardo, **F. Brevis**, M. Cepeda-Arancibia, D. Cortés-Ortuño, P. Landeros, and R. A. Gallardo, "Mode Localization in Chiral Magnonic Crystals via Graded Interfacial DMI," (submitted).

Conference Presentations

- "Momentos magnetoeléctricos en texturas magnéticas cónico helicoidales estabilizadas por la interacción de Dzyaloshinskii Moriya" (Poster) XXIII Simposio Chileno de Física (SOCHIFI 2022), Universidad Técnica Federico Santa María, Valparaíso.
- "Toroidal moment conical-helical magnetic textures stabilized by Dzyaloshinskii-Moriya interaction" (Poster) 14th Joint European Magnetic Symposia (JEMS 2023), Madrid, Spain.
- "Toroidal moment and nonreciprocity in magnonics" (Oral presentation) XXIV Simposio Chileno de Física (SOCHIFI 2024), Universidad de La Frontera, Temuco.
- "Toroidal moment and nonreciprocity in magnonics" (Oral presentation) Advances in Magnetics (AIM 2025), Bressanone, Italy.